2020

ELECTROSPUN FIBERS WITH SMART DELIVERY OF THERAPEUTIC AGENTS

Zahra Mahdieh

ELECTROSPUN FIBERS WITH SMART DELIVERY OF THERAPEUTIC AGENTS

By

Zahra Mahdieh

Master of Science in Materials Science and Engineering, Sharif University of Technology, Tehran, Iran, 2013
Bachelor of Science in Materials Science and Engineering, Isfahan University of Technology, Isfahan, Iran, 2010

Dissertation

Presented in partial fulfillment of the requirements for the degree of

Doctor of Philosophy

in Materials Science

The University of Montana
Missoula, MT

Official Graduation Date: May 2020

Scott Whittenburg,
Graduate School Dean

Andrij Holian

Armando McDonald

Nicholas R. Natale

Christopher Palmer

Aaron Thomas

Rob Walker

Mahdieh, Zahra, Ph.D., May 2020 Materials Science

Electrospun Fibers with Smart Delivery of Therapeutic Agents

Chairperson: Andrij Holian

Electrospinning is the most widely studied technique of producing fibers. Delivery of nanoparticles and therapeutic agents from electrospun fibers have potential uses in various fields including drug delivery, filtration, and cosmetics. However, controlling the delivery rate remains the main challenge. In the current study, core-shell structure fibers were developed with zinc oxide nanoparticles applied in the shell composition to improve the pore structure (release pathway) and mechanical stability. Fine-tuned delivery rates were achieved via loading different sizes of silver nanoparticles (Ag NP) inside the fiber core. *In vitro* drug release assays showed fast, slow, and intermediate delivery rates of 20 nm Ag NP, 110 nm Ag NP, and a mix of the two Ag NP, respectively. In the next step, temperature-controlled delivery rates were achieved via loading thermoresponsive microgel particles of poly(n-isopropylacrylamide) in addition to Ag NP inside the fiber core. *In vitro* drug release assays showed a fast release of Ag NP above the transition temperature and a slow release below the transition temperature. Ball-milling of the hydrogel was developed as a versatile, simple, and high yield technique of producing microgel particles (microgels). *In vitro* antibacterial tests confirmed the efficacy of the fiber meshes for anti-infection applications. Subcutaneous implantation of fiber meshes in a mouse model confirmed the *in vivo* drug release performance of the fibers. Fiber meshes were had appropriate biocompatibility and mechanical stability. The thorough characterization, *in vitro* and *in vivo* analyses of the fiber meshes confirmed their potential for prolonged drug delivery applications.

Table of Contents

Chapter 1: Introduction

Contribution

Zahra Mahdieh, University of Montana: Primary author.

Andrij Holian, University of Montana: Supervisor. Reviewed the final submission.

Gretchen McCaffrey, University of Montana: Provided editorial guidance.

Electrospinning: significance and technique

Electrospun fibers have attracted significant attention for their outstanding characteristics such as high surface area to volume ratio, adjustable surface morphology, and high interconnected mesh porosity (1). Electrospinning is recognized as the most popular technique for fabrication of nanofibers due to its simplicity, cost efficiency, versatility, and the possibility of large-scale production (1–4). Potential applications of electrospun fibers range from biomedical, filtration, agriculture and food industry, energy, sensors, and textiles. An overview of some of these applications is presented in Table 1.1.

Table 1.1 Potential applications of electrospun fibers.

Biomedical	Tissue scaffolds (5–8), wound dressings (9–13), cancer treatment (14–16), surgical Meshes (17,18), vascular grafts (19–21), heart patches (22–24), and drug delivery (25,26)
Filtration	Air and water filtration (27,28) and affinity membranes (29,30)
Agriculture and food industry	Biosensors (31), encapsulation (32), and food packaging (33,34)
Energy	Solar (35,36) and fuel cells (37–39), supercapacitor (40,41), and actuators (42,43)
Sensors	Gas, chemical, optical (44,45), and piezoelectric sensors (46,47)
Technical textile	Protective clothing (48,49), performance textile (46), and breathable textile (50)

Electrospun fibers are produced from a polymeric solution by application of high electric voltage between a spinneret and a collector. When an applied electric field overcomes the cohesive forces (mostly dominated by surface tension) of the polymeric solution at the capillary

tip, an electrically charged jet of polymer solution is drawn toward the collector. While the jet travels in the air, the solvent evaporates and the jet solidifies into fibers. Electrospinning provides non-woven fiber meshes with diameters from tens of microns down to tens of nanometers (51,52).

Electrospun fiber meshes in biomedical applications

Reviewing published studies on various applications of electrospun fibers reveals that electrospun fibers are well-known for biomedical applications, which can be due to their unique structure (53). In wound dressing applications, a flexible and porous structure of fiber meshes allows for liquid and gas permeability, and thus facilitates hemostasis, cell respiration, regulated moisture level, and a suitable bacterial barrier (12,13,54). In tissue engineering applications, the structure of electrospun fiber meshes similar to extracellular matrix (ECM) increases the cell interaction and nutrient diffusion, and thus facilitates tissue growth into the fiber mesh (55,56). Moreover, electrospun fiber meshes can be deposited as a thin layer on the surface of prostheses and implants to increase the surface area, improve the biocompatibility, and reduce friction, thus reducing the prosthetics failure rate by improving the implant-tissue interaction (57–59). Table 1.2 presents an overview for some biomedical applications of fiber meshes and their advantageous properties for each application.

Table 1.2 Biomedical applications of electrospun fibers and their advantageous properties for these applications. Therapeutic agents/drugs loaded into the electrospun fibers for development of drug delivery systems.

Application	**Advantages**	**Loaded drugs (purpose)**
Wound dressing	Regulate the moisture level Allows for oxygen diffusion Bacterial barrier Facilitates homeostasis	Growth factors (60–62) Antibiotics (63–65) Viruses (66–68) Vitamins (69–71) Hemostatic agents (72–74) Analgesics (75–77)
Cancer treatment	Isolating the tumor Localization of drug delivery	Anticancer drugs (78–80)
Prosthetic coating	Providing an interactive surface Reducing the infection risk	Antibacterial agents (81–83) Bone regenerative (59,84,85)
Tissue engineering (vascular grafts, bone scaffolds, skin grafts, heart patches, surgical meshes, etc)	Resembling ECM structure Allowing for diffusion of nutrients and wastes	Growth factors and stem cells (86–89) Proteins (90–93) Antibiotics (94) Polypeptides (95,96) Anticoagulant (97–99)
Bone scaffolds	Providing suitable surface for bone regeneration	Bone regenerative nano/microparticles (β-tricalcium phosphate (100,101), hydroxyapatite (102–104), bioactive glass (94,105,106))

A distinguishing advantage of electrospun fiber meshes is the possibility of loading therapeutic agents for development of drug delivery systems (107). Drug delivery can be accompanied with any biomedical application of fiber mesh use in order to improve the outcome (107). Furthermore, loading drugs into fiber meshes can provide local drug deliveries for administration of high and sustained drug concentrations without the need for large systemic doses, thus reducing the off-target tissue toxicities (108). Consequently, a great number of studies have been performed in attempts to develop fiber meshes with drug delivery properties. Therapeutic agents ranging from antibiotics, growth factors, viruses, vitamins, analgesics, etc. have been incorporated into electrospun fibers. An overview of these drug delivery systems is presented in Table 1.2.

Development of drug delivery systems made of fiber meshes: methods and challenges

Therapeutic agents/drugs can be loaded into electrospun fibers before or after the electrospinning (pre- or post-electrospinning) (109). The major methods of pre-electrospinning drug loading are illustrated in Figure 1.1.

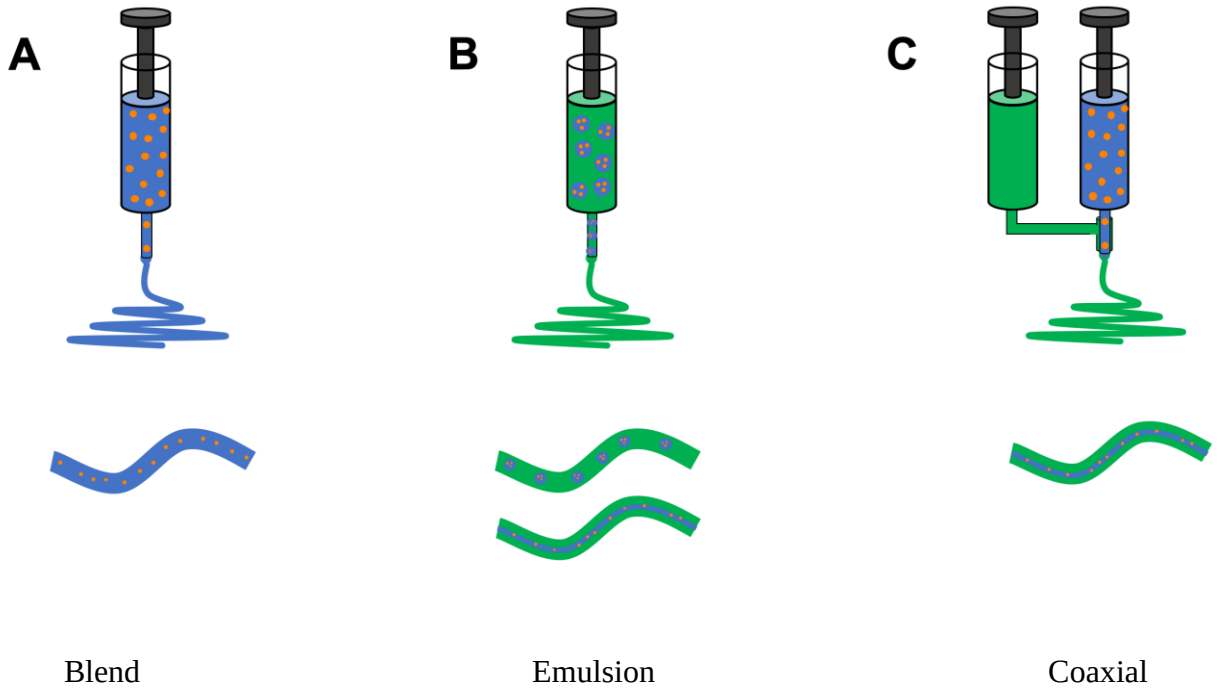

Figure 1.1 Schematic illustration of the electrospinning syringe set up and a fiber product for three major methods of pre-electrospinning drug loading: (A) blend electrospinning, (B) emulsion electrospinning, and (C) coaxial electrospinning.

The basic method used for loading drugs into electrospun fiber meshes is blend electrospinning in which a solution of polymer and drug is used during the electrospinning process (Figure 1.1A). The main advantage of this method is a simple electrospinning set up and less complications for adjusting the electrospinning parameters. A proper distribution of drugs in the solution and later in the electrospun fibers is a crucial factor to have a sustained delivery. However, most drug molecules migrate to the fiber surface with the evaporation of solvents during the electrospinning process. Accumulation of drug molecules at the surface of fibers causes sudden release of drugs, defined as the burst release effect. Since electrospun fibers have the potential for burst release due to their high surface area to volume ratio, surface accumulation of drugs exacerbates the burst release (110). Another challenge in this method is that being

blended in the electrospinning solution, drugs can be harmed by the organic solvents and harsh conditions of electrospinning (such as high voltage and rapid changes in the vapor pressure). Therefore, an important limitation of this method is difficulty for loading fragile drugs or bioactive agents into the fibers.

A more advanced method for incorporation of drugs is emulsion electrospinning in which two liquids, stabilized by an emulsifier, are used for the electrospinning process (Figure 1.1B). In this method fragile drugs are protected from solvents used in the polymer solution. Emulsion properties and electrospinning parameters can be manipulated in this method to form fibers with a core-shell structure. The advantage of the core-shell structure is that the fiber shell provides a barrier to reduce the burst release. In practice, adjusting the electrospinning parameters is challenging in this method. In many studies, fibers with a dispersed phase of droplets are reported instead of the core-shell structure (Figure 1.1B) (111). Moreover, selecting a stable polymer-drug emulsion system brings limitations to this method. An unstable emulsion results in agglomeration and localization of drugs on the surface of fibers, which results in the burst release problem (112).

The core-shell structure can also be produced via coaxial electrospinning in which two immiscible solutions (core and shell) are electrospun simultaneously through a coaxial spinneret (Figure 1.1C). The main advantage of this method is protecting bioactive or fragile therapeutic agents from organic solvents and harsh electrospinning conditions. In this method, drug molecules can be loaded inside the core or (less-fragile drugs) can be blended with the shell solution. Drugs loaded in the shell release via desorption/leaching into the surrounding liquid media i.e. erosion/degradation of the shell (111,113). To release drugs loaded in the core, pores are formed in the shell using porogens. A porogen is a polymer added into the shell solution

before electrospinning. The porogen is selectively dissolved or melted away from the fibers after electrospinning resulting in pores formed in the shell structure. Although application of porogen in the shell seems suitable for drug release, in practice, high percentages of porogens are needed to form pores that are connected to the core ("interconnected pores" or "open pores"). Application of high percentages of porogens cause rupture/swelling and failure of the shell structure when dissolved, resulting in an uncontrolled and burst release of the drug (114,115). Therefore, controlling the pore structure while maintaining the fiber integrity is a crucial challenge of drug delivery in core-shell structured fibers.

Electrospun fiber meshes and the potential for smart drug delivery

Smart drug delivery systems are drug carriers that can be stimulated with the changes of temperature, pH, light, electromagnetic fields, and mechanical forces to release drugs (116). Compared to conventional drug delivery systems, stimuli-responsive delivery further improves the drug targeting efficacy, thus minimizing the off-target tissue toxicities (117). For instance, a thermoresponsive drug delivery system can release an antibacterial drug upon the temperature increase of the infected tissue. Localized and responsive delivery of such a system improves treatment efficacy, reduces cost and discomfort, and prevents the overuse of antibacterial drugs which can cause antibacterial resistance (118). Consequently, fabrication of stimuli responsive electrospun fibers has attracted attention due to their importance in drug delivery applications. Figure 1.2 reviews the main electrospun fiber structures developed from poly(n-isopropylacrylamide) (PNIPAM), which is a thermoresponsive polymer. PNIPAM is the most studied thermoresponsive polymer for drug delivery applications because it has a transition temperature close to human body temperature.

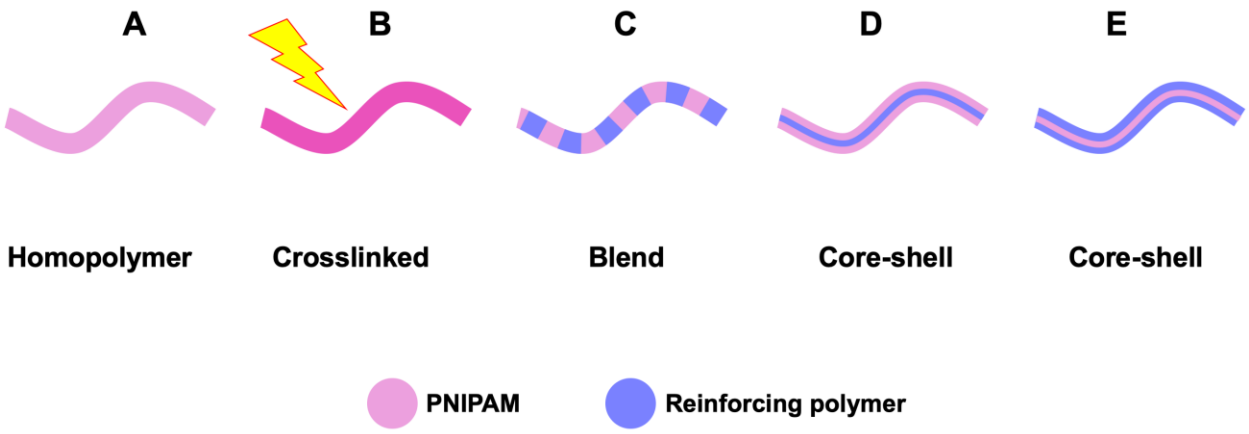

Figure 1.2 Schematic illustration of fiber structures developed from electrospinning of PNIPAM.

The basic method used to produce thermoresponsive fiber meshes is electrospinning monolithic fibers in which a solution of PNIPAM is used for electrospinning (Figure 1.2) (119). This method requires a simple electrospinning set up with fewer complications while adjusting the electrospinning parameters. However, fibers made in this method lack suitable mechanical properties and stability in aqueous solutions (120). Suitable mechanical properties of electrospun fibers is an important factor to prevent the burst release and obtaining a long term and controlled drug release (121,122). Furthermore, mechanical properties are especially important for thermoresponsive (or stimuli-responsive) fibers because release of these polymers into the tissue can cause toxicity (123).

Post-electrospinning crosslinking of the PNIPAM fibers is another method, which was mainly developed to improve the mechanical properties (Figure 1.2B). Post-crosslinking is performed by heating fibers or exposing fibers to ultraviolet light (124,125). This method results in better mechanical properties and a controlled drug release. However, it is not possible to load fragile bioactive agents in this method, because they are susceptible to denaturation under the harsh crosslinking conditions and organic solvents (126).

Electrospinning a PNIPAM blended or copolymerized with another polymer also improves the mechanical properties of the fibers (Figure 1.2C) (124). In this method, a drug could be also blended into the electrospinning solution (Figure 1.1A). Therefore, a simple electrospinning procedure is an advantage of this method. However, drug release rate is poorly controlled (127). Harsh electrospinning conditions and solvents in this method prevent loading fragile or bioactive agents. A more advanced group of fibers are core-shell structured with PNIPAM in the shell and a strong polymer, such as polycaprolactone, in the core (Figure 1.2D) (128,129). These fibers have better mechanical properties due to the strong core. However, PNIPAM in the shell has a high degree of hydrophilicity and can dissolve/detach from the fibers in an aqueous media (which is the common drug delivery media). Instability of PNIPAM results in burst release of drugs and also induces toxicity.

In one study (130), core-shell fibers with PNIPAM in the core and polyurethane in the shell were developed. The core-shell fibers were compared to fibers produced from a blend of PNIPAM and polyurethane (method 2C). It was shown that the burst release, seen in the blend fibers, were reduced in the core-shell fibers. However, no drug release pathway was formed in core-shell fibers. Therefore, the drug release profile reached a plateau after 10 h of immersion with 58% of drug trapped inside the fibers.

Purpose of the study

To our knowledge, electrospun fibers developed prior to this study could not address all the discussed problems simultaneously. For example, improving the mechanical properties via post-crosslinking prevented the possibility of loading bioactive agents. Therefore, the purpose of this study was to develop electrospun fibers with prolonged and controlled drug release, suitable

mechanical properties, and minimum toxicity, whilst having the possibility of loading fragile drugs or bioactive agents. These goals were addressed in three sections as follows.

First (Chapter 2), the core-shell fiber structure was chosen for the drug delivery method because it is possible to load fragile drugs or bioactive agents inside the core. Zinc oxide nanoparticles (ZnO NP) were applied in the shell composition to form open pores while improving the mechanical properties because these are necessary factors to avoid burst release and control the release rate. Silver nanoparticles (Ag NP) were loaded in the fiber core as a model antibacterial drug, but could be replaced by other therapeutic agents or nanoparticles for different applications. Different sizes of Ag NP were applied to fine-tune the release rate via controlling the diffusion rate of nanoparticles through the pores.

Second (Chapter 3), PNIPAM microgel particles were loaded in the core in addition to Ag NP to obtain a temperature-responsive release of Ag NP. Loading PNIPAM microgel particles protected the microgel from harsh conditions of electrospinning which can induce the hydrophilic to hydrophobic transition and thus unwanted release of drugs. Moreover, loading PNIPAM microgel particles in the core prevented their contact with solvents used in the shell solution, thus preventing any unwanted phase transition or reaction of microgel. Another advantage was preventing direct contact of the PNIPAM microgel particles with the tissue and thus reducing any possible toxicity. The PNIPAM microgel particles were produced via a novel use of ball milling. This method is simple, versatile, and nontoxic hence allows for particle production from various kinds of stimuli-responsive microgels.

Third (Chapter 4), *in vitro* and *in vivo* assessments of the developed fiber meshes were performed to evaluate their efficacy. Antibacterial and cytotoxicity measurements of the fiber meshes were performed *in vitro*. Since the body fluid dynamic differs from the *in vitro* drug

release studies, performing animal model studies were essential to confirm the efficacy of fiber meshes. Histological studies of the fiber meshes were performed to evaluate tissue responses to the fiber meshes.

References

1. Zamani M, Prabhakaran MP, Ramakrishna S. Advances in drug delivery via electrospun and electrosprayed nanomaterials. Vol. 8, International Journal of Nanomedicine. 2013. p. 2997–3017.

2. Abrigo M, McArthur SL, Kingshott P. Electrospun nanofibers as dressings for chronic wound care: Advances, challenges, and future prospects. Vol. 14, Macromolecular Bioscience. Wiley-VCH Verlag; 2014. p. 772–92.

3. Huang ZM, Zhang YZ, Kotaki M, Ramakrishna S. A review on polymer nanofibers by electrospinning and their applications in nanocomposites. Compos Sci Technol. 2003 Nov 1;63(15):2223–53.

4. Lu P, Ding B. Applications of Electrospun Fibers. Recent Pat Nanotechnol. 2008 Nov 9;2(3):169–82.

5. Pham QP, Sharma U, Mikos AG. Electrospinning of polymeric nanofibers for tissue engineering applications: A review. Vol. 12, Tissue Engineering. Mary Ann Liebert, Inc. 2 Madison Avenue Larchmont, NY 10538 USA ; 2006. p. 1197–211.

6. Murugan R, Ramakrishna S. Nano-featured scaffolds for tissue engineering: A review of spinning methodologies. Vol. 12, Tissue Engineering. Mary Ann Liebert Inc.; 2006. p. 435–47.

7. Khorshidi S, Solouk A, Mirzadeh H, Mazinani S, Lagaron JM, Sharifi S, et al. A review of key challenges of electrospun scaffolds for tissue-engineering applications. Vol. 10, Journal of Tissue Engineering and Regenerative Medicine. John Wiley and Sons Ltd; 2016. p. 715–38.

8. Nisbet DR, Forsythe JS, Shen W, Finkelstein DI, Horne MK. Review paper: a review of the cellular response on electrospun nanofibers for tissue engineering. J Biomater Appl. 2009 Jul 12;24(1):7–29.

9. Zahedi P, Rezaeian I, Ranaei-Siadat SO, Jafari SH, Supaphol P. A review on wound dressings with an emphasis on electrospun nanofibrous polymeric bandages. Vol. 21, Polymers for Advanced Technologies. John Wiley & Sons, Ltd; 2010. p. 77–95.

10. Khil MS, Cha D Il, Kim HY, Kim IS, Bhattarai N. Electrospun Nanofibrous Polyurethane Membrane as Wound Dressing. J Biomed Mater Res - Part B Appl Biomater. 2003 Nov 15;67(2):675–9.

11. Toncheva A, Spasova M, Paneva D, Manolova N, Rashkov I. Polylactide (PLA)-Based Electrospun Fibrous Materials Containing Ionic Drugs as Wound Dressing Materials: A Review. Int J Polym Mater Polym Biomater. 2014 Sep 2;63(13):657–71.

12. Rieger KA, Birch NP, Schiffman JD. Designing electrospun nanofiber mats to promote wound healing-a review. Vol. 1, Journal of Materials Chemistry B. The Royal Society of Chemistry; 2013. p. 4531–41.

13. Liu M, Duan XP, Li YM, Yang DP, Long YZ. Electrospun nanofibers for wound healing. Vol. 76, Materials Science and Engineering C. Elsevier Ltd; 2017. p. 1413–23.

14. Ignatova M, Rashkov I, Manolova N. Drug-loaded electrospun materials in wound-dressing applications and in local cancer treatment. Vol. 10, Expert Opinion on Drug Delivery. Taylor & Francis; 2013. p. 469–83.

15. Ma G, Liu Y, Peng C, Fang D, He B, Nie J. Paclitaxel loaded electrospun porous nanofibers as mat potential application for chemotherapy against prostate cancer. Carbohydr Polym. 2011 Aug 15;86(2):505–12.

16. Sridhar R, Ravanan S, Venugopal JR, Sundarrajan S, Pliszka D, Sivasubramanian S, et al. Curcumin-and natural extract-loaded nanofibres for potential treatment of lung and breast cancer: In vitro efficacy evaluation. J Biomater Sci Polym Ed. 2014 Jul 3;25(10):985–98.

17. Veleirinho B, Coelho DS, Dias PF, Maraschin M, Bia Pinto R, Cargnin-Ferreira E, et al. Foreign Body Reaction Associated with PET and PET/ Chitosan Electrospun Nanofibrous Abdominal Meshes.

18. Monticelli O, Bocchini S, Gardella L, Cavallo D, Cebe P, Germelli G. Impact of synthetic talc on PLLA electrospun fibers. Eur Polym J. 2013 Sep 1;49(9):2572–83.

19. Rocco KA, Maxfield MW, Best CA, Dean EW, Breuer CK. In vivo applications of electrospun tissue-engineered vascular grafts: A review. Vol. 20, Tissue Engineering - Part B: Reviews. Mary Ann Liebert Inc.; 2014. p. 628–40.

20. Lee SJ, Yoo JJ, Lim GJ, Atala A, Stitzel J. In vitro evaluation of electrospun nanofiber scaffolds for vascular graft application. J Biomed Mater Res - Part A. 2007 Dec 15;83(4):999–1008.

21. Centola M, Rainer A, Spadaccio C, Porcellinis S De, Genovese JA, Trombetta M. Combining electrospinning and fused deposition modeling for the fabrication of a hybrid vascular graft. Biofabrication. 2010 Mar 10;2(1):014102.

22. Kitsara M, Agbulut O, Kontziampasis D, Chen Y, Menasché P. Fibers for hearts: A critical review on electrospinning for cardiac tissue engineering. Vol. 48, Acta Biomaterialia. Elsevier Ltd; 2017. p. 20–40.

23. Prabhakaran MP, Kai D, Ghasemi-Mobarakeh L, Ramakrishna S. Electrospun biocomposite nanofibrous patch for cardiac tissue engineering. Biomed Mater. 2011 Aug 3;6(5):055001.

24. Ehler E, Jayasinghe SN. Cell electrospinning cardiac patches for tissue engineering the heart. Analyst. 2014 Aug 11;139(18):4449–52.

25. Haider A, Haider S, Kang IK. A comprehensive review summarizing the effect of electrospinning parameters and potential applications of nanofibers in biomedical and biotechnology. Vol. 11, Arabian Journal of Chemistry. Elsevier B.V.; 2018. p. 1165–88.

26. Khalf A, Madihally S V. Recent advances in multiaxial electrospinning for drug delivery. Vol. 112, European Journal of Pharmaceutics and Biopharmaceutics. Elsevier B.V.; 2017. p. 1–17.

27. Hajra MG, Mehta K, Chase GG. Effects of humidity, temperature, and nanofibers on drop coalescence in glass fiber media. Sep Purif Technol. 2003 Jan;30(1):79–88.

28. Gopal R, Kaur S, Ma Z, Chan C, Ramakrishna S, Matsuura T. Electrospun nanofibrous filtration membrane. J Memb Sci. 2006 Sep 15;281(1–2):581–6.

29. Wang X, Hsiao BS. Electrospun nanofiber membranes. Vol. 12, Current Opinion in Chemical Engineering. Elsevier Ltd; 2016. p. 62–81.

30. Ahmed FE, Lalia BS, Hashaikeh R. A review on electrospinning for membrane fabrication: Challenges and applications. Vol. 356, Desalination. Elsevier; 2015. p. 15–30.

31. Mercante LA, Scagion VP, Migliorini FL, Mattoso LHC, Correa DS. Electrospinning-based (bio)sensors for food and agricultural applications: A review. Vol. 91, TrAC - Trends in Analytical Chemistry. Elsevier B.V.; 2017. p. 91–103.

32. Noruzi M. Electrospun nanofibres in agriculture and the food industry: a review. Vol. 96, Journal of the science of food and agriculture. John Wiley & Sons, Ltd; 2016. p. 4663–78.

33. Qian Y-F, Zheng L-J, Song R-Y, Du B. Electrospinning of pullulan nanofibers for food package materials. 2013;

34. Drosou CG, Krokida MK, Biliaderis CG. Encapsulation of bioactive compounds through electrospinning/electrospraying and spray drying: A comparative assessment of food-related applications. Vol. 35, Drying Technology. Taylor and Francis Inc.; 2017. p. 139–62.

35. Yang L, Leung WWF. Electrospun TiO2 nanorods with carbon nanotubes for efficient electron collection in dye-sensitized solar cells. Adv Mater. 2013 Mar 25;25(12):1792–5.

36. Panda PK. Ceramic Nanofibers by Electrospinning Technique-A Review. Trans Indian Ceram Soc. 2007;66(2):65–76.

37. Junoh H, Jaafar J, Anam MN, Norddin M, Ismail AF, Hafiz M, et al. A Review on the Fabrication of Electrospun Polymer Electrolyte Membrane for Direct Methanol Fuel Cell. 2015;

38. Sood R, Cavaliere S, Jones DJ, Rozière J. Electrospun nanofibre composite polymer electrolyte fuel cell and electrolysis membranes. Vol. 26, Nano Energy. Elsevier Ltd; 2016. p. 729–45.

39. Cavaliere S, Subianto S, Savych I, Jones DJ, Rozière J. Electrospinning: Designed architectures for energy conversion and storage devices. Vol. 4, Energy and Environmental Science. The Royal Society of Chemistry; 2011. p. 4761–85.

40. Li X, Chen Y, Huang H, Mai YW, Zhou L. Electrospun carbon-based nanostructured electrodes for advanced energy storage - A review. Vol. 5, Energy Storage Materials. Elsevier B.V.; 2016. p. 58–92.

41. Mao X, Hatton TA, Rutledge GC. A Review of Electrospun Carbon Fibers as Electrode Materials for Energy Storage.

42. Persano L, Camposeo A, Pisignano D. Active polymer nanofibers for photonics, electronics, energy generation and micromechanics. Vol. 43, Progress in Polymer Science. Elsevier Ltd; 2015. p. 48–95.

43. Fang J, Niu H, Wang H, Wang X, Lin T. Enhanced mechanical energy harvesting using needleless electrospun poly(vinylidene fluoride) nanofibre webs. Energy Environ Sci. 2013 Jul 21;6(7):2196–202.

44. Lee SH, Ku BC, Wang X, Samuelson LA, Kumar J. Design, synthesis and electrospinning of a novel fluorescent polymer for optical sensor applications. Mater Res Soc Symp - Proc. 2002;708:403–8.

45. Wang X, Drew C, Lee SH, Senecal KJ, Kumar J, Samuelson LA. Electrospun Nanofibrous Membranes for Highly Sensitive Optical Sensors. Nano Lett. 2002 Nov;2(11):1273–5.

46. Baniasadi M, Huang J, Xu Z, Moreno S, Yang X, Chang J, et al. High-performance coils and yarns of polymeric piezoelectric nanofibers. ACS Appl Mater Interfaces. 2015 Mar 11;7(9):5358–66.

47. Maity K, Mandal D. All-Organic High-Performance Piezoelectric Nanogenerator with Multilayer Assembled Electrospun Nanofiber Mats for Self-Powered Multifunctional Sensors. ACS Appl Mater Interfaces. 2018 May 30;10(21):18257–69.

48. Schreuder-Gibson H, Gibson P, Senecal K, Sennett M, Walker J, Yeomans W, et al. Protective textile materials based on electrospun nanofibers. J Adv Mater. 2002 Jul;34(3):44–55.

49. Gibson PW, Schreuder-Gibson HL, Rivin D. Electrospun fiber mats: Transport properties. AIChE J. 1999;45(1):190–5.

50. Kang YK, Park CH, Kim J, Kang TJ. Application of electrospun polyurethane web to breathable water-proof fabrics. Fibers Polym. 2007 Dec 1;8(5):564–70.

51. Kowalewski TA, Bło´nski S, Bło´nski B, Barral S. Experiments and modelling of electrospinning process.

52. Lannutti J, Reneker D, Ma T, Tomasko D, Farson D. Electrospinning for tissue engineering scaffolds. Mater Sci Eng C. 2007 Apr 1;27(3):504–9.

53. Sridhar R, Lakshminarayanan R, Madhaiyan K, Barathi VA, Limh KHC, Ramakrishna S. Electrosprayed nanoparticles and electrospun nanofibers based on natural materials: Applications

in tissue regeneration, drug delivery and pharmaceuticals. Vol. 44, Chemical Society Reviews. Royal Society of Chemistry; 2015. p. 790–814.

54. Hassiba AJ, El Zowalaty ME, Nasrallah GK, Webster TJ, Luyt AS, Abdullah AM, et al. Review of recent research on biomedical applications of electrospun polymer nanofibers for improved wound healing. Vol. 11, Nanomedicine. Future Medicine Ltd.; 2016. p. 715–37.

55. Sill TJ, von Recum HA. Electrospinning: Applications in drug delivery and tissue engineering. Vol. 29, Biomaterials. Elsevier; 2008. p. 1989–2006.

56. Lannutti J, Reneker D, Ma T, Tomasko D, Farson D. Electrospinning for tissue engineering scaffolds. Mater Sci Eng C. 2007;27(3):504–9.

57. Han N, Johnson JK, Bradley PA, Parikh KS, Lannutti JJ, Winter JO. Cell Attachment to Hydrogel-Electrospun Fiber Mat Composite Materials. J Funct Biomater. 2012 Jul 27;3(3):497–513.

58. Bishop A, Balázsi C, Yang JHC, Gouma PI. Biopolymer-hydroxyapatite composite coatings prepared by electrospinning. In: Polymers for Advanced Technologies. John Wiley & Sons, Ltd; 2006. p. 902–6.

59. Laurencin CT, Kumbar SG, Nukavarapu SP, James R, Hogan M V. Recent Patents on Electrospun Biomedical Nanostructures: An Overview.

60. Yang Y, Xia T, Zhi W, Wei L, Weng J, Zhang C, et al. Promotion of skin regeneration in diabetic rats by electrospun core-sheath fibers loaded with basic fibroblast growth factor. Biomaterials. 2011 Jun 1;32(18):4243–54.

61. Lai HJ, Kuan CH, Wu HC, Tsai JC, Chen TM, Hsieh DJ, et al. Tailored design of electrospun composite nanofibers with staged release of multiple angiogenic growth factors for chronic wound healing. Acta Biomater. 2014 Oct 1;10(10):4156–66.

62. Choi JS, Leong KW, Yoo HS. In vivo wound healing of diabetic ulcers using electrospun nanofibers immobilized with human epidermal growth factor (EGF). Biomaterials. 2008 Feb;29(5):587–96.

63. GhavamiNejad A, Rajan Unnithan A, Ramachandra Kurup Sasikala A, Samarikhalaj M, Thomas RG, Jeong YY, et al. Mussel-Inspired Electrospun Nanofibers Functionalized with Size-Controlled Silver Nanoparticles for Wound Dressing Application. ACS Appl Mater Interfaces. 2015 Jun 10;7(22):12176–83.

64. Rodríguez-Tobías H, Morales G, Ledezma A, Romero J, Saldívar R, Langlois V, et al. Electrospinning and electrospraying techniques for designing novel antibacterial poly(3-hydroxybutyrate)/zinc oxide nanofibrous composites. J Mater Sci. 2016 Sep 1;51(18):8593–609.

65. Unnithan AR, Barakat NAM, Tirupathi Pichiah PB, Gnanasekaran G, Nirmala R, Cha YS, et al. Wound-dressing materials with antibacterial activity from electrospun polyurethane-dextran nanofiber mats containing ciprofloxacin HCl. Carbohydr Polym. 2012 Nov 6;90(4):1786–93.

66. Lee S, Kim JS, Chu HS, Kim GW, Won JI, Jang JH. Electrospun nanofibrous scaffolds for controlled release of adeno-associated viral vectors. Acta Biomater. 2011 Nov 1;7(11):3868–76.

67. Lee S, Jin G, Jang J-H. Electrospun nanofibers as versatile interfaces for efficient gene delivery. 2014.

68. Andriolo JM, Wyss GF, Murphy JP, Pedulla ML, Katie Hailer M, Skinner JL. Iron-Doped Apatite Nanoparticles Delivered via Electrospun Fiber Mesh for Maximized Bacterial Killing by Bacteriophage. In: MRS Advances. Materials Research Society; 2017. p. 2465–70.

69. Li H, Wang M, Williams GR, Wu J, Sun X, Lv Y, et al. Electrospun gelatin nanofibers loaded with vitamins A and e as antibacterial wound dressing materials. RSC Adv. 2016 May 18;6(55):50267–77.

70. Kheradvar SA, Nourmohammadi J, Tabesh H, Bagheri B. Starch nanoparticle as a vitamin E-TPGS carrier loaded in silk fibroin-poly(vinyl alcohol)-Aloe vera nanofibrous dressing. Colloids Surfaces B Biointerfaces. 2018 Jun 1;166:9–16.

71. Zarandi MA, Zahedi P, Rezaeian I, Salehpour A, Gholami M, Motealleh B. Drug release, cell adhesion and wound healing evaluations of electrospun carboxymethyl chitosan/polyethylene oxide nanofibres containing phenytoin sodium and Vitamin C. IET Nanobiotechnology. 2015 Aug 1;9(4):191–200.

72. Wang H, Li M, Hu J, Wang C, Xu S, Han CC. Multiple targeted drugs carrying biodegradable membrane barrier: Anti-adhesion, hemostasis, and anti-infection. Biomacromolecules. 2013 Apr 8;14(4):954–61.

73. Xia Q, Liu Z, Wang C, Zhang Z, Xu S, Han CC. A biodegradable trilayered barrier membrane composed of sponge and electrospun layers: Hemostasis and antiadhesion. Biomacromolecules. 2015 Sep 14;16(9):3083–92.

74. Spasova M, Manolova N, Paneva D, Mincheva R, Dubois P, Rashkov I, et al. Polylactide stereocomplex-based electrospun materials possessing surface with antibacterial and hemostatic properties. Biomacromolecules. 2010 Jan 11;11(1):151–9.

75. Li X, Wang C, Yang S, Liu P, Zhang B. Electrospun PCL/mupirocin and chitosan/ lidocaine hydrochloride multifunctional double layer nanofibrous scaffolds for wound dressing applications. Int J Nanomedicine. 2018;13:5287–99.

76. Thakur RA, Florek CA, Kohn J, Michniak BB. Electrospun nanofibrous polymeric scaffold with targeted drug release profiles for potential application as wound dressing. Int J Pharm. 2008 Nov 19;364(1):87–93.

77. Tseng YY, Liu SJ. Nanofibers used for the delivery of analgesics. Vol. 10, Nanomedicine. Future Medicine Ltd.; 2015. p. 1785–800.

78. Balaji A, Vellayappan M V., John AA, Subramanian AP, Jaganathan SK, Supriyanto E, et al. An insight on electrospun-nanofibers-inspired modern drug delivery system in the treatment of deadly cancers. RSC Adv. 2015 Jun 30;5(71):57984–8004.

79. Ignatova MG, Manolova NE, Toshkova RA, Rashkov IB, Gardeva EG, Yossifova LS, et al. Electrospun nanofibrous mats containing quaternized chitosan and polylactide with in vitro antitumor activity against hela cells. Biomacromolecules. 2010 Jul 14;11(6):1633–45.

80. Chen P, Wu QS, Ding YP, Chu M, Huang ZM, Hu W. A controlled release system of titanocene dichloride by electrospun fiber and its antitumor activity in vitro. Eur J Pharm Biopharm. 2010 Nov 1;76(3):413–20.

81. Li LL, Wang LM, Xu Y, Lv LX. Preparation of gentamicin-loaded electrospun coating on titanium implants and a study of their properties in vitro. Arch Orthop Trauma Surg. 2012 Jun 29;132(6):897–903.

82. Zhang L, Yan J, Yin Z, Tang C, Guo Y, Li D, et al. Electrospun vancomycin-loaded coating on titanium implants for the prevention of implant-associated infections. Int J Nanomedicine. 2014 Jun 23;9(1):3027–36.

83. Shahi RG, Albuquerque MTP, Münchow EA, Blanchard SB, Gregory RL, Bottino MC. Novel bioactive tetracycline-containing electrospun polymer fibers as a potential antibacterial dental implant coating. Odontology. 2017 Jul 1;105(3):354–63.

84. Bishop A, Balázsi C, Yang JHC, Gouma P-I. Biopolymer-hydroxyapatite composite coatings prepared by electrospinning. Polym Adv Technol. 2006 Nov 1;17(11–12):902–6.

85. Soujanya GK, Hanas T, Chakrapani VY, Sunil BR, Kumar TSS. Electrospun Nanofibrous Polymer Coated Magnesium Alloy for Biodegradable Implant Applications. Procedia Mater Sci. 2014 Jan 1;5:817–23.

86. Sahoo S, Toh SL, Goh JCH. A bFGF-releasing silk/PLGA-based biohybrid scaffold for ligament/tendon tissue engineering using mesenchymal progenitor cells. Biomaterials. 2010 Apr 1;31(11):2990–8.

87. Sahoo S, Ang LT, Cho-Hong Goh J, Toh SL. Bioactive nanofibers for fibroblastic differentiation of mesenchymal precursor cells for ligament/tendon tissue engineering applications. Differentiation. 2010 Feb 1;79(2):102–10.

88. Sahoo S, Ang LT, Goh JCH, Toh SL. Growth factor delivery through electrospun nanofibers in scaffolds for tissue engineering applications. J Biomed Mater Res - Part A. 2010 Jun 15;93(4):1539–50.

89. Yin Z, Chen X, Chen JL, Shen WL, Hieu Nguyen TM, Gao L, et al. The regulation of tendon stem cell differentiation by the alignment of nanofibers. Biomaterials. 2010 Mar 1;31(8):2163–75.

90. He W, Ma Z, Wee ET, Yi XD, Robless PA, Thiam CL, et al. Tubular nanofiber scaffolds for tissue engineered small-diameter vascular grafts. J Biomed Mater Res - Part A. 2009 Jul 1;90(1):205–16.

91. He W, Ma ZW, Yong T, Teo WE, Ramakrishna S. Fabrication of collagen-coated biodegradable polymer nanofiber mesh and its potential for endothelial cells growth. Biomaterials. 2005 Dec 1;26(36):7606–15.

92. Ma Z, Kotaki M, Yong T, He W, Ramakrishna S. Surface engineering of electrospun polyethylene terephthalate (PET) nanofibers towards development of a new material for blood vessel engineering. Biomaterials. 2005 May 1;26(15):2527–36.

93. Zhu Y, Leong MF, Ong WF, Chan-Park MB, Chian KS. Esophageal epithelium regeneration on fibronectin grafted poly(l-lactide-co-caprolactone) (PLLC) nanofiber scaffold. Biomaterials. 2007 Feb 1;28(5):861–8.

94. Hong Y, Chen X, Jing X, Fan H, Guo B, Gu Z, et al. Preparation, bioactivity, and drug release of hierarchical nanoporous bioactive glass ultrathin fibers. Adv Mater. 2010 Feb 9;22(6):754–8.

95. Wise SG, Byrom MJ, Waterhouse A, Bannon PG, Ng MKC, Weiss AS. A multilayered synthetic human elastin/polycaprolactone hybrid vascular graft with tailored mechanical properties. Acta Biomater. 2011 Jan 1;7(1):295–303.

96. Blit PH, Battiston KG, Yang M, Paul Santerre J, Woodhouse KA. Electrospun elastin-like polypeptide enriched polyurethanes and their interactions with vascular smooth muscle cells. Acta Biomater. 2012 Jul 1;8(7):2493–503.

97. Wang S, Zhang Y, Wang H, Dong Z. Preparation, characterization and biocompatibility of electrospinning heparin-modified silk fibroin nanofibers. Int J Biol Macromol. 2011 Mar 1;48(2):345–53.

98. Du F, Wang H, Zhao W, Li D, Kong D, Yang J, et al. Gradient nanofibrous chitosan/poly e{open}-caprolactone scaffolds as extracellular microenvironments for vascular tissue engineering. Biomaterials. 2012 Jan 1;33(3):762–70.

99. Liu B, Xu F, Guo MY, Chen SF, Wang J, Zhang B. Electrospun PLLA fibers coated with chitosan/heparin for scaffold of vascular tissue engineering. Surf Coatings Technol. 2013 Aug 15;228(SUPPL.1):S568–73.

100. Bianco A, di Federico E, Cacciotti I. Electrospun poly(ε-caprolactone)-based composites using synthesized β-tricalcium phosphate. Polym Adv Technol. 2011 Dec 1;22(12):1832–41.

101. Yeo M, Lee H, Kim G. Three-dimensional hierarchical composite scaffolds consisting of polycaprolactone, β-tricalcium phosphate, and collagen nanofibers: Fabrication, physical properties, and in vitro cell activity for bone tissue regeneration. Biomacromolecules. 2011 Feb 14;12(2):502–10.

102. Peng F, Yu X, Wei M. In vitro cell performance on hydroxyapatite particles/poly(L-lactic acid) nanofibrous scaffolds with an excellent particle along nanofiber orientation. Acta Biomater. 2011 Jun 1;7(6):2585–92.

103. Lee JH, Rim NG, Jung HS, Shin H. Control of osteogenic differentiation and mineralization of human mesenchymal stem cells on composite nanofibers containing poly[lactic-co- (glycolic acid)] and hydroxyapatite. Macromol Biosci. 2010 Feb 11;10(2):173–82.

104. Chen JP, Chang YS. Preparation and characterization of composite nanofibers of polycaprolactone and nanohydroxyapatite for osteogenic differentiation of mesenchymal stem cells. Colloids Surfaces B Biointerfaces. 2011 Aug 1;86(1):169–75.

105. Lu H, Zhang T, Wang XP, Fang QF. Electrospun submicron bioactive glass fibers for bone tissue scaffold. J Mater Sci Mater Med. 2009 Mar 20;20(3):793–8.

106. Xie J, Blough ER, Wang CH. Submicron bioactive glass tubes for bone tissue engineering. Acta Biomater. 2012 Feb 1;8(2):811–9.

107. Sharma J, Lizu M, Stewart M, Zygula K, Lu Y, Chauhan R, et al. Multifunctional nanofibers towards active biomedical therapeutics. Polymers (Basel). 2015 Feb 3;7(2):186–219.

108. Eccleston DS, Horrigan MC, Ellis SG. Rationale for local drug delivery. Semin Interv Cardiol. 1996 Mar;1(1):8–16.

109. Dzierzkowska E, Stodolak-Zych E. Electrospinning for drug delivery systems: potential of the technique. Eng Biomater. 2019;Vol. 22, no. 149.

110. Son YJ, Kim WJ, Yoo HS. Therapeutic applications of electrospun nanofibers for drug delivery systems. Vol. 37, Archives of Pharmacal Research. Springer; 2014. p. 69–78.

111. Yarin AL. Coaxial electrospinning and emulsion electrospinning of core-shell fibers. Vol. 22, Polymers for Advanced Technologies. John Wiley & Sons, Ltd; 2011. p. 310–7.

112. Elahi MF, Lu W. Core-shell Fibers for Biomedical Applications-A Review. J Bioeng Biomed Sci. 2013;03(01).

113. Abdullah MF, Nuge T, Andriyana A, Ang BC, Muhamad F. Core-Shell fibers: Design, roles, and controllable release strategies in tissue engineering and drug delivery. Vol. 11, Polymers. MDPI AG; 2019. p. 2008.

114. Klein S, Kuhn J, Avrahami R, Tarre S, Beliavski M, Green M, et al. Encapsulation of bacterial cells in electrospun microtubes. Biomacromolecules. 2009 Jul 13;10(7):1751–6.

115. Andriolo JM, Sutton NJ, Murphy JP, Huston LG, Kooistra-Manning EA, West RF, et al. Electrospun Fibers for Controlled Release of Nanoparticle-Assisted Phage Therapy Treatment of Topical Wounds. In: MRS Advances. Materials Research Society; 2018. p. 3011–7.

116. Karimi M, Sahandi Zangabad P, Ghasemi A, Amiri M, Bahrami M, Malekzad H, et al. Temperature-Responsive Smart Nanocarriers for Delivery of Therapeutic Agents: Applications and Recent Advances. Vol. 8, ACS Applied Materials and Interfaces. 2016. p. 21107–33.

117. Liu D, Yang F, Xiong F, Gu N. The smart drug delivery system and its clinical potential. Vol. 6, Theranostics. Ivyspring International Publisher; 2016. p. 1306–23.

118. Qu J, Zhao X, Ma PX, Guo B. Injectable antibacterial conductive hydrogels with dual response to an electric field and pH for localized "smart" drug release. Acta Biomater. 2018 May 1;72:55–69.

119. Rockwood DN, Chase DB, Akins RE, Rabolt JF. Characterization of electrospun poly(N-isopropyl acrylamide) fibers. Polymer (Guildf). 2008 Aug 26;49(18):4025–32.

120. Okuzaki H, Kobayashi K, Yan H. Thermo-responsive nanofiber mats. Macromolecules. 2009 Aug 25;42(16):5916–8.

121. Chou SF, Carson D, Woodrow KA. Current strategies for sustaining drug release from electrospun nanofibers. Vol. 220, Journal of Controlled Release. Elsevier B.V.; 2015. p. 584–91.

122. Chou SF, Woodrow KA. Relationships between mechanical properties and drug release from electrospun fibers of PCL and PLGA blends. J Mech Behav Biomed Mater. 2017 Jan 1;65:724–33.

123. Hossen S, Khalid Hossain M, Basher MK, Mia MNH, Rahman MT, Uddin MJ. Smart nanocarrier-based drug delivery systems for cancer therapy and toxicity studies: A review. 2019;

124. Jiang S, Liu F, Lerch A, Ionov L, Agarwal S. Unusual and Superfast Temperature-Triggered Actuators. Adv Mater. 2015 Sep;27(33):4865–70.

125. Kim YJ, Ebara M, Aoyagi T. Temperature-responsive electrospun nanofibers for "on-off" switchable release of dextran. Sci Technol Adv Mater. 2012;13(6).

126. Jiang H, Wang L, Zhu K. Coaxial electrospinning for encapsulation and controlled release of fragile water-soluble bioactive agents. J Control Release. 2014 Nov 10;193:296–303.

127. Song F, Wang XL, Wang YZ. Poly (N-isopropylacrylamide)/poly (ethylene oxide) blend nanofibrous scaffolds: Thermo-responsive carrier for controlled drug release. Colloids Surfaces B Biointerfaces. 2011 Dec 1;88(2):749–54.

128. Tran T, Hernandez M, Patel D, Burns E, Peterman V, Wu J. Controllable and switchable drug delivery of ibuprofen from temperature responsive composite nanofibers. Nano Converg. 2015;2(1).

129. Chen M, Dong M, Havelund R, Regina VR, Meyer RL, Besenbacher F, et al. Thermo-responsive core-sheath electrospun nanofibers from poly (N - isopropylacrylamide)/polycaprolactone blends. Chem Mater. 2010;22(14):4214–21.

130. Lin X, Tang D, Lyu H, Zhang Q. Poly(N-isopropylacrylamide)/polyurethane core-sheath nanofibres by coaxial electrospinning for drug controlled release. Micro Nano Lett. 2016 May 1;11(5):260–3.

Chapter 2: Electrospun fibers with an improved pore structure for controlled delivery of nanoparticles

Contributions

Zahra Mahdieh, University of Montana: Primary author responsible for development of project and design of experiments. Performed electrospinning processes and sample preparations, scanning electron microscopy, energy dispersive spectroscopy, confocal laser scanning microscopy, in vitro release studies, weight loss studies, Fourier transform infrared spectroscopy, X-ray diffraction analyses, tensile testing, and statistical analyses.

Andrij Holian, University of Montana: Supervised project development and experimental design. Reviewed final paper submission.

Somenath Mitra, New Jersey Institute of Technology: Provided resource support for BET nitrogen adsorption/desorption analyses and coupled plasma mass spectrometry.

Larisa Krishtopa, New Jersey Institute of Technology: Performed coupled plasma mass spectrometry.

Samar Azizighanad, New Jersey Institute of Technology: Performed BET nitrogen adsorption/desorption analyses.

Gretchen McCaffrey, University of Montana: Provided editorial guidance for preparation of paper.

Jim Driver, University of Montana: Provided training and resource support for scanning electron microscopy. Performed transmission electron microscopy.

Kevin Trout, University of Montana: Constructed electrospinning hardware and provided training for electrospinning.

Lou Harriette, University of Montana: Provided training for confocal laser scanning microscopy.

Hamilton Ray, University of Montana: Provided training for statistical analyses.

Monica Serban, University of Montana: Provided training and resources for tensile testing.

Chris Palmer, University of Montana: Provided training and resources for Fourier transform infrared spectroscopy.

Robert Walker, Montana State University: Provided resource support for field emission scanning electron microscopy.

Elif Roehm, Montana State University: Performed field emission scanning electron microscopy.

Abstract

Electrospun fiber meshes with controlled drug delivery properties have great potential for applications such as wound dressings, tissue engineering, and cancer treatment. However, controlling the drug release, especially from core-shell fibers, remains the main challenge. In this study, core-shell fibers were developed with silver nanoparticles (Ag NP, as an antibacterial agent) loaded in the core. To control the release rate, pore structure in the shell (diffusion pathway for Ag NP) was improved compared to previous studies by a novel use of ZnO NP combined with polyethylene glycol (as the porogen). Moreover, the diffusion/release rate of Ag NP from electrospun fibers was fine-tuned with variation in particle size. Fibers were loaded with three size compositions of 20 nm, 110 nm, or a mix of the two Ag NP inside the fiber core. Release studies showed fast, slow, and intermediate delivery rates obtained with the defined Ag NP. Fine-tuned release of Ag NP confirmed the formation of open pores within a stable shell structure because controlling the release rate was only possible through this well-defined release pathway. Furthermore, tensile strength analysis revealed excellent mechanical stability of the fibers after pore formation.

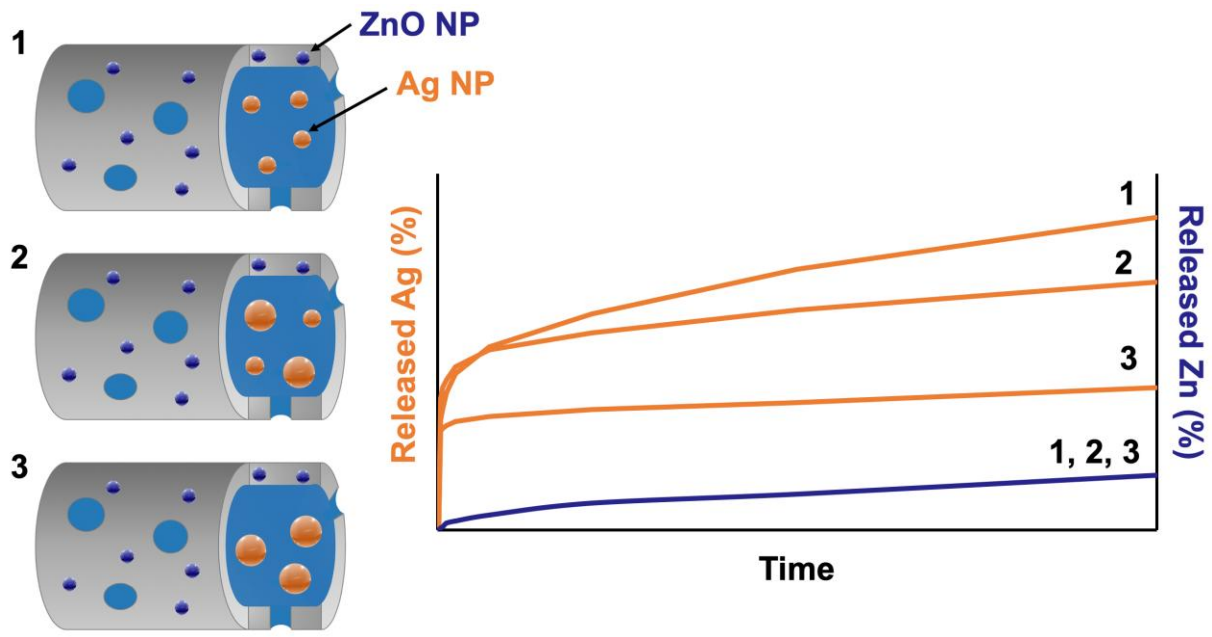

Ag: fast (1), intermediate (2), and slow (3) release of 20, 20+110, 110 nm Ag NP from the fiber core through pores. Zn: sustained release of ZnO NP from fiber shell.

Introduction

Among various methods of fabricating fiber meshes, electrospinning is the most popular process due to its simplicity, cost efficiency, versatility, and the possibility of large-scale production (1,2). Potential applications of electrospun fibers range from biomedical, filtration, energy, sensors, and food industry (3–5). Electrospun fibers are being primarily developed for biomedical applications due to their unique structure i.e. high surface area to volume ratio, high interconnected mesh porosity, and similar structure to the extracellular matrix (6,7). The distinguishing advantage of electrospinning for biomedical applications is the possibility of incorporating drugs into the fibers. Furthermore, development of coaxial electrospinning facilitates the ability to load various therapeutic agents, including fragile drugs and biomolecules, inside the fiber core (8).

In order to release the encapsulated agents from the fiber core, a porogen, which is usually a water-soluble polymer such as polyethylene glycol (PEG), needs to be added into the shell (9–13). The porogen dissolves (by selective dissolution) to form open pores required for the release of agents from the core. However, in practice, high percentages of porogen in the shell composition are needed to obtain open pores. Unfortunately, using high percentages of porogen results in fiber rupture or swelling, and failure of the shell structure. This failure in turn results in an uncontrolled and sudden release of agents within one or few hours (14–21). To control the release rate, therefore, it is crucial to form pores without disrupting the shell structure.

In this project, zinc oxide nanoparticles (ZnO NP) were included into the fiber shell to overcome the challenge of creating open pores without losing the fiber stability. ZnO NP have been used in electrospun fibers to improve the mechanical properties, but not in combination with porogen to form pores (22–24). Silver nanoparticles (Ag NP) were used as a model drug in

this study, but could be replaced by other therapeutic agents for different applications. Ag NP have been incorporated into electrospun fibers for their antiseptic, antibacterial, anti-inflammatory properties (25). However, the release rate of Ag NP from electrospun fibers has not been well controlled (26–34). In this study, commercially available Ag NP were used inside the core to control the release rate through the pores. Two different sizes of Ag NP were used in the core with the goal of fine-tuning the release rate. It was hypothesized that this unique structure would have two distinct delivery rates: (i) fast diffusion of smaller Ag NP through the formed pores, (ii) slow diffusion of larger Ag NP through the pores.

Materials and methods

Polycaprolactone (PCL, M_W = 45,000 g/mol), Poly(ethylene glycol) (PEG, BioUltra, Mw = 3,350 g/mol), Chloroform (biotechnology grade, ≥99.8%, 0.5-1.0% ethanol as stabilizer), N,N-Dimethylformamide (DMF, ReagentPlus, ≥99%), and fluorescein isothiocyanate diethylaminoethyl dextran (FITC–DEAE–Dextran, Mw = 70,000 g/mol) were purchased from Sigma-Aldrich, USA. Citrate coated silver nanoparticles (Ag NP, 20 nm and 110 nm diameter, 1 mg/mL) stabilized in 2 mM sodium citrate aqueous solution were obtained from NanoComposix (Biopure™, San Diego, CA, USA). Zinc oxide nanoparticles were obtained from Meliorum Technologies, Inc. (ZnO NP, 20 nm diameter, Rochester, NY, USA). Characterization information of ZnO NP and Ag NP are available in our previous studies (35,36). Ultrapure Mili-Q water, obtained from a Milli-Q water purifier (QGARD00D2, Millipore, USA), was used throughout this study.

Electrospinning of core-shell fibers

Data in Table 2.1 shows the sample designation and composition for each of the fabricated fiber meshes. Samples were designated according to the size of Ag NP used for their

fabrication. For the core feed fluids, different concentrations of Ag NP suspensions were prepared by diluting the stock suspension of the Ag NP concentrates in water. Ag NP were used as an antibacterial agent to be released from the core. For the shell feed fluids, a mixture of chloroform/DMF with a ratio of 17:10 was used as the solvent for different compositions of PCL, PEG and ZnO NP shown in Table 2.1.

An in-house built coaxial electrospinning instrument was used for fabrication of core-shell fibers. The spinneret-collector was arranged horizontally with a distance of 20 cm. A prebuilt blunt coaxial spinneret (100-10-COAXIAL-2016, ramé-hart instrument Co.) with a 20-gauge inner needle and a 16-gauge outer needle was used. Core and shell fluids were pumped into the inner and outer needles with the feeding rates of 0.4 mL/h and 1 mL/h, respectively. Fiber meshes were collected on a rotating drum (226 rpm, 5.08 cm diameter) that was covered with aluminum foil. The spinneret was connected to a DC power supply and the collector grounded. Applied voltages for different fiber compositions are shown in Table 2.1. Electrospinning was performed in an electrically-insulated plastic case and placed inside a laboratory safety hood (room temperature of 20°C and ambient humidity of 10%). Fiber meshes were fabricated by 1h of electrospinning. Then, fiber meshes were left inside the hood to dry overnight.

Table 2.1 Fabricated electrospun fiber meshes and their corresponding sample names

Sample	Core Composition (Particle Diameter)	Shell Composition			Voltage (KV)
		PCL (Wt%)	PEG (Wt%)	ZnO NP (Wt%)	
F-Ag20	0.02 Wt% Ag NP (20 nm)	14	7	1.6	20
F-Ag110	0.02 Wt% Ag NP (110 nm)	14	7	1.6	21
F-AgMix	0.01 Wt% Ag NP (20 nm) + 0.01 Wt% Ag NP (110 nm)	14	7	1.6	21
F-ZnO	water	14	7	1.6	17
F-PEG	water	14	7	-	16

Nanoparticles release rate and weight loss measurements

Samples with a size of 15 × 3 cm^2 were cut from the center of electrospun fiber meshes (F-Ag20, F-Ag110 and F-AgMix). Fiber meshes were placed in water for a few seconds and then quickly detached from the aluminum foil in water in order to obtain intact pieces of fiber meshes. The results reflect the average of three electrospun fiber meshes (error bars represent the standard deviation, SD, for n=3). Each sample was placed into a 50 mL conical centrifuge tube containing 20 mL water. Since these fibers could have various applications, water was chosen as the immersion media. Tubes were placed on a shaker (200 rpm, 0.12-inch orbit motion, Thermo Labline 4625 Titer Shaker, USA) inside an incubator (37°C). At predetermined periods of time, samples were gently taken out of the tubes and moved into new tubes containing 20 mL water and put back on the shaker at 37°C. The time periods of 1 h, 2 h, 4 h, 8 h, 24 h, 3 days, 7 days,

and 14 days were selected to obtain a time course that reflects potential wound dressing application periods. Supernatants were analyzed for Ag and Zn using an inductively coupled plasma mass spectrometer (ICP-MS, Algilent 7900, CA, USA). The released percentages of Ag at each time interval (Ag_r) were calculated as follows:

$$\% Ag_r = \frac{Ag_s}{Ag_t \times \frac{A_s}{A_t}} \times 100 \quad (1)$$

Where Ag_s is the mass (g) of Ag measured by ICP-MS in 20 mL supernatants at each time interval; Ag_t is the mass (g) of Ag in the original electrospun fiber mesh as calculated by the mass of Ag that was injected into the inner needle during 1 h of electrospinning (Ag_t (g) = core solution feeding rate (mL/h) × electrospinning time (h) × concentration of Ag in the core solution (g/g) × density of the core solution (g/mL)); A_s is the sample area (a 15 × 3 cm^2 piece cut out of the fiber mesh); and A_t is the original electrospun fiber mesh area (thin edges of fiber meshes were not included in A_t). The denominator of formula 1 represents the mass of Ag in the sample before immersion. The density of the core solution was assumed to be 1 g/mL (density of water) due to the low concentration of Ag (0.02 Wt% Ag).

The released percentages of Zn were calculated differently since the density of the shell solution could not be assumed to be 1 g/mL because of complexity of the solution. The released percentages of Zn at each time interval (Zn_r) were calculated as follows:

$$\% Zn_r = \frac{Zn_s}{Zn_t} \times 100 \quad (2)$$

$$Zn_t = M_s \times \frac{M_{ZnO}}{M_{ZnO} + M_{PCL} + M_{PEG} + M_{core}} \quad (3)$$

Where Zn_s is the mass (g) of Zn measured by ICP-MS in 20 mL supernatants at each time interval, Zn_t is the total mass (g) of Zn in the original fiber mesh. Zn_t (g) was calculated using

formula 3 where, M_s is the mass (g) of the sample before immersion; M_{ZnO}, M_{PCL}, and M_{PEG} are the masses of ZnO, PCL, and PEG used for making the fiber mesh, respectively; and M_{core} is the mass of the core solution injected during 1 h of electrospinning. The mass of Zn in the original fiber mesh (Zn_t) was calculated as the mass (g) of the sample before immersion (M_s) multiplied by the mass ratio of ZnO NP to the fiber mesh (formula 3). It was assumed that all of the solvents were evaporated from the fiber mesh (thus, the denominator of formula 3 represents the weight of the fiber mesh).

Sample weight loss was determined by measuring the difference between the weight of samples before and after one and two weeks of immersion in water. Percent weight loss was calculated using the following formula.

$$\%Weight\ Loss = \frac{M_0 - M_i}{M_0} \times 100$$

(4)

Where M_0 is the sample weight before immersion and M_i is the sample weight after one or two weeks of immersion. M_0 was measured by weighing the sample attached to the aluminum foil and then subtracting the weight of the aluminum foil.

Electron Microscopy and fluorescent imaging of the fibers

The morphology of the electrospun fiber meshes was evaluated using a field emission scanning electron microscope (FESEM, Carl Zeiss AG, SUPRA^{TM} 55VP) and a scanning electron microscope (SEM, Hitachi S-4700) in the secondary electron mode. Samples were coated with gold/palladium prior to imaging. SEM and FESEM were performed on samples before immersion, and after one- and two- week immersion. Average fiber diameter and pore size were calculated by measuring at least 150 points of FESEM images using image analyzer

software (ImageJ, National Institutes of Health, USA). Elemental mapping of the fiber mesh surfaces was determined using energy dispersive spectroscopy (EDS, TESCAN VEGA3) performed in conjunction with SEM images.

The core-shell structure of the fibers was further evaluated using a confocal laser scanning (CLS) microscope (Zeiss LSM 880). For this, fluorescent dextran (FITC–DEAE–Dextran, 0.01%) was dissolved in the core fluid prior to the electrospinning. The core syringe and tubing were covered to prevent bleaching of the fluorescent dye. Electrospinning procedures were performed with the same conditions and fibers were collected directly on cover glasses by passing the cover glass quickly in front of the spinneret close to the collector. Fibers without added fluorescent dextran to the core fluid were also collected as the control.

The core-shell structure of the fibers was determined by transmission electron microscopy (TEM, Hitachi H-7500). A piece of electrospun fiber mesh was embedded in a cold-setting embedding resin (1232 Epofix^{TM} Kit, PA, USA) at room temperature in order to avoid melting of fibers. Slides of 50 nm thickness were cut from the mounted fiber mesh for the TEM imaging.

Nitrogen adsorption/desorption analysis

The Brunauer–Emmett–Teller (BET) surface area of samples was measured using nitrogen physical adsorption method with a gas sorption analyzer (Autosorb iQ-MP, Quantachrome Instruments, FL, USA). Samples were degassed in vacuum at 30°C for 24 hours prior to the measurement. BET surface area measurement was performed at International Union of Pure and Applied Chemistry (IUPAC) standard temperature and pressure (STP) with 52-point adsorption and 15-point desorption isotherms. Two samples of 1×1 cm^2 squares were cut from the fiber mesh (F-Ag20) and detached from the aluminum foil without any immersion. One

sample was analyzed without any treatment (before pore formation) and the other sample was analyzed after one-week immersion in water (after pore formation).

Fourier transform infrared (FTIR) spectroscopy

FTIR spectroscopy was performed on fiber meshes before immersion and after one- and two-week immersion. FTIR spectra of samples were obtained in the attenuated total reflection (ATR) mode (Thermo Scientific iD7 ATR accessory for a Nicolet™ iS5 Spectrometer). Dried pieces of fiber mesh with no additional processing were loaded on the ATR accessory for the measurement.

X-ray diffraction (XRD) analysis

XRD analysis was performed to assess the crystal structure of fiber meshes before immersion and after one- and two-week immersion. A PANanalytical X'Pert PRO X-ray diffractometer was used for XRD analysis. The 2θ range was 10°-50° with a step size of 0.0170°. X-rays were generated with a Co tube with Fe_{β} filter (run at 40 kV and current of 45 mA). XRD spectra were converted to the spectra recorded by Cu-K_{α} using X'Pert HighScore Plus© software.

Tensile test

Tensile tests were performed using a Discovery HR2 hybrid rheometer (TA Instruments, New Castle, DE, USA) at a strain rate of 10 mm/min and with 10N load cell. Fiber meshes were cut into strips (10×30 mm^2) and quickly detached from aluminum foil in water. Samples were immersed in water (for one and two weeks compared to no immersion) under similar conditions as used in the nanoparticles release study. Samples were taken out of the water and placed on flat

tissues to dry. Samples were kept for five days at 20°C and 10% humidity prior to the tensile test. Four replicates were carried out for each measurement. Data is represented as mean ± SD.

Statistical analyses

Statistical analyses were performed using a one- or two-way ANOVA followed by individual comparison of groups using Holm-Sidak's multiple comparisons test (PRISM v.7.0, GraphPad, San Diego, CA, USA). The Holm-Sidak's multiple comparison results are reported at supplementary data of chapter 2. A statistical significance level of 5% ($p < 0.05$) was defined. The minimum number of replicates was three. Values were reported as M ± SD.

Results and Discussion

Fiber structure

The morphology of fabricated fibers was evaluated via FESEM imaging. Figures 2.1A and 1B show FESEM micrographs of sample F-Ag20 at 10KX and 30KX magnifications, respectively. Figure 2.1A reveals the overall morphology of electrospun fibers to be continuous and randomly aligned. In addition, relatively few beads were detected throughout the fiber mesh during the FESEM imaging. The average fiber diameter was measured to be 698 ± 529 nm using ImageJ analyzer software. The fiber diameter distribution is shown in Figure 2.2. Fibers had a wide diameter distribution of diameters with the majority fiber diameter frequency of 600-800 nm. Figure 2.1B shows the surface of the sample F-Ag20 fibers at higher magnification. Some microcracks can be seen on the surface of thinner fibers in addition to some dimples on thicker fibers. These irregular surface features have been suggested to be the result of the phase separation (between PCL and PEG) during the electrospinning (37). The fiber structure was sufficient to achieve the controlled delivery goals in this research; however, it is likely that the

fiber structure could be further improved by using an electrospinning instrument with an isolated chamber and controlled processing conditions.

Fiber structures of samples F-Ag110 and F-AgMix were similar to the sample F-Ag20 since similar electrospinning conditions were applied in order to avoid creating extra parameters. Only minor voltage adjustments were applied for electrospinning of samples in order to generate similar fiber structures. Therefore, data is only shown for sample F-Ag20 and not for samples F-Ag110 and F-AgMix since they were similar.

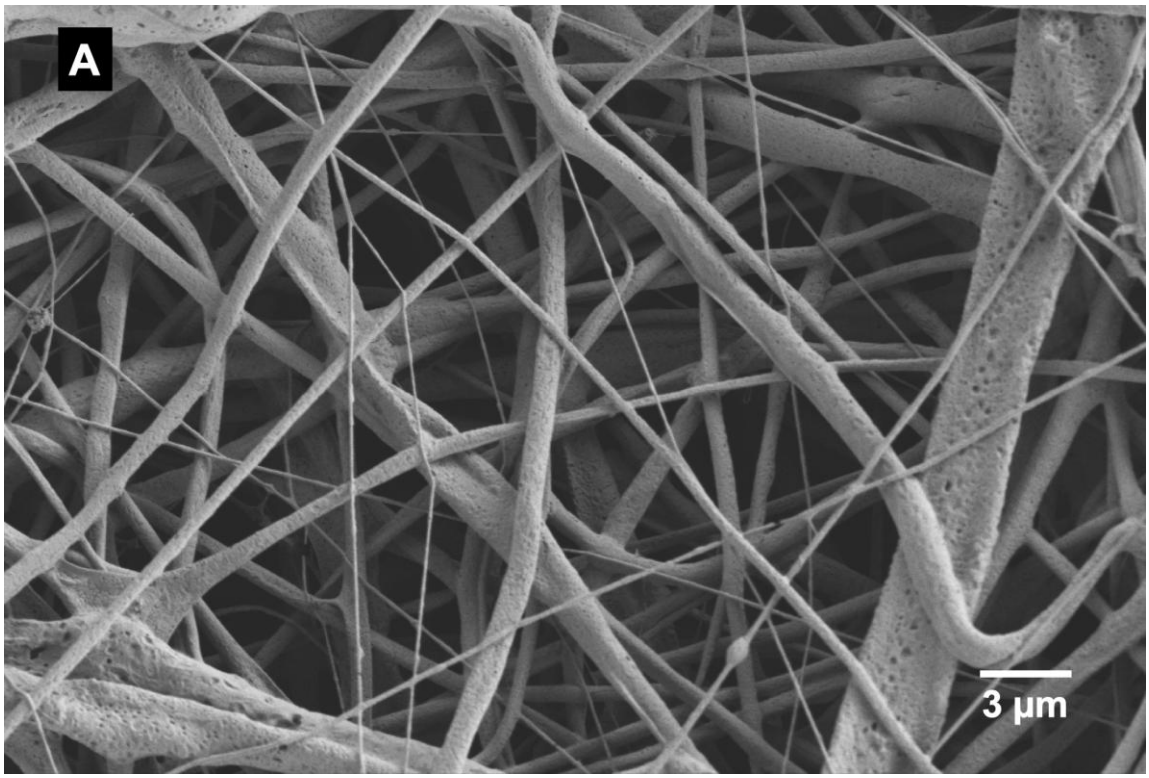

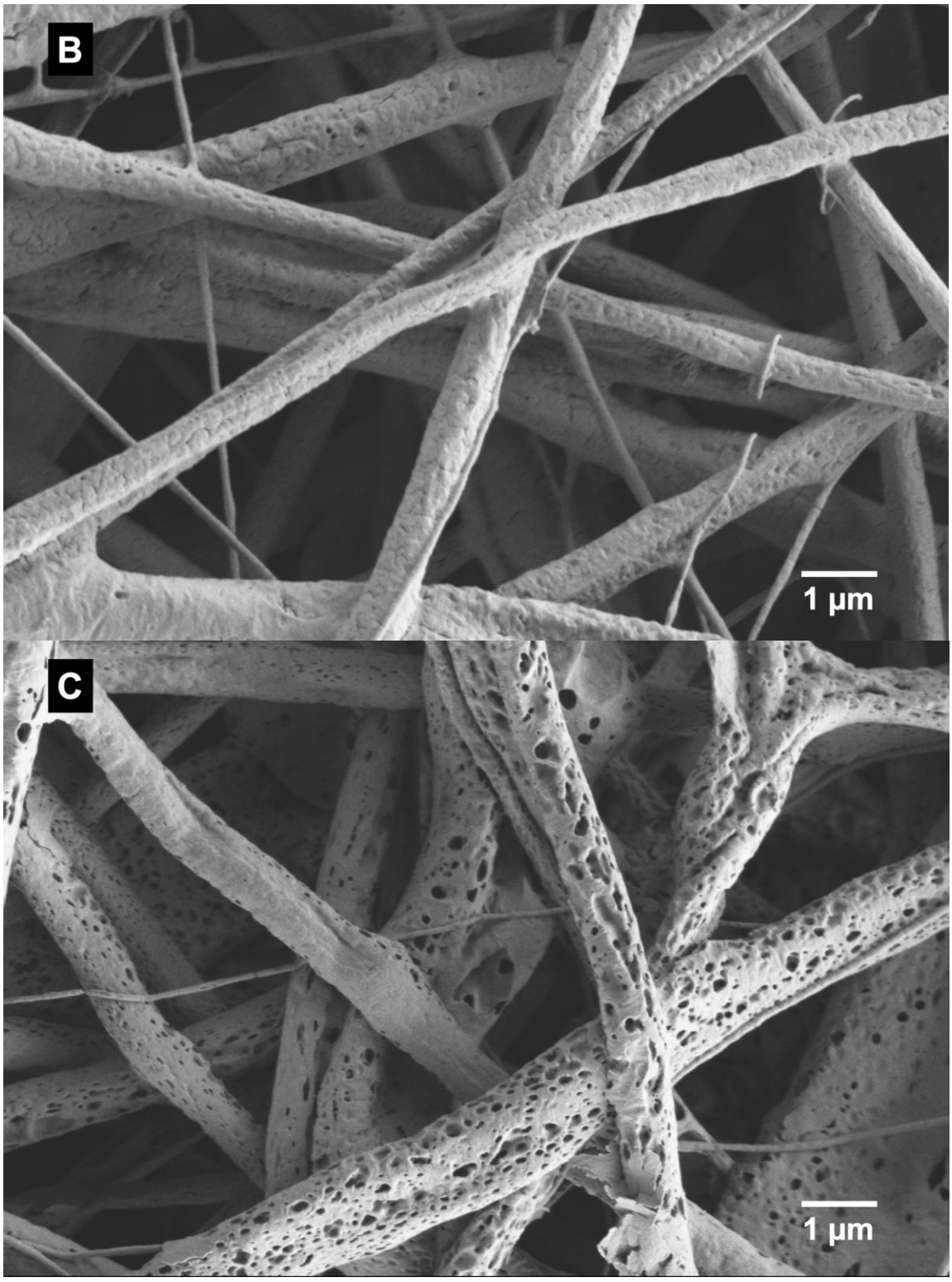
B
1 µm
C
1 µm

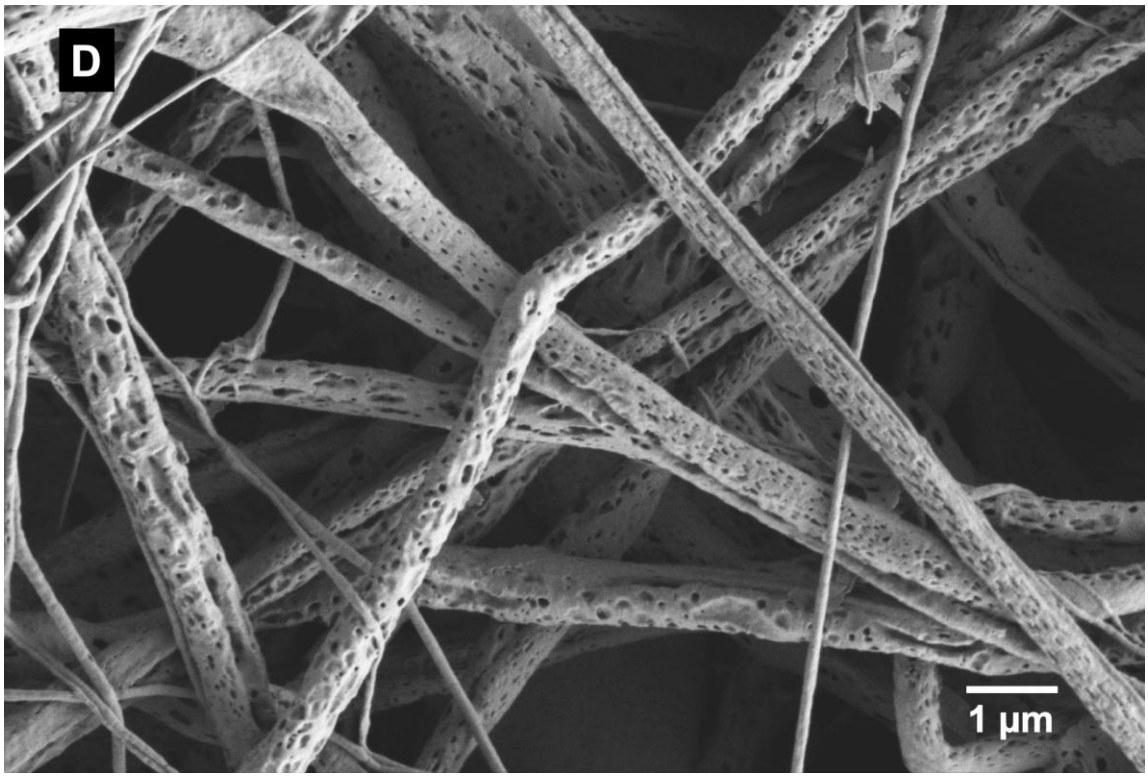

Figure 2.1 FESEM micrographs of fiber mesh F-Ag20: (A) before immersion at 10KX magnification, (B) before immersion at 30KX magnification (C) after one-week immersion at 30KX magnification, and (D) after two-week immersion at 30KX magnification. F-Ag20 is the core-shell structured electrospun fiber mesh containing 20 nm silver nanoparticles in the core.

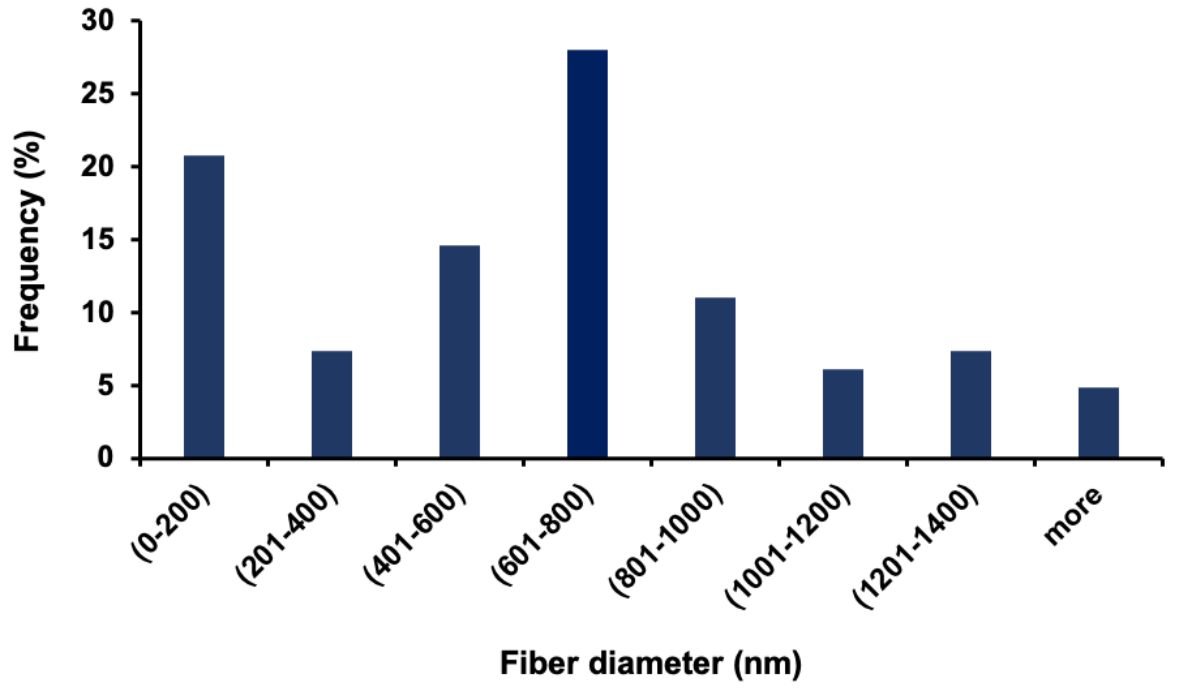

Figure 2.2 Fiber diameter distribution of fiber mesh F-Ag20 before pore formation. F-Ag20 is the core-shell structured electrospun fiber mesh containing 20 nm silver nanoparticles in the core.

Formation of core-shell structure throughout the fibers was evaluated using CLS microscopy. Figures 2.3A, 2.3B and 2.3C show the fluorescent mode, optical mode and overlay of the two (fluorescent and optical) images for sample F-Ag20, respectively. The fluorescent image (Figure 2.3A) represents the core, which contains fluorescent dextran, and is dispersed throughout the fiber length. The optical mode image (Figure 2.3B) represents the shell part of the fiber. The overlay image (Figure 2.3C) represents the core-shell structure of the fiber. A discrete core-shell margin can be seen in the overlay image verifying that no mixing of core and shell solutions occurred during the electrospinning process. The core and shell diameters changed when moving the image plane throughout the fiber thickness suggesting a cylindrical fiber shape.

Moreover, no fiber breaks or core leakage were detected during the CLS microscopic imaging of the fibers.

In order to verify that none of the materials used for fabrication of fibers had any background fluorescence, control samples, which contained no fluorescent dextran, were also imaged. All CLS micrographs of control samples were devoid of any fluorescence in the fluorescent mode confirming absence of fluorescence background staining (data not shown).

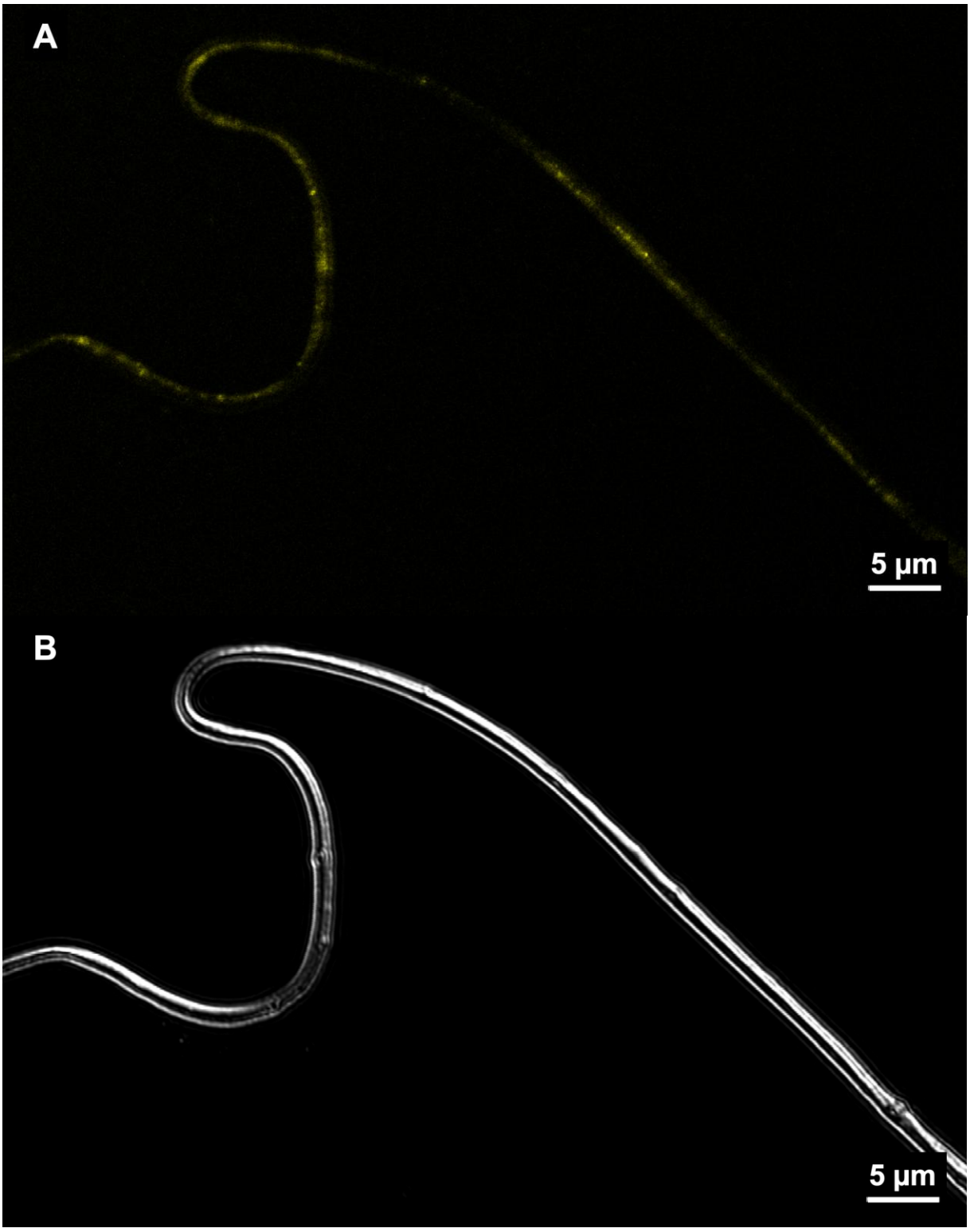
A
5 µm
B
5 µm

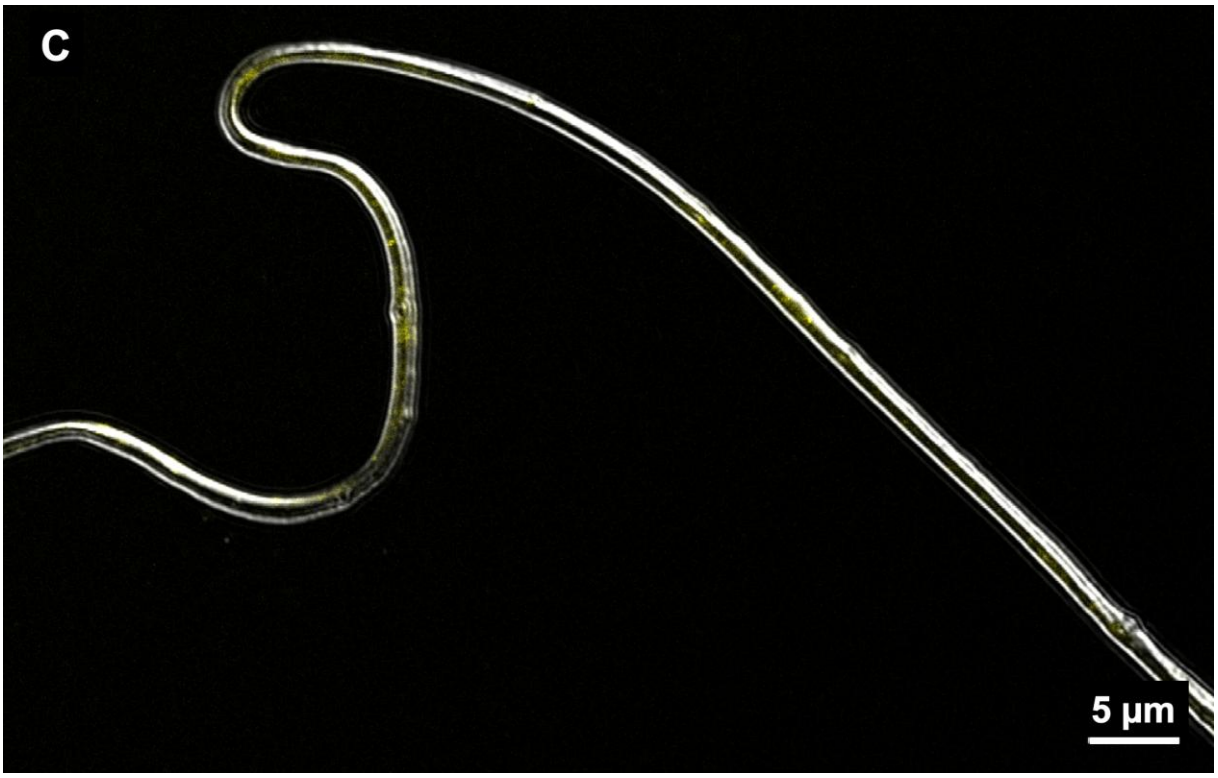

Figure 2.3 CLS micrographs of a fiber of sample F-Ag20: (A) fluorescent mode image, (B) optical mode image, and (C) overlay of fluorescent and optical images. F-Ag20 is the core-shell structured electrospun fiber mesh containing 20 nm silver nanoparticles in the core.

The cross-section of fibers was assessed for more details on the core-shell structure via TEM microscopy. Figure 2.4 shows a TEM micrograph of a fiber cross-section for sample F-Ag20. It can be seen in the image that the fibers had a cylindrical core-shell structure. A discrete, smooth margin could be seen between the core and the shell. No pores could be seen on the outer surface of the fiber. The dimensions of the core and the shell are shown in Figure 2.4. The average fiber shell thickness and core diameter measured using ImageJ analyzer software were 125 ± 17 nm and 547 ± 50 nm, respectively.

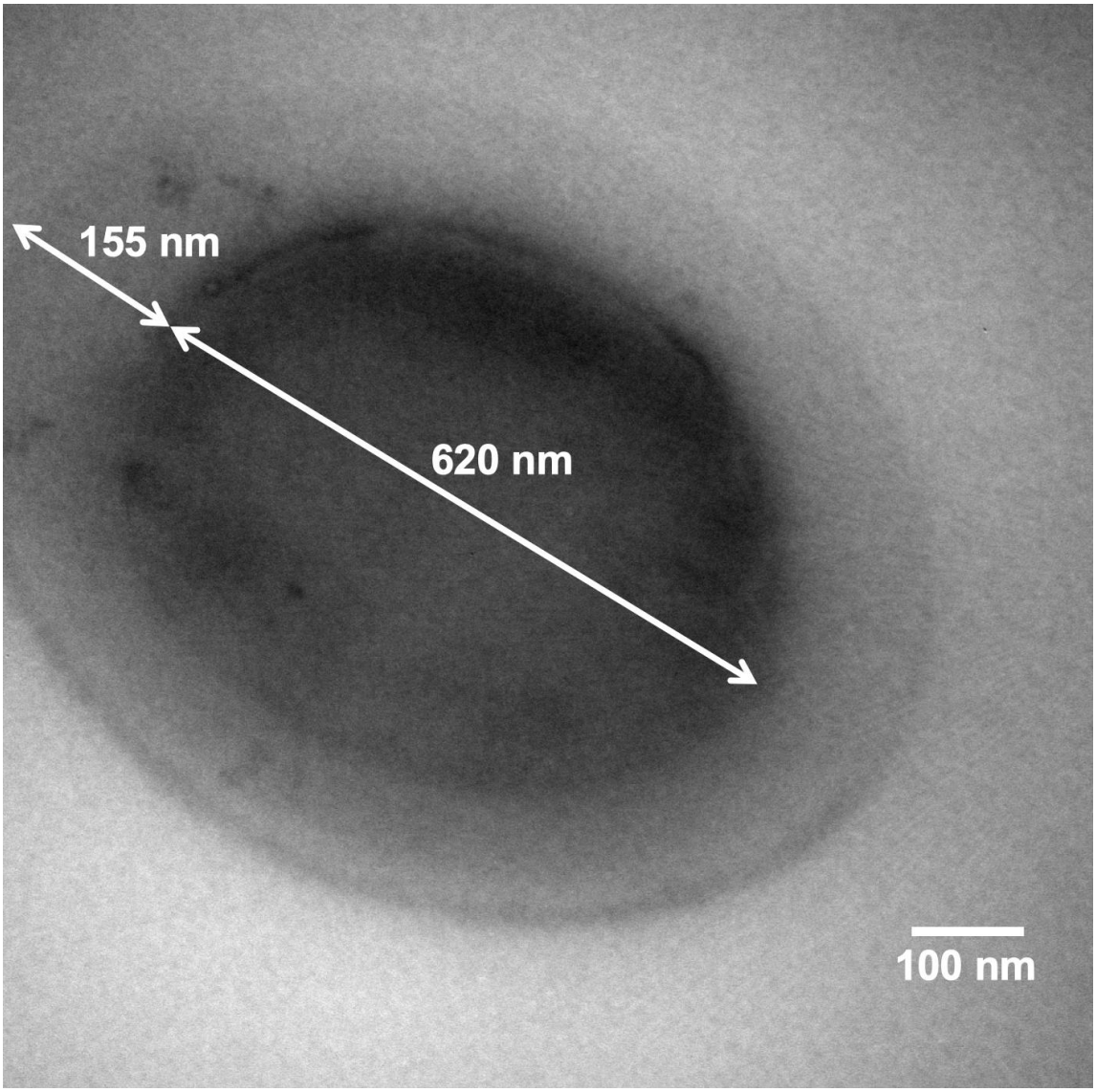

Figure 2.4 TEM micrograph of a fiber cross-section of sample F-Ag20 before pore formation (100KX, 75KV). Dimensions of the core and the shell are indicated in the image. F-Ag20 is the core-shell structured electrospun fiber mesh containing 20 nm silver nanoparticles in the core.

EDS micrographs were obtained from the fiber meshes in order to demonstrate that Ag was loaded inside the core of the fibers throughout the fiber mesh. Ag potentially could leak out of the core through various defects such as mixing of the core and shell solutions during the electrospinning, from torn or non-continuous fibers, flawed shell structure, etc. The data in

Figures 2.5A and 2.5B show the EDS layered image of the fiber mesh F-Ag20 with a surface area of 340 × 340 μm^2 and its corresponding elemental analysis table, respectively. As can be seen in the elemental analysis table shown in Figure 2.5B, no Ag was detected on the surface of the fibers confirming an intact core-shell structure of the fibers throughout the fiber mesh. An EDS control image was taken of a dried droplet of Ag NP suspension on a piece of aluminum foil to confirm that Ag in (in the form of Ag NP) can be detected by EDS (data not shown). Moreover, the red color in the EDS layered image represents Zn. It can be seen that Zn, which is in the form of ZnO NP, was dispersed all through the fibers' shell. Other detected elements in the elemental analysis table are from aluminum foil substrate (Al, Fe), palladium coating (Pd), or the shell polymer (O).

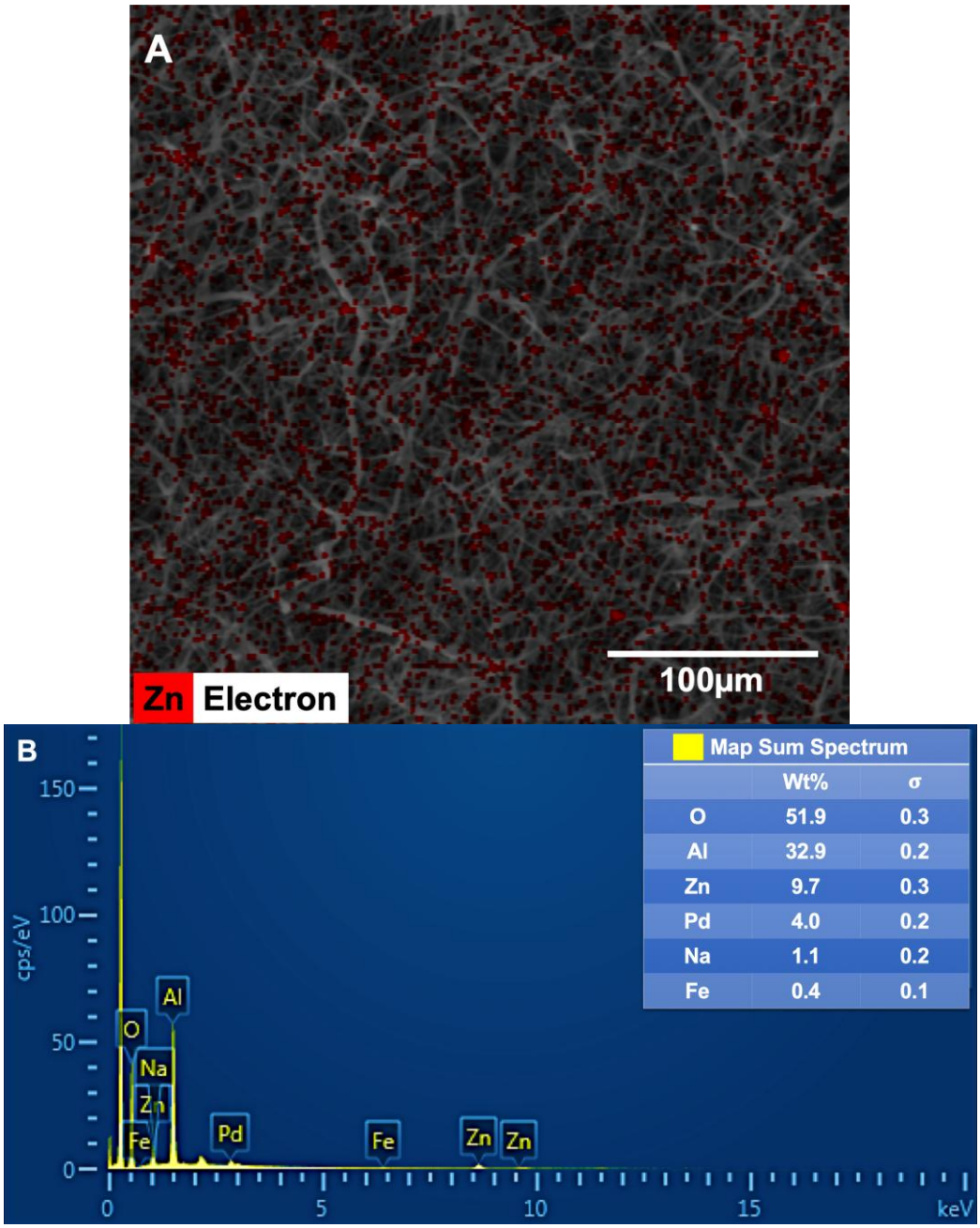
A
100µm
Zn Electron
B
Map Sum Spectrum
Wt% σ
O 51.9 0.3
Al 32.9 0.2
Zn 9.7 0.3
Pd 4.0 0.2
Na 1.1 0.2
Fe 0.4 0.1
cps/eV
150
100
50
0
O
Al
Na
Zn
Fe
Pd
Fe
Zn
Zn
0
5
10
15
keV

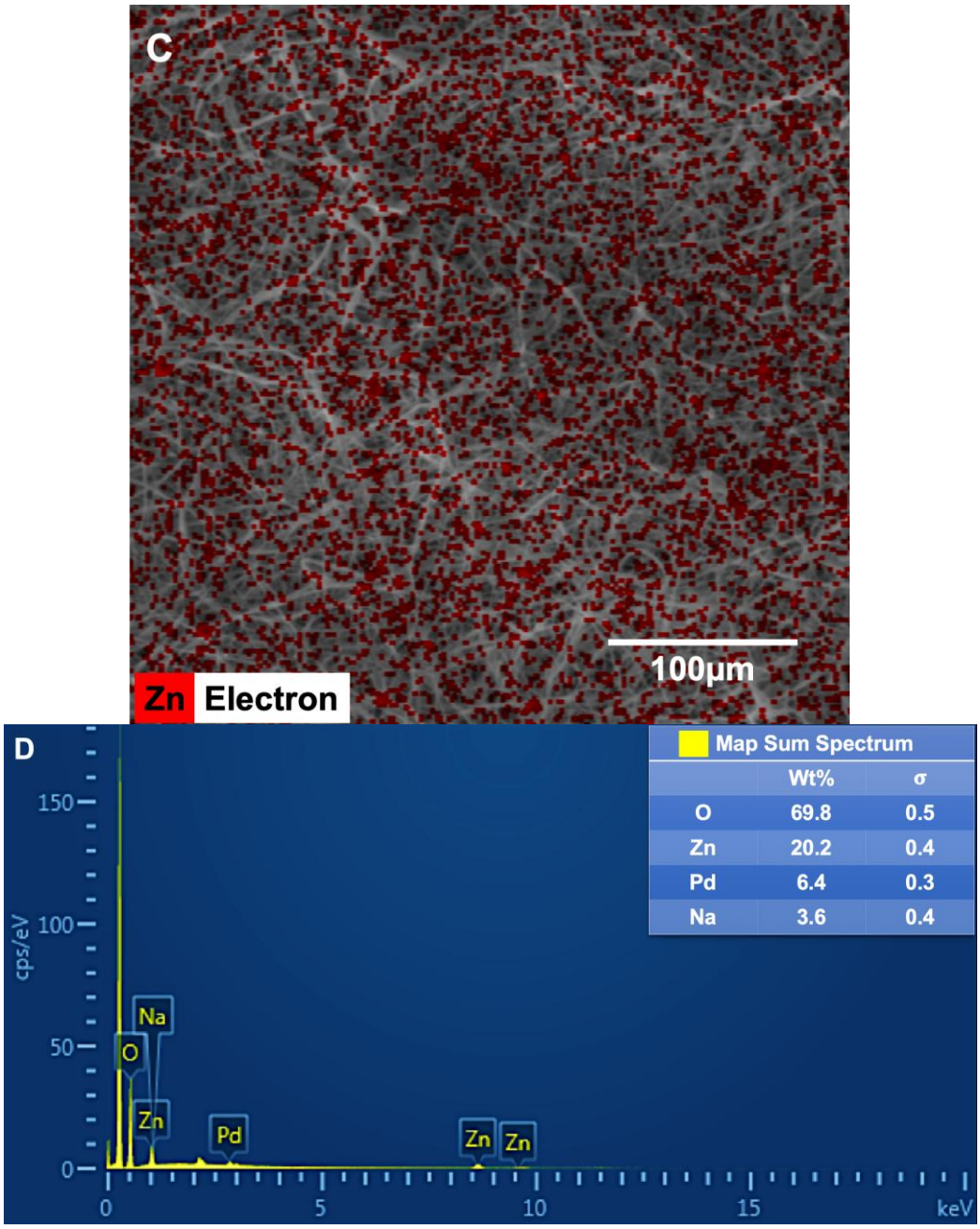

Figure 2.5 (A) SEM-EDS image of fiber mesh F-Ag20 before pore formation, and (B) its corresponding table of elemental analysis, (C) SEM-EDS image of fiber mesh F-Ag20 after pore formation (two-week immersion), and (D) its corresponding table of elemental analysis. The color red in the layered SEM-EDS images represents the Zn mapping. F-Ag20 is the core-shell structured electrospun fiber mesh containing 20 nm silver nanoparticles in the core.

Pore structure

Improvement of pore structure using ZnO NP

In order to obtain an open pore structure without disturbing the fiber integrity, ZnO NP were added to the shell simultaneous with the use of PEG as porogen. Our studies showed that a small percentage of ZnO NP (1.6%) and PEG (7%) successfully resulted in forming pores that were connected to the core. However, in previous studies high percentage of porogens was needed to form open pores, which caused rupture/swelling and failure of fiber (10,19,20,38,39). The data in Figures 2.6A and 2.6B show SEM micrographs of electrospun fibers of samples F-PEG and F-Ag20 after pore formation, respectively. The shell composition of sample F-PEG is different from sample F-Ag20 only in the absence of ZnO NP, i.e. sample F-PEG has no ZnO NP. Comparing the pore structure of samples F-PEG and F-Ag20 reveals the effect of the ZnO NP on the pore structure. In sample F-PEG, which only had PEG as the porogen, pores were shallow and small, while, in sample F-Ag20, which had both PEG and ZnO NP, pores were deep and large. Therefore, addition of ZnO NP increased the depth and the size of the pores. Moreover, it can be seen in Figure 2.6B that use of the low percentage of porogens in our studies resulted in preservation of the shell structure after removal of porogens.

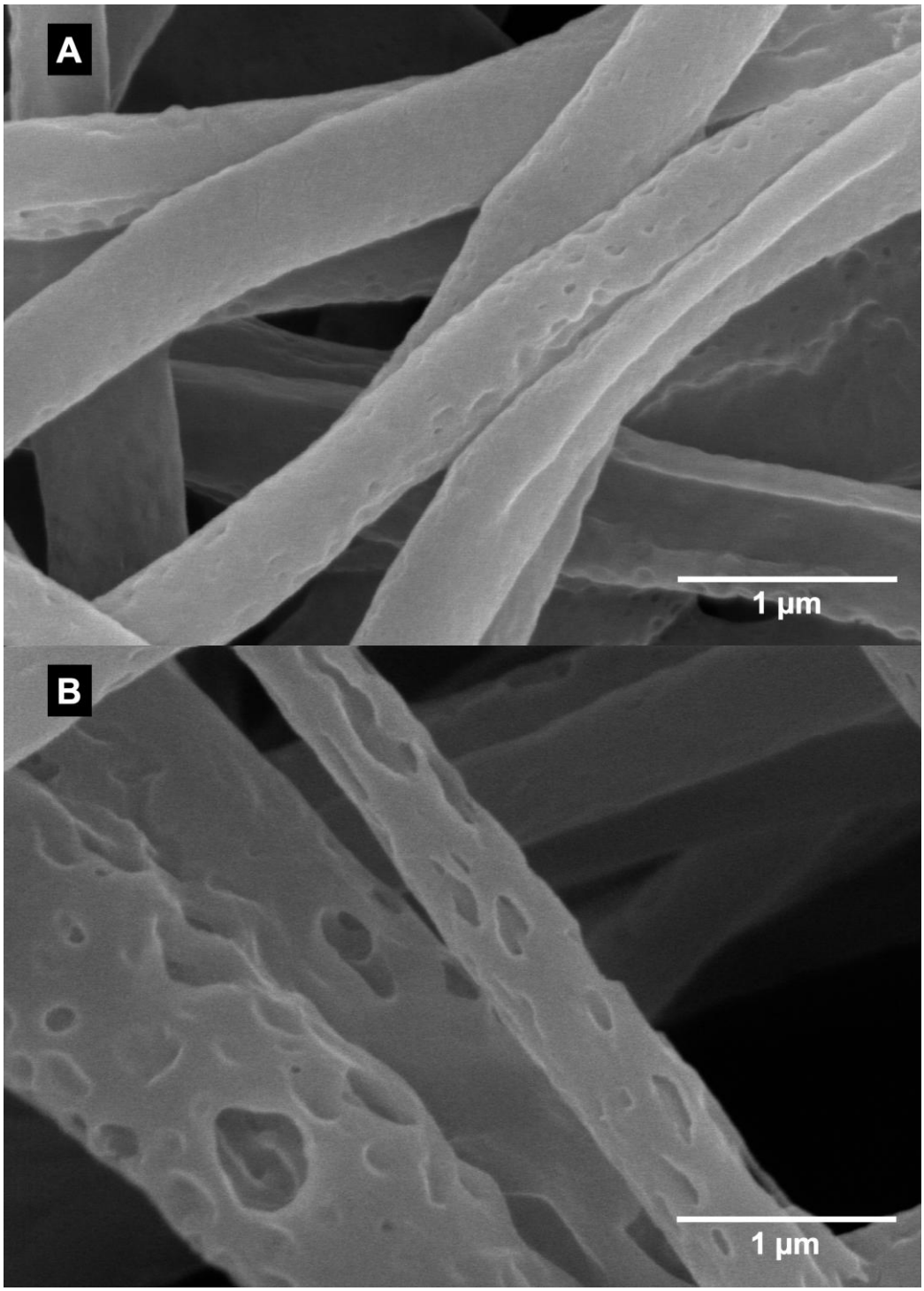

Figure 2.6 SEM micrographs (30KX, 10KV) of pore structure after one-week immersion of the fiber meshes: (A) F-PEG (PEG used as porogen) and (B) F-Ag20 (PEG and ZnO used simultaneously).

The pore structure during two weeks of immersion was evaluated using FESEM microscopy. The data in Figures 2.1C and 2.1D show FESEM micrographs of fibers (sample F-Ag20) after one and two weeks of immersion, respectively. It can be seen that pores were formed in the fibers with immersion. The data in Figure 2.6B shows the one-week immersed pore structure at higher magnification. It can be seen that pores did not have a constant diameter going inward through the fibers. In other words, pores were uneven tunnels through the shell thickness. Moreover, pores were mostly elongated along the length of fibers and their diameter at the surface of fibers were measured using ImageJ analyzer software. The pore width (perpendicular to the fiber length) and length (parallel to the fiber length) diameter distribution are shown in Figure 2.7. The average pore width and length were measured to be 70 ± 57 nm and 127 ± 64 nm, respectively. Consequently, FESEM results confirmed the formation of mostly oblong pores in the surface of the fibers.

Moreover, it can be seen in the FESEM micrographs of the immersed fibers (Figures 2.1C and 2.1D) that the intact fiber structure was preserved after one or two weeks of immersion and no further change in fiber diameter was observed. The measured total weight loss of sample F-Ag20 after one and two weeks of immersion were 27.9 ± 0.45% and 28.5 ± 0.78%, respectively. The weight loss during the first week of immersion is most likely due to the pore formation i.e. dissolution of PEG. The small amount of weight loss during the second week of immersion (0.6%) is consistent with the FESEM pictures of these fibers (Figure 2.1D) showing no degradation or loss of fiber integrity during the immersion.

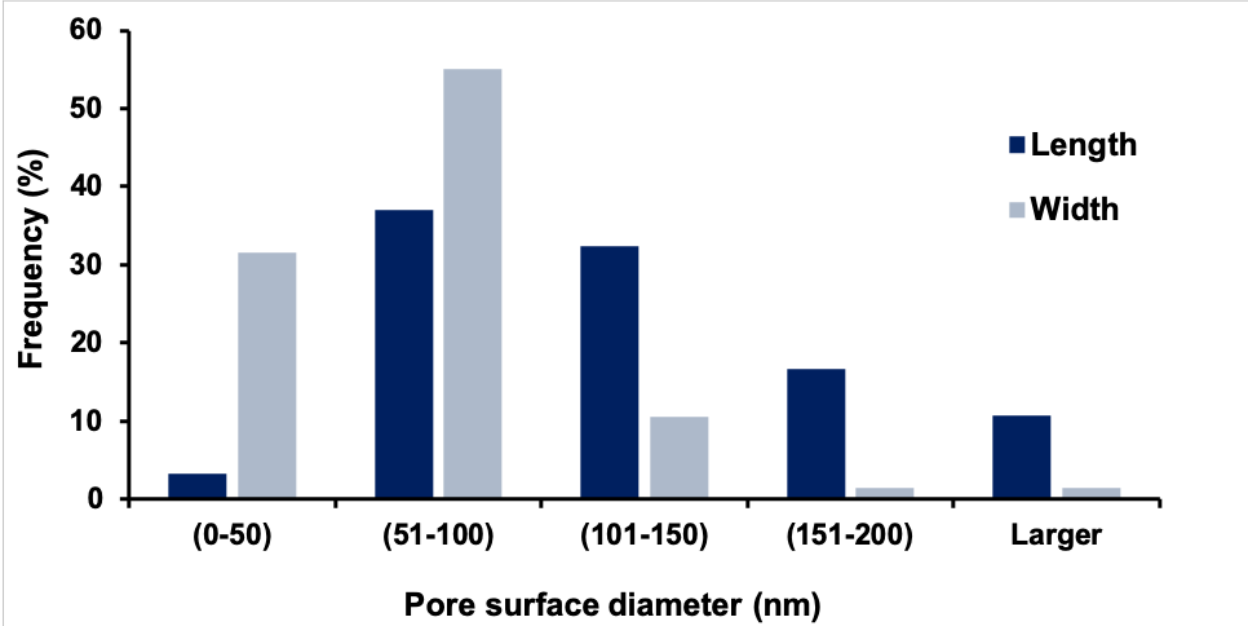

Figure 2.7 The length and width distribution of the pores formed on the fiber mesh F-Ag20 after one-week immersion measured from FESEM images using ImageJ software. F-Ag20 is the core-shell structured electrospun fiber mesh containing 20 nm silver nanoparticles in the core.

The changes of fiber mesh surface area due to the pore formation was measured via BET analysis. The measured surface area and pore volume of sample F-Ag20 before and after one-week immersion are shown in Table 2.2. The surface area of the fiber mesh had a 5.9-fold increase after pore formation. The pore volume of fiber mesh had a 6.3-fold increase after pore formation. These results are consistent with the large number of pores found in the FESEM imaging of F-Ag20 fibers after pore formation.

Table 2.2 BET surface area and pore volume measurements of fiber mesh F-Ag20 before pore formation and after pore formation (one-week immersion). F-Ag20 is the core-shell structured electrospun fiber mesh containing 20 nm silver nanoparticles in the core.

	Before pore formation	**After pore formation**
Surface area (m^2/g)	29.4	173
Pore volume (cm^3/g)	0.012	0.076

Figures 2.5A and 2.5C show the EDS layered images of the fiber mesh F-Ag20 before and after pore formation, and Figures 2.5B and 2.5D show their corresponding elemental analysis, respectively. It can be seen in both EDS layered images that ZnO NP were dispersed uniformly throughout the fiber structure both before and after pore formation. Surprisingly, elemental analysis indicated 9.7 Wt% Zn for fibers before pore formation (Figure 2.5B) and 20.2 Wt% Zn for fibers after pore formation (Figure 2.5D), indicating that a higher amount of Zn was detected after pore formation.

The higher amount of Zn detected after pore formation suggests two possibilities: first, ZnO NP were mostly located at the inner part of the shell because EDS collected signals from deeper parts of the fibers after pores were formed; second, ZnO NP were mostly associated in the PCL phase rather than the PEG phase because EDS collected more signals from the PCL matrix after removal of PEG during pore formation. Considering each of these possibilities, two different mechanisms could explain the deeper pore structure in the presence of the ZnO NP.

First, during electrospinning, when the fiber jet forms, solvents move toward the surface of the fibers and evaporate. PEG, which has a lower molecular weight compared to PCL, migrates with the solvents toward the fiber surface. Therefore, when the phase separation of PCL and PEG occurs, PCL-rich areas are formed at inner parts of the fibers and PEG-rich areas are formed at the surface of the fibers. However, when ZnO NP are present, ZnO NP associate with PEG and hinder the diffusion of PEG. ZnO NP, which are the heaviest components of the shell solution, may sink into the shell solution and keep the PEG associated deeper in the shell. Subsequently, pores, which are the emptied spaces formed by selective dissolution of PEG, are deeper in the presence of ZnO.

Second, association of ZnO NP with the PCL decreases the interfacial energy of the PCL and PEG phases. Therefore, there is a decreased need for recession of the PEG phase toward the fiber surface in order to reach a stable energy state, i.e. the PEG phase forms deeper in the fibers. After removal of the PEG from the PCL matrix via selective dissolution, the phase boundary of PCL and PEG becomes the pore's surface area. The lower interfacial energy, i.e. larger phase boundary in the PCL-ZnO/PEG system is consistent with the high surface area of fibers measured by BET after pore formation. In addition, the second mechanism can be viewed from the kinetic of phase separation. During the electrospinning, fast evaporation of solvents (i.e. concentration changes) results in a phase separation of the porogen and the shell polymer. The fast evaporation of solvents (in the range of milliseconds) favors spinodal phase separation rather than binodal phase separation, which results in matrix-dispersed phase morphologies rather than co-continuous. Therefore, closed or shallow pores form by removal of the porogen (40,41). However, presence of ZnO NP could alter the kinetic toward binodal phase separation, which allows for coarsening of the PEG phase. Therefore, open or deep pores form by removal of PEG.

Either or both of these mechanisms could result in the pore depth increase. However, the second mechanism could be more prevalent since no burst release of ZnO NP was seen in this study, i.e. not many of ZnO NP were associated with PEG, which dissolves within the minutes of immersion in water (42). Further studies are needed to determine the effects of ZnO nanoparticles on the phase separation PCL/PEG during the electrospinning process.

Release of nanoparticles

Release of Ag

In order to fine-tune the Ag NP release rates, fibers were loaded with 20 nm Ag NP, 110 nm Ag NP, and a mixture of the two Ag NP in their core. A two-week release study was performed to evaluate the release profile of Ag (in the form of nanoparticles and/or ion) from the fiber meshes. Fiber meshes were immersed in water (shaking at 37°C) and water samples were collected and analyzed using ICP-MS for the presence of Ag at the predetermined time intervals. Shorter time intervals were chosen for the first day of the release study in order to investigate the presence of the burst release stage in the release profile. Burst release is an initial fast release of the drug in the early stage of the drug delivery before reaching a stable release rate (43).

Burst release stage: The Ag release profile during the first 8 hours of immersion is shown in Figure 2.8A. A burst release of Ag can be seen at one hour of immersion for all three samples. The burst release seen in such core-shell electrospun fibers is thought to be due to the fast release of a part of the drug that is located close to the surface of the fibers, after a fast dissolution of PEG (44). During the burst release stage (first hour), samples F-Ag20, F-Ag110, and F-AgMix released 28%, 24%, and 33% of Ag, respectively. According to the Einstein-Stokes equation, diffusion coefficient is inversely related to the particle size (45). Therefore, it was expected that the 20 nm Ag NP would release the fastest, 110 nm Ag NP would release the

slowest, and the mixture of these two Ag NP would have an intermediate release rate (46). However, the amount of released Ag observed at the burst release stage was not related to the size of the Ag NP loaded inside the fibers. The amount of released Ag during the primary stage was the lowest for F-Ag110, which is in accordance with the slower diffusion of larger Ag NP from the fibers. This result suggests that a larger size of Ag NP loaded in fibers could reduce the burst release. The Ag release rate at the burst release was fastest for F-AgMix, in contrast to the expectation that the 20 Ag NP (sample F-Ag20) would release fastest. In addition, it should be noted that the differences in the burst release rate of the different samples were not large.

We propose that the Ag burst release rate was related to the quality of the fibers (number of beads and homogeneity of fibers). The higher burst release from fiber meshes with lower fiber quality could be because Ag NP located at the site of the inhomogeneity and beads release faster due to the thinner shell (shorter diffusion distance), higher number of Ag NP (higher concentration gradient) and more core fluid (higher flow velocity) (45). This hypothesis is consistent with the SEM assessment revealing the lowest fiber quality for F-AgMix, compared to the samples F-Ag20 and F-Ag110. This result implies that the burst release stage was affected by the uncontrolled environmental condition of the electrospinning in this study. We suggest that using an electrospinning instrument with an isolated chamber and controlled environmental condition would result in a reduction of the Ag burst release.

Sustained release stage: The Ag release profile of the samples during the two-week immersion period is shown in Figure 2.8B. It can be seen in Figure 2.8B that after the burst release, all samples enter a second stage of sustained Ag release for the rest of the immersion period (two weeks). During the second stage, samples F-Ag20, F-AgMix, and F-Ag110 released 51%, 29%, and 12% of Ag NP mass, respectively. The cumulative Ag release after two weeks of

immersion was 79%, 62%, and 36% for samples F-Ag20, F-AgMix, and F-Ag110, respectively. The amount of released Ag and the slope of the release curves were inversely related to the size of Ag NP, i.e. smaller Ag NP had a faster release rate. The size of Ag NP was the only difference between the compositions of these three samples. The shell pore size (diffusion path) was kept constant in all samples by using the same amount of PEG and ZnO in the shell solution, in addition to equivalent electrospinning procedures. Therefore, it can be concluded that the size of Ag NP was the controlling factor for the diffusion of Ag NP out from the fiber core and through the shell. The 20 and 110 nm Ag NP had fast and slow diffusion rates through the pores, respectively. These results suggest that various release rates of the Ag NP (or possibly, any other drug in the form of nanoparticles) can be obtained by altering the size of the applied Ag NP. Moreover, simultaneous use of 20 and 110 nm Ag NP resulted in an intermediate release rate, suggesting that a summative release rate can be obtained by simultaneous use of Ag NP with various sizes.

It is possible that the Ag release is in the form of ion rather than nanoparticles. However, according to a study performed by Wang et al (47) for measuring the dissolution rate of 30 nm Ag NP of a similar brand and citrate coating, the dissolution rate of the 20 nm Ag NP used in our study should be in the range of 0.14 μg/mL after two weeks of immersion. The cumulative amount of Ag released from F-Ag20 fiber meshes was measured to be 17 μm/mL (79%) after two weeks of immersion, which is much higher than 0.14 μg/mL. Therefore, it can be concluded that the release mechanism of Ag was mainly by diffusion of Ag NP through the pores located in the shell. In other words, the dissolution of Ag NP and diffusion of Ag ions had a negligible effect on the release results. Moreover, the dissolution rate is even lower for 110 nm Ag NP, due

to their lower surface area, compared to 20 nm Ag NP. Hence, the dissolution of 110 nm Ag NP and its ion diffusion should not be considered as an effective release mechanism.

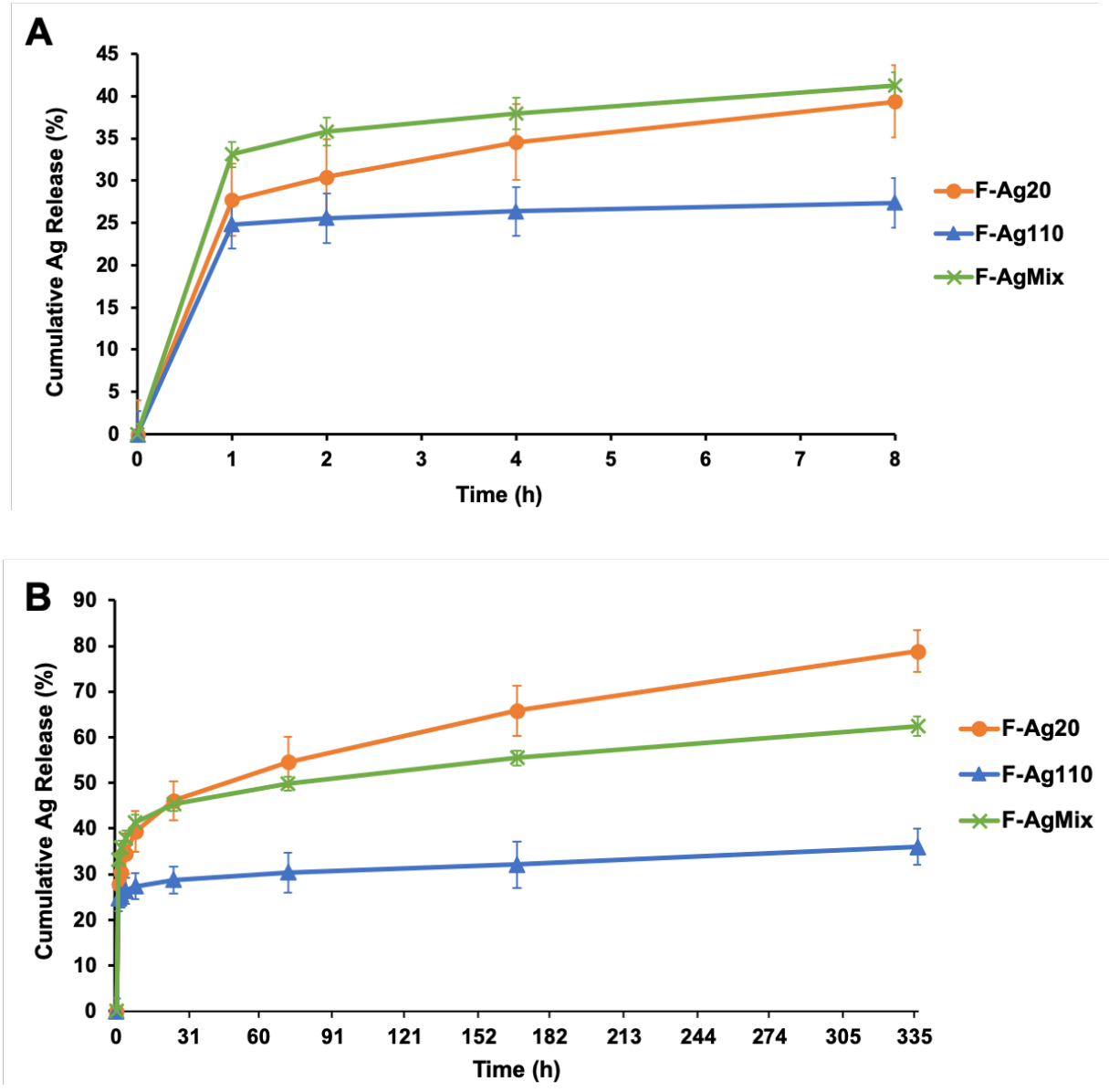

Figure 2.8 Percent cumulative release of Ag from fiber meshes of F-Ag20 (●), F-Ag110(▲), and F-AgMix (**X**) during immersion: (A) first 8 hours and (B) two weeks. Error bars represent standard deviation of three measurements. F-Ag20, F-Ag110, and F-AgMix are the core-shell

structured electrospun fiber meshes containing 20 nm, 110 nm, and a mixture of both silver nanoparticle sizes in the core, respectively.

Release of Zn

The amount of Zn released in water from the fiber meshes was measured in addition to the Ag in the release study. The cumulative release profile of Zn during two weeks of immersion is shown in Figure 2.9. The Zn release profile was similarly slow and sustained in all samples and showed no significant difference (the error bars overlap). The ZnO NP associated to the PEG phase were anticipated to be released in the early stage of immersion period by the fast dissolution of PEG in water. However, no burst release was seen in the release profile of Zn, implying that most of ZnO NP were associated with the PCL phase of the fiber shell. The higher association of ZnO NP with PCL was also supported by the EDS elemental mapping results (Figure 2.5D) showing a higher weight percentage of Zn on the surface of fibers after two weeks of immersion (when PEG was removed from the shell), compared to non-immersed fibers (Figure 2.5B).

Leaching or desorption of ZnO NP exposed on the surface of fibers is suggested to be the release mechanism of Zn (48). Shell composition and structure of fibers were similar for samples F-Ag20, F-Ag110, and F-AgMix, resulting in similar condition for Zn release from the fiber shell. This was confirmed by the similar Zn release rate in all fiber meshes during two weeks of immersion. The cumulative release of Zn was about 14% after two weeks of immersion, which was slower than the Ag release due to the different release mechanisms i.e. Ag NP diffuse through the pores located in the shell, while Zn ions leach out of the shell matrix (PCL phase).

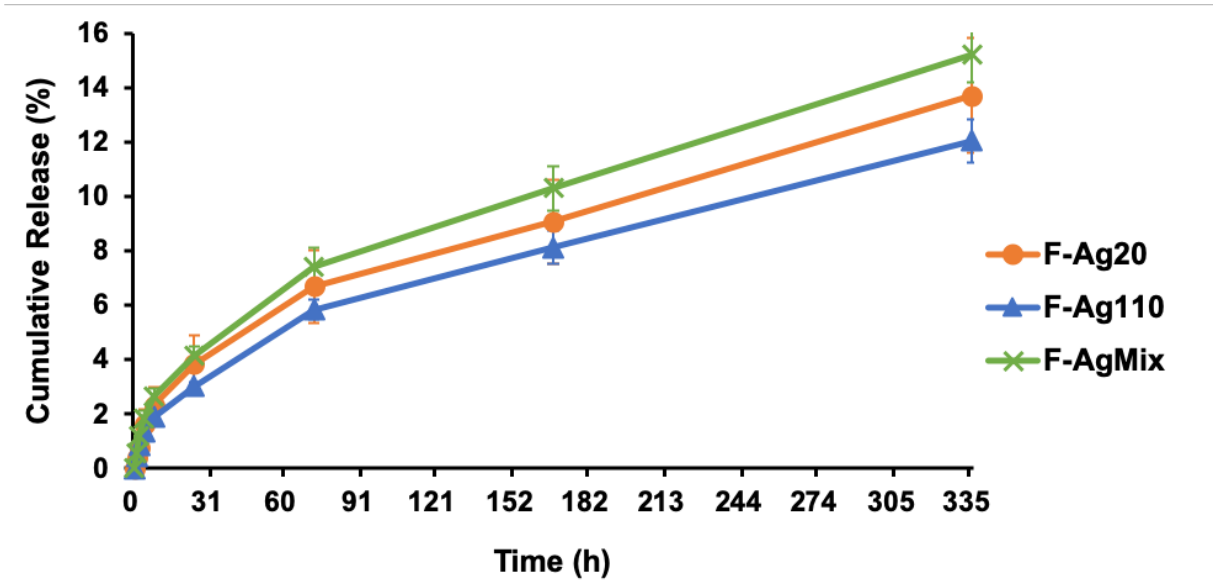

Figure 2.9 Percent cumulative release of Zn from fiber meshes of F-Ag20 (●), F-Ag110(▲), and F-AgMix (**X**) during two weeks of immersion. Error bars represent standard deviation of three measurements. F-Ag20, F-Ag110, and F-AgMix are the core-shell structured electrospun fiber meshes containing 20 nm, 110 nm, and a mixture of both silver nanoparticle sizes in the core, respectively.

Molecular structure

The surface functional groups of fiber meshes before immersion and after one- and two-week immersion were assessed using FTIR analyses (Figure 2.10). The band seen at 1722 cm^{-1} is related to the C=O stretching of ester carbonyl group. A small decrease was seen in the band at

1722 cm^{-1} after one- and two-weeks immersion. Decreases seen in the C=O stretching of the PCL suggest an interaction between the PCL carbonyl groups and ZnO NP. (This interaction could be a physical interaction due to Vander Waals forces (49).) A suggested schematic to explain this interaction is shown in Figure 2.11 (49). The suggested interaction is consistent with the decrease seen in the broad 400-700 cm^{-1} band, which is related to stretching of the Zn-O bond. During immersion, polymer chains can move and interact with ZnO NP. The decrease of Zn-O bond intensity is larger for the one-week immersion, compared to the two-week immersion. This shows a better interaction of ZnO-PCL after one week and its subsequent weakening after two weeks of immersion.

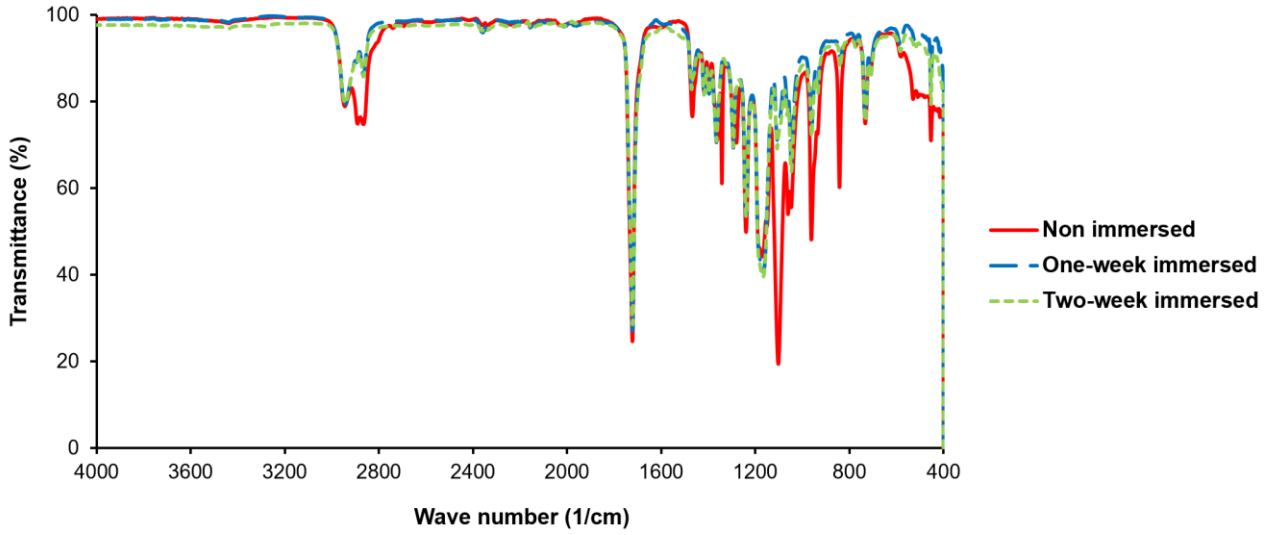

Figure 2.10 FTIR spectra of fiber mesh F-Ag20: before immersion (——), one-week immersed (— —), and two-week immersed (- - -). F-Ag20 is the core-shell structured electrospun fiber mesh containing 20 nm silver nanoparticles in the core.

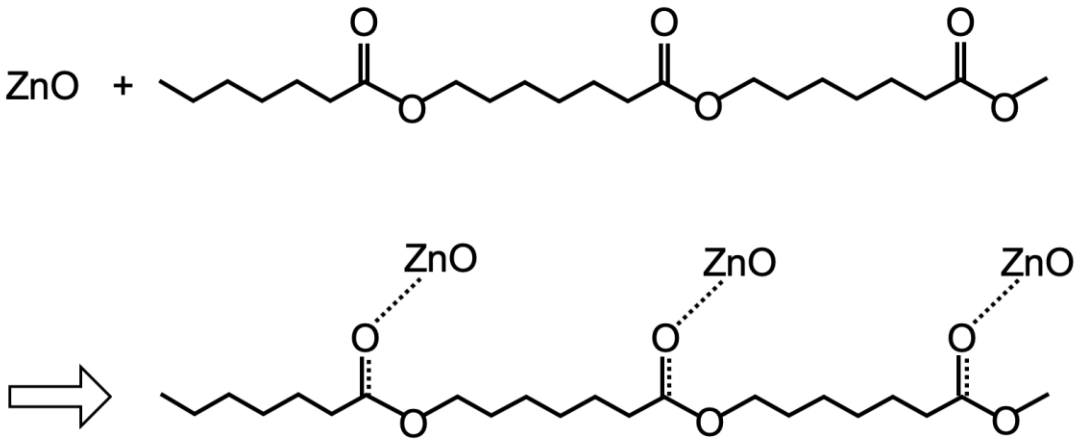

Figure 2.11 Schematic presentation of ZnO NP and PCL polymer chain interaction (adapted from (49)).

Crystal structure

The effect of immersion on the crystal structure of electrospun fibers was studied by XRD. Figure 2.12 shows the XRD diffractograms of non-, one- and, two-week immersed F-Ag20 fiber meshes. Three peaks at 21.4°, 22° and 23.7° seen on all three diffractograms correspond to (110), (111) and (200) planes of PCL orthorhombic crystal structure, respectively (50). The intensity of these three peaks are the lowest for non-immersed fibers, showing the lowest crystallinity of PCL in the fibers without immersion. While, after one week of immersion, the intensity of PCL peaks (21.4°, 22° and 23.7°) increased, showing an increase in PCL crystallinity. The explanation for the lowest intensity of PCL peaks for non-immersed fibers could be that during electrospinning, mobility of the polymer chains is restricted by the presence of ZnO NP, as well as, fast evaporation of solvents, resulting in a lower crystallinity (49). However, the higher intensity seen after one-week immersion suggests an annealing effect of immersion at 37°C for the polymer chains to reorient into higher crystallinity state (lower energy

state). The immersion temperature of 37°C is higher than the glass transition temperature of PCL (-60°C), in which PCL polymer chains have higher mobility.

The intensity of the PCL peaks (21.4°, 22° and 23.7°) had small decreases after two weeks of immersion, relative to one-week, although the intensity was still higher for the two-weeks immersed samples compared to non-immersed samples. This decrease could be due to the start of degradation of PCL after two weeks of immersion.

Two peaks at 19.2° and 23.3° seen in the XRD diffractograms of non-immersed fibers correspond to the PEG. The PEG peak at 23.3° has an overlap with the PCL peak at 23.7°. The PEG peak at 19.2° was eliminated from the XRD diffractograms of one- and two-week immersed samples showing that during immersion, PEG was extracted from the fibers by dissolving in water. However, the intensity of the PCL and PEG overlapping peak at 23.7° increased in the one- and two-week immersed fibers. The increase in the intensity of peak 23.7° occurred simultaneously with the increase of the two other PCL peaks at 21.4° and 22°. Therefore, the intensity increase seen in the peak at 23.7° is related to the increase of PCL crystallinity, which has compensated for the loss in the intensity of the peak at 23.3° due to the removal of PEG from the structure.

In the XRD diffractograms of non-immersed fibers, three peaks at 31.8°, 34.4° and 36.3° correspond to (100), (002) and (101) planes of ZnO wurtzite crystal structure, respectively. These three peaks are lost from XRD patterns of the fibers after immersion. In addition, a peak has appeared at 12.9° on the XRD patterns of the fibers after one- and two- weeks immersion, which is related to $Zn_5(OH)_8(CH_3COO)_2.2H_2O$ (51). This result shows an interaction of Zn with oxygen of the ester bond in the PCL molecular chains, which is consistent with the FTIR spectral results.

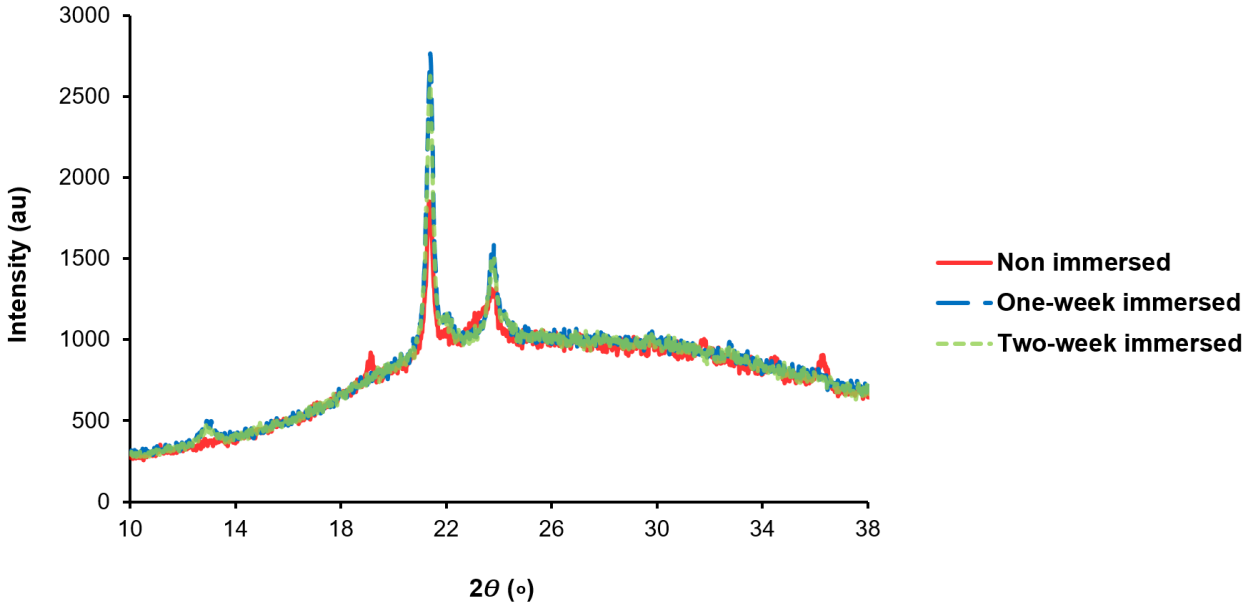

Figure 2.12 XRD diffractograms of fiber mesh F-Ag20: before immersion (——), one-week immersed (— —), and two-week immersed (- - -). F-Ag20 is the core-shell structured electrospun fiber mesh containing 20 nm silver nanoparticles in the core.

Mechanical properties

Tensile studies were conducted to determine the stability of the fiber meshes after immersion. The stress-strain curves of the fiber meshes before immersion and after one- and two-week immersion are presented in Figure 2.13. The average elongation at break, ultimate tensile strength, and Young's modulus obtained for four samples are presented in Table 2.3. The average elongation at break of fibers increased 115% and 76% after one- and two-week immersion, respectively. In addition, the average tensile strength of fibers increased 59% and 16% after one- and two-week immersion, respectively. Finally, the average Young's modulus of fibers decreased 6% and 44% after one- and two-week immersion, respectively.

The unexpected observed improvement of mechanical properties following immersion could be due to the removal of residual stresses by an annealing effect of immersion. Residual

stresses are created in the fibers due to two simultaneous factors. First, during the electrospinning process, solvents evaporate in a fraction of second not allowing enough time for polymer chains to move. Consequently, polymer chains rapidly solidify (or freeze) into a high energy, metastable phase (52). Second, deformation caused by the whipping motion of the polymer solution jet during electrospinning applies stress onto the polymer chains. Subsequently, when fiber meshes are immersed at 37°C, polymer chains can move and reorient to a state with lower energy, which is the crystalline phase. The annealing process is also facilitated by the plasticizing or lubricating effect of water. The presence of water molecules between the polymer chains helps the polymer chains to slip past each other (1,53). This hypothesis is consistent with the XRD results showing an increased crystallinity of PCL after one- and two-week immersion.

The annealing process can also increase the tensile strength by improving the interface of the reinforcement (ZnO NP) and the polymer matrix (PCL) (54), which is consistent with the FTIR results showing an improvement of ZnO-PCL interactions. The high increase of mechanical properties suggests that both these mechanisms (increase of PCL crystallinity and improvement of ZnO-PCL interaction) occurred during the immersion.

Further studies are needed to fully evaluate the molecular structure and mechanical property changes occurring in the individual fibers during immersion. In general, there are not many studies reporting changes of fiber's mechanical properties with immersion. Some studies report that mechanical properties deteriorate with immersion, which is suggested to occur due to degradation of polymer (50,55,56). However, other studies have reported increases of the Young's modulus (50,56), tensile strength (50,55), elongation at break (55,57,58), or impact energy (59) with water immersion. The plasticizing effect of water was suggested to be responsible for improvement of plasticity in those studies (55,59).

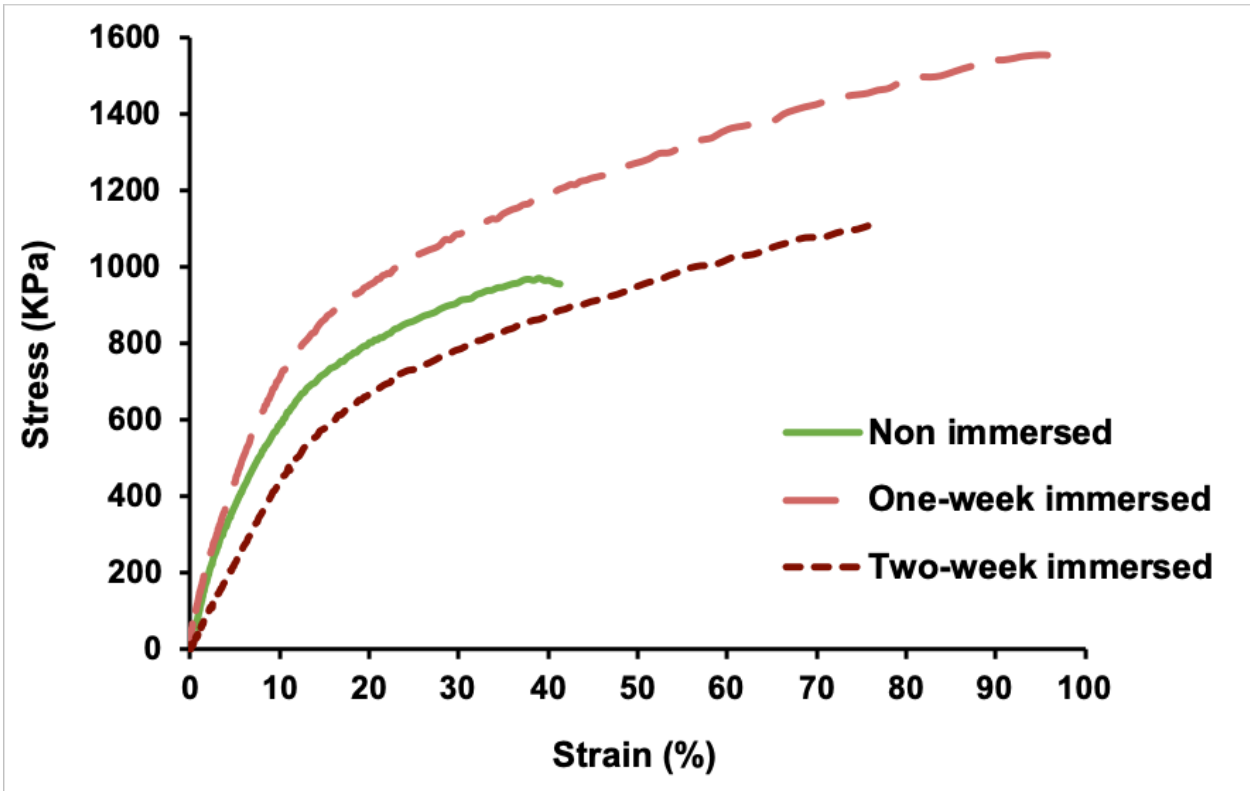

Figure 2.13 Tensile stress-strain curves of fiber mesh F-Ag20: before immersion (——), one-week immersed (— —), and two-week immersed (- - -). F-Ag20 is the core-shell structured electrospun fiber mesh containing 20 nm silver nanoparticles in the core.

Table 2.3 Measured tensile properties (elongation at break, ultimate tensile strength, and Young's modulus) of non-, one-, and two-week immersed fiber mesh F-Ag20. The SD for n=4 is reported in the parentheses for each measurement. F-Ag20 is the core-shell structured electrospun fiber mesh containing 20 nm silver nanoparticles in the core.

	Elongation at Break (%)	**Ultimate Tensile Strength (KPa)**	**Young's Modulus (KPa)**
Non-immersed	41.33 (±6.58)	919.46 (±72.99)	88.56 (±1.62)
One-week immersed	89.10 (±12.36)	1466.55 (±123.23)	83.40 (±18.52)
Two-week immersed	72.79 (±4.11)	1067.60 (±53.77)	49.37 (±2.43)

Conclusions

The main achievement of this research was forming deep discrete pores in the fiber shell using ZnO NP to control the delivery rate of therapeutic agents. The delivery rate was fine-tuned via loading different sizes of Ag NP inside the core of coaxial electrospun fibers. This research showed that fast, intermediate, and slow delivery of drug could be achieved by using different sizes of Ag NP. Moreover, it was shown that preserving the mechanical stability of the fibers using ZnO NP prevented the sudden uncontrolled release of the drug seen in previous studies (19,20).

The major advantage of this novel use of diffusion to control the drug delivery rate is its flexibility for using any type of drug from antibiotics, to growth factors, to cancer drugs. These drugs could be produced in the form of nanoparticles or could be loaded on the surface of carrier

nanoparticles. Moreover, the presented drug delivery method described in this study could be applied for delivery of bioactive agents, such as bacteriophages, since the agent is loaded inside the fiber core and is preserved from the organic solvents used in the shell or from the harsh conditions of electrospinning. Another possible application of this delivery method, is simultaneous delivery of several therapeutic agents and individual control of their delivery rates via modification of the size of the nanoparticles.

References

1. Agarwal S, Wendorff JH, Greiner A. Use of electrospinning technique for biomedical applications. Vol. 49, Polymer. 2008. p. 5603–21.

2. Abrigo M, McArthur SL, Kingshott P. Electrospun Nanofibers as Dressings for Chronic Wound Care: Advances, Challenges, and Future Prospects. Macromol Biosci. 2014 Jun 1;14(6):772–92.

3. Noruzi M. Electrospun nanofibres in agriculture and the food industry: a review. Vol. 96, Journal of the science of food and agriculture. John Wiley & Sons, Ltd; 2016. p. 4663–78.

4. Lannutti J, Reneker D, Ma T, Tomasko D, Farson D. Electrospinning for tissue engineering scaffolds. Mater Sci Eng C. 2007 Apr 1;27(3):504–9.

5. Persano L, Camposeo A, Pisignano D. Active polymer nanofibers for photonics, electronics, energy generation and micromechanics. Vol. 43, Progress in Polymer Science. Elsevier Ltd; 2015. p. 48–95.

6. Sridhar R, Lakshminarayanan R, Madhaiyan K, Barathi VA, Limh KHC, Ramakrishna S. Electrosprayed nanoparticles and electrospun nanofibers based on natural materials: Applications

in tissue regeneration, drug delivery and pharmaceuticals. Vol. 44, Chemical Society Reviews. Royal Society of Chemistry; 2015. p. 790–814.

7. Zamani M, Prabhakaran MP, Ramakrishna S. Advances in drug delivery via electrospun and electrosprayed nanomaterials. Vol. 8, International Journal of Nanomedicine. 2013. p. 2997–3017.

8. Yarin AL. Coaxial electrospinning and emulsion electrospinning of core-shell fibers. Vol. 22, Polymers for Advanced Technologies. John Wiley & Sons, Ltd; 2011. p. 310–7.

9. Jiang H, Hu Y, Zhao P, Li Y, Zhu K. Modulation of protein release from biodegradable core-shell structured fibers prepared by coaxial electrospinning. J Biomed Mater Res - Part B Appl Biomater. 2006 Oct;79(1):50–7.

10. Zhang YZ, Wang X, Feng Y, Li J, Lim CT, Ramakrishna S. Coaxial electrospinning of (fluorescein isothiocyanate-conjugated bovine serum albumin)-encapsulated poly(ε-caprolactone) nanofibers for sustained release. Biomacromolecules. 2006;7(4):1049–57.

11. Liao IC, Chew SY, Leong KW. Aligned core-shell nanofibers delivering bioactive proteins. Nanomedicine. 2006;1(4):465–71.

12. Huang ZM, He CL, Yang A, Zhang Y, Han XJ, Yin J, et al. Encapsulating drugs in biodegradable ultrafine fibers through co-axial electrospinning. J Biomed Mater Res - Part A. 2006 Apr 1;77(1):169–79.

13. Jiang H, Wang L, Zhu K. Coaxial electrospinning for encapsulation and controlled release of fragile water-soluble bioactive agents. J Control Release. 2014 Nov 10;193:296–303.

14. Khansari S, Duzyer S, Sinha-Ray S, Hockenberger A, Yarin AL, Pourdeyhimi B. Two-Stage Desorption-Controlled Release of Fluorescent Dye and Vitamin from Solution-Blown and Electrospun Nanofiber Mats Containing Porogens. 2013;

15. Abdullah MF, Nuge T, Andriyana A, Ang BC, Muhamad F. Core-Shell fibers: Design, roles, and controllable release strategies in tissue engineering and drug delivery. Vol. 11, Polymers. MDPI AG; 2019. p. 2008.

16. Li W, Yu Q, Yao H, Zhu Y, Topham PD, Yue K, et al. Superhydrophobic hierarchical fiber/bead composite membranes for efficient treatment of burns. Acta Biomater. 2019 Jul 1;92:60–70.

17. Sebe I, Szabó P, Kállai-Szabó B, Zelkó R. Incorporating small molecules or biologics into nanofibers for optimized drug release: A review. Vol. 494, International Journal of Pharmaceutics. Elsevier; 2015. p. 516–30.

18. Buschle-Diller Jared Cooper AE Zhiwei Xie AE Ye Wu AE James Waldrup AE Xuehong Ren GA. Release of antibiotics from electrospun bicomponent fibers. 2007;

19. Andriolo JM, Sutton NJ, Murphy JP, Huston LG, Kooistra-Manning EA, West RF, et al. Electrospun Fibers for Controlled Release of Nanoparticle-Assisted Phage Therapy Treatment of Topical Wounds. In: MRS Advances. Materials Research Society; 2018. p. 3011–7.

20. Klein S, Kuhn J, Avrahami R, Tarre S, Beliavski M, Green M, et al. Encapsulation of bacterial cells in electrospun microtubes. Biomacromolecules. 2009 Jul 13;10(7):1751–6.

21. Fazley Elahi M, Lu W, Guoping G, Khan F. Core-shell Fibers for Biomedical Applications-A Review. 2013;

22. Augustine R, Dominic EA, Reju I, Kaimal B, Kalarikkal N, Thomas S. Investigation of angiogenesis and its mechanism using zinc oxide nanoparticle-loaded electrospun tissue engineering scaffolds. RSC Adv. 2014 Sep 26;4(93):51528–36.

23. Augustine R, Dominic EA, Reju I, Kaimal B, Kalarikkal N, Thomas S. Electrospun polycaprolactone membranes incorporated with ZnO nanoparticles as skin substitutes with enhanced fibroblast proliferation and wound healing. RSC Adv. 2014 Jun 9;4(47):24777–85.

24. Gao Y, Han Y, Cui M, Tey HL, Wang L, Xu C. ZnO nanoparticles as an antimicrobial tissue adhesive for skin wound closure. J Mater Chem B. 2017 Jun 14;5(23):4535–41.

25. Zhang S, Tang Y, Vlahovic B. A Review on Preparation and Applications of Silver-Containing Nanofibers. Vol. 11, Nanoscale Research Letters. Springer New York LLC; 2016. p. 1–8.

26. De Faria AF, Perreault F, Shaulsky E, Arias Chavez LH, Elimelech M. Antimicrobial Electrospun Biopolymer Nanofiber Mats Functionalized with Graphene Oxide-Silver Nanocomposites. ACS Appl Mater Interfaces. 2015;7(23):12751–9.

27. Tijing LD, Amarjargal A, Jiang Z, Ruelo MTG, Park CH, Pant HR, et al. Antibacterial tourmaline nanoparticles/polyurethane hybrid mat decorated with silver nanoparticles prepared by electrospinning and UV photoreduction. Curr Appl Phys. 2013 Jan 1;13(1):205–10.

28. Wang B, Xu C, Xu F, Lu T. Electrospinning of poly(ethylene-co-vinyl alcohol) nanofibres encapsulated with Ag nanoparticles for skin wound healing. J Nanomater. 2011 Jan 23;2011:1–7.

29. Wang X, Cheng F, Gao J, Wang L. Antibacterial wound dressing from chitosan/polyethylene oxide nanofibers mats embedded with silver nanoparticles. J Biomater Appl. 2015 Mar 2;29(8):1086–95.

30. Kohsari I, Shariatinia Z, Pourmortazavi SM. Antibacterial electrospun chitosan-polyethylene oxide nanocomposite mats containing ZIF-8 nanoparticles. Int J Biol Macromol. 2016 Apr 20;91:778–88.

31. Tian L, Wang P, Zhao Z, Ji J. Antimicrobial activity of electrospun poly(butylenes succinate) fiber mats containing PVP-capped silver nanoparticles. Appl Biochem Biotechnol. 2013 Dec 7;171(7):1890–9.

32. Song J, Remmers SJA, Shao J, Kolwijck E, Walboomers XF, Jansen JA, et al. Antibacterial effects of electrospun chitosan/poly(ethylene oxide) nanofibrous membranes loaded with chlorhexidine and silver. Nanomedicine Nanotechnology, Biol Med. 2016 Jul 1;12(5):1357–64.

33. Quirós J, Borges JP, Boltes K, Rodea-Palomares I, Rosal R. Antimicrobial electrospun silver-, copper- and zinc-doped polyvinylpyrrolidone nanofibers. J Hazard Mater. 2015 Dec 15;299:298–305.

34. Xu X, Zhou M. Antimicrobial gelatin nanofibers containing silver nanoparticles. Fibers Polym. 2008 Dec 13;9(6):685–90.

35. Xia T, Hamilton RF, Bonner JC, Crandall ED, Elder A, Fazlollahi F, et al. Interlaboratory Evaluation of in Vitro Cytotoxicity and Inflammatory Responses to Engineered Nanomaterials: The NIEHS Nano GO Consortium. Environ Health Perspect. 2013 Jun;121(6):683–90.

36. Hamilton R, Buckingham S, Holian A. The Effect of Size on Ag Nanosphere Toxicity in Macrophage Cell Models and Lung Epithelial Cell Lines Is Dependent on Particle Dissolution. Int J Mol Sci. 2014 Apr 22;15(4):6815–30.

37. Zhang YZ, Feng Y, Huang ZM, Ramakrishna S, Lim CT. Fabrication of porous electrospun nanofibres. Nanotechnology. 2006;17(3):901–8.

38. Lu Y, Jiang H, Tu K, Wang L. Mild immobilization of diverse macromolecular bioactive agents onto multifunctional fibrous membranes prepared by coaxial electrospinning. Acta Biomater. 2009 Jun;5(5):1562–74.

39. Chakraborty S, Liao IC, Adler A, Leong KW. Electrohydrodynamics: A facile technique to fabricate drug delivery systems. Vol. 61, Advanced Drug Delivery Reviews. 2009. p. 1043–54.

40. Fashandi H, Karimi M. Characterization of porosity of polystyrene fibers electrospun at humid atmosphere. Thermochim Acta. 2012 Nov 10;547:38–46.

41. Bognitzki M, Frese T, Steinhart M, Greiner A, Wendorff JH, Schaper A, et al. Preparation of fibers with nanoscaled morphologies: electrospinning of polymer blends. Polym Eng Sci. 2001 Jun 1;41(6):982–9.

42. Corrigan OI, Murphy CA, Timoney RP. Dissolution properties of polyethylene glycols and polyethylene glycol-drug systems. Int J Pharm. 1979 Nov;4(1):67–74.

43. Huang X, Brazel CS. On the importance and mechanisms of burst release in matrix-controlled drug delivery systems. Vol. 73, Journal of Controlled Release. Elsevier; 2001. p. 121–36.

44. Wang X, Cheng F, Gao J, Wang L. Antibacterial wound dressing from chitosan/polyethylene oxide nanofibers mats embedded with silver nanoparticles. J Biomater Appl. 2015 Mar 2;29(8):1086–95.

45. Katayama K, Nomura H, Ogata H, Eitoku T. Diffusion coefficients for nanoparticles under flow and stop-flow conditions. Phys Chem Chem Phys. 2009 Nov 4;11(44):10494–9.

46. Rudyak VY. Diffusion of nanoparticles in gases and liquids. In: Handbook of Nanoparticles. 2015. p. 1193–218.

47. Wang H, Burgess RM, Cantwell MG, Portis LM, Perron MM, Wu F, et al. Stability and aggregation of silver and titanium dioxide nanoparticles in seawater: Role of salinity and dissolved organic carbon. Environ Toxicol Chem. 2014 May;33(5):1023–9.

48. Yarin AL. Coaxial electrospinning and emulsion electrospinning of core-shell fibers. Polym Adv Technol. 2011 Mar;22(3):310–7.

49. Augustine R, Malik HN, Singhal DK, Mukherjee A, Malakar D, Kalarikkal N, et al. Electrospun polycaprolactone/ZnO nanocomposite membranes as biomaterials with antibacterial and cell adhesion properties. J Polym Res. 2014 Mar 13;21(3):347.

50. Augustine R, Kalarikkal N, Thomas S. Effect of zinc oxide nanoparticles on the in vitro degradation of electrospun polycaprolactone membranes in simulated body fluid. Int J Polym Mater Polym Biomater. 2016 Jan 2;65(1):28–37.

51. Luković Golić D, Branković G, Počuča Nešić M, Vojisavljević K, Rečnik A, Daneu N, et al. Structural characterization of self-assembled ZnO nanoparticles obtained by the sol-gel method from Zn(CH3COO)22H2O. Nanotechnology. 2011 Sep 30;22(39):395603.

52. Zhou H, Green TB, Joo YL. The thermal effects on electrospinning of polylactic acid melts. Polymer (Guildf). 2006 Oct 4;47(21):7497–505.

53. Wright JB, Lam K, Burrell RE. Wound management in an era of increasing bacterial antibiotic resistance: A role for topical silver treatment. Am J Infect Control. 1998 Dec 1;26(6):572–7.

54. Zhou Y, Hosur M, Jeelani S, Mallick PK. Fabrication and characterization of carbon fiber reinforced clay/epoxy composite. J Mater Sci. 2012 Jun;47(12):5002–12.

55. Sombatsompop N, Chaochanchaikul K. Effect of moisture content on mechanical properties, thermal and structural stability and extrudate texture of poly(vinyl chloride)/wood sawdust composites. Polym Int. 2004 Sep 1;53(9):1210–8.

56. Felice B, Sánchez MA, Socci MC, Sappia LD, Gómez MI, Cruz MK, et al. Controlled degradability of PCL-ZnO nanofibrous scaffolds for bone tissue engineering and their antibacterial activity. Mater Sci Eng C. 2018 Dec 1;93:724–38.

57. Münchow EA, Albuquerque MTP, Zero B, Kamocki K, Piva E, Gregory RL, et al. Development and characterization of novel ZnO-loaded electrospun membranes for periodontal regeneration. Dent Mater. 2015 Sep 1;31(9):1038–51.

58. Duling RR, Dupaix RB, Katsube N, Lannutti J. Mechanical characterization of electrospun polycaprolactone (PCL): A potential scaffold for tissue engineering. J Biomech Eng. 2008 Feb 5;130(1):011006.

59. Sabo R, Jin L, Stark N, Ibach RE. Effect of environmental conditions on the mechanical properties and fungal degradation of polycaprolactone/ microcrystalline cellulose/wood flour composites. BioResources. 2013 May 9;8(3):3322–35.

Supplementary data of chapter 2

Table 1. The Holm-Sidak's multiple comparisons test results for the percent cumulative release of Ag from fiber meshes reported in Figure 2.8B. Asterisks indicate significant difference ****$p < 0.0001$, ***$p < 0.0002$, **$p < 0.0021$, *$p < 0.0332$, $^{ns}P > 0.1234$.

	F-Ag20 vs. F-AgMix	F-Ag20 vs. F-Ag110	F-AgMix vs. F-Ag110
1h	ns	ns	*
2h	ns	ns	**
4h	*	ns	***
8h	***	ns	****
24h	****	ns	****
72h	****	ns	****
168h	****	***	****
336h	****	****	****

Table 2. The Holm-Sidak's multiple comparisons test results for the percent cumulative release of Zn from fiber meshes reported in Figure 2.9. Asterisks indicate significant difference ****$p < 0.0001$, ***$p < 0.0002$, **$p < 0.0021$, *$p < 0.0332$, $^{ns}P > 0.1234$.

	F-Ag20 vs. F-AgMix	F-Ag20 vs. F-Ag110	F-AgMix vs. F-Ag110
1h	ns	ns	ns
2h	ns	ns	ns
4h	ns	ns	ns
8h	ns	ns	ns
24h	ns	ns	ns
72h	ns	ns	ns
168h	ns	ns	**
336h	ns	ns	****

Table 3. The Holm-Sidak's multiple comparisons test results for the measured tensile properties (elongation at break, ultimate tensile strength, and Young's modulus) of non-, one-, and two-week immersed fiber mesh F-Ag20 reported in Table 2.3. Asterisks indicate significant difference ****$p < 0.0001$, ***$p < 0.0002$, **$p < 0.0021$, *$p < 0.0332$, $^{ns}P > 0.1234$.

	Non-immersed vs. one-week immersed	Non-immersed vs. two-week immersed	one-week immersed vs. two-week immersed
Elongation at break	**	**	ns
Ultimate tensile strength	***	ns	**
Young's modulus	ns	*	*

Chapter 3: Electrospun fibers loaded with ball-milled microgel particles for smart delivery applications

Contributions

Zahra Mahdieh, University of Montana: Primary author responsible for development of project and design of experiments. Performed electrospinning processes and sample preparations, scanning electron microscopy, confocal laser scanning microscopy, in vitro release studies, weight loss studies, syntheses of hydrogels, ball milling of hydrogels, differential scanning calorimetry, dynamic light scattering analyses, tensile testing, and statistical analyses.

Andrij Holian, University of Montana: Supervised project development and experimental design. Reviewed final paper submission.

Gretchen McCaffrey, University of Montana: Provided editorial guidance for preparation of paper.

Somenath Mitra, New Jersey Institute of Technology: Provided resource support for coupled plasma mass spectrometry.

Larisa Krishtopa, New Jersey Institute of Technology: Performed coupled plasma mass spectrometry.

Jim Driver, University of Montana: Provided training and resource support for scanning electron microscopy. Performed transmission electron microscopy.

Lou Harriette, University of Montana: Provided training for confocal laser scanning microscopy.

Monica Serban, University of Montana: Provided training and resources for tensile testing.

Chris Palmer, University of Montana: Provided resource support for syntheses of hydrogels.

Hamilton Ray, University of Montana: Provided training for statistical analyses.

Kevin Trout, University of Montana: Constructed electrospinning hardware and provided training for electrospinning.

Robert Walker, Montana State University: Provided resource support for field emission scanning electron microscopy.

Elif Roehm, Montana State University: Performed field emission scanning electron microscopy.

Abstract

Stimuli-responsive electrospun fibers loaded with therapeutic agents for smart delivery triggered by stimuli such as temperature or pH are attractive options for wound dressing, cancer treatment, and tissue engineering applications. However, development of such fibers requires the use of complex chemical processes that can induce toxicity, reduce fiber quality, or prohibit fiber electrospinnablity. To address these challenges, core-shell structured fibers capable of temperature-controlled delivery of nanoparticles were developed. The fiber core contained an aqueous suspension of poly(n-isopropylacrylamide) (PNIPAM) microgel particles and silver nanoparticles (Ag NP, as a model antibacterial drug). A novel use of ball-milling was applied to produce microgel particles with an average hydrodynamic diameter of 511 ± 100 nm. The ball-milling technique was developed to avoid the current complex chemical processes for syntheses of microgels, and to address the need for high-yield techniques in industrial manufacturing. The results show that the thermoresponsive properties of the PNIPAM hydrogel particles were preserved during the ball-milling process. The fiber shell formed a strong and ductile structure matrix, regulated the nanoparticles release pathway (through stable and defined pores formed via selective dissolution of porogen), in addition to serving as a barrier to prevent direct contact of the microgel particles with tissues. This core-shell fiber design allows for the future application of various therapeutic agents, including fragile and bioactive agents, and microgel particles with special properties.

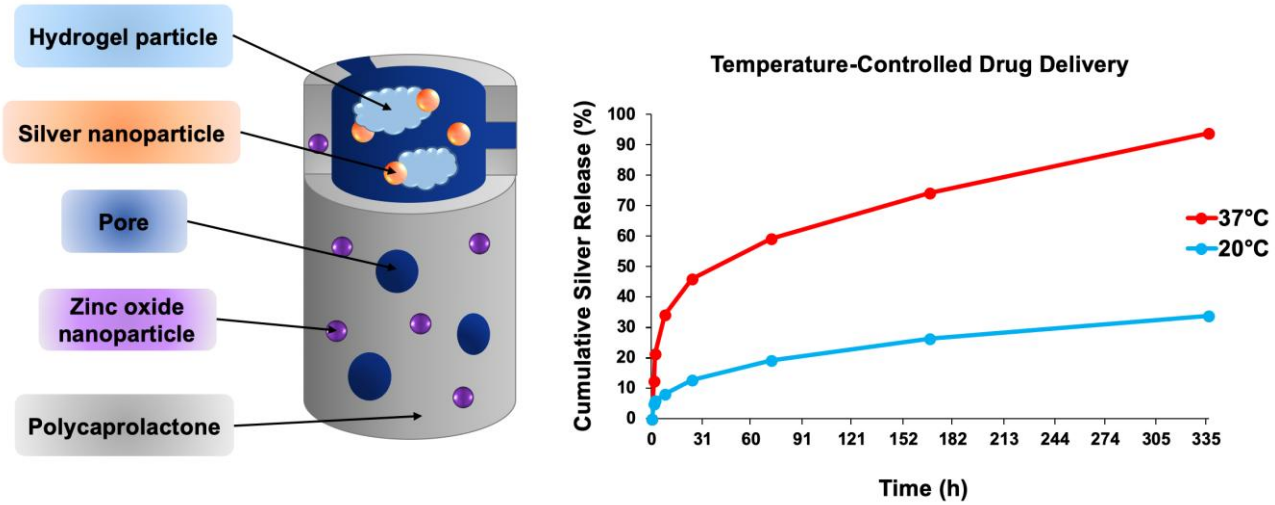

Temperature controlled release of silver nanoparticles from core-shell structured electrospun fibers via application of poly(n-isopropylacrylamide) microgel particles inside the core

Introduction

Stimuli-responsive polymers are called “smart” polymers for the ability to sense and respond to environmental parameters such as temperature, light, pH, and electromagnetic force (1,2). In particular, poly(n-isopropylacrylamide) (PNIPAM) is a thermoresponsive polymer with a reproducible lower critical solution temperature behavior. PNIPAM has been extensively studied for development of various drug delivery systems owing to its transition temperature being close to the human body temperature (between 30 to 35, depending on the solvents and chain modifications) (3,4). Therapeutic agents can be incorporated with the polymer in the swollen hydrophilic state below the transition temperature and released in the collapsed hydrophobic state on demand when the ambient temperature increases above the transition temperature (5,6). Therefore, to improve the treatment efficacy, various PNIPAM drug delivery systems in the form of fibers, microgels, and films are developed (7–10).

Electrospun fibers of PNIPAM are highly attractive for biomedical applications such as wound dressing, tissue engineering and cancer treatment (10–12). However, several challenges have hindered their use in such applications. The primary shortcoming of PNIPAM electrospun fibers is the lack of mechanical stability caused by dissolution of PNIPAM below the transition temperature and collapse of the polymer network above the transition temperature (13,14). Therefore, the low mechanical stability of PNIPAM fibers can result in a burst release of loaded drugs, possible toxic effects of fast released polymer or loaded drug, and failure to deliver required mechanical support (15–19). Cross-linking of the PNIPAM polymer network could stabilize the PNIPAM fibers (20–23). However, crosslinking must be performed after the electrospinning process because it is not possible to inject a crosslinked polymer, which is solidified, through the spinneret. While post-crosslinking is effective to improve the mechanical

stability of the fibers, it precludes the possibility of loading fragile or bioactive therapeutic agents into the fibers because of the harsh conditions and organic solvents required for crosslinking (24–26).

Smart microgel particles (including PNIPAM microgels) are crosslinked polymer particles that have a stimuli-responsive property (27). Due to the smaller dimension, the swelling/deswelling response of microgel particles is much faster than macroscopic hydrogels (28). Accordingly, microgel particles have prompted great interest in a variety of applications such as biomedical applications, filtration, and nanoreactors (29–32). In particular, biomedical and cosmetic applications require mechanical and chemical versatility of microgels, along with biocompatibility. Therefore, there is a great need for novel design strategies that can simultaneously meet the biological and physical attributes of microgel particles (33–35). Importantly, the increasing industrial applications of microgel particles, such as the agriculture and food industry, demand large scale manufacturing techniques (36–38).

In the current study, electrospun fibers with a core-shell structure were designed to simultaneously address challenges of mechanical stability, burst release, possible toxicity, and capable of loading bioactive or fragile therapeutic agents. Unlike other fiber designs where the whole fiber or fiber shell were electrospun from PNIPAM, we used PNIPAM microgel particles and loaded them inside the fiber core. The fiber core contained a suspension of PNIPAM microgel particles and silver nanoparticles (Ag NP), which were used as a model antibacterial drug. We also developed a novel use of ball-milling as a simple, non-toxic, and high-yield technique for producing microgel particles. The use of ball-milling was developed to avoid the current chemical complexities for synthesizing microgel particles, which usually require the use of toxic chemicals (24).

Materials and methods

N-isopropylacrylamide (NIPAM, ≥99%), potassium persulfate (ACS reagent, ≥99.0%), Tetramethylenediamine (TEMED, 99%), Poly(ethylene glycol) (PEG, BioUltra, Mw = 3,350 g/mol), polycaprolactone (PCL, MW = 45,000 g/mol), Chloroform (biotechnology grade, ≥99.8%, 0.5-1.0% ethanol as stabilizer), N,N-Dimethylformamide (DMF, ReagentPlus, ≥99%), and fluorescein isothiocyanate-diethylaminoethyl-dextran (FITC–DEAE–Dextran, Mw = 70,000 g/mol) were purchased from Sigma-Aldrich, USA. Laponite XLG was provided by BYK Additives Inc., Gonzales, TX, USA. Citrate coated silver nanoparticles (Ag NP, 20 nm diameter, 1 mg/mL) stabilized in 2 mM sodium citrate aqueous solution were obtained from NanoComposix (Biopure^{TM}, San Diego, CA, USA). Zinc oxide nanoparticles were obtained from Meliorum Technologies, Inc. (ZnO NP, 20 nm diameter, Rochester, NY, USA). Characterization information of ZnO NP and Ag NP is available in our previous studies (39,40). Ultrapure Mili-Q water, obtained from a Milli-Q water purifier (QGARD00D2, Millipore, USA), was used throughout this study.

Preparation of the PNIPAM microgel particles (microgel)

PNIPAM hydrogel was synthesized via an *in situ* free radical polymerization method developed by Haraguchi, k. et al (41). Laponite XLG clay (1 g) and n-isopropylacrylamide (3 g, NIPAM) were added into water (28.5 mL) and stirred in a round bottom flask while bubbled with nitrogen gas for three hours at 20°C. Afterward, the temperature of the solution was brought to 0°C using an ice bath, and a solution of the catalyst (TEMED, 24 µL) and initiator (KPS, 0.03 g) in water (1.5 mL) was injected into it. The ice bath was then allowed to reach room temperature (20°C) and free radical polymerization was allowed to proceed for 20 hours. The positive pressure of nitrogen was maintained inside the reactor during the whole polymerization

process to avoid oxygen. The prepared hydrogel was then cut into small pieces (~ 1 cm^3) and soaked in water for 48 hours (water was changed several times) to purify the hydrogel. After purification, the hydrogel pieces were dried at 40°C for 48 hours. Afterward, 3.6 g of the dried hydrogel pieces were put in a ball-mill vial and ball-milled with 4 balls for 80 minutes. Ball-milling was performed using a zirconia ceramic grinding vial set (6.35 cm × 6.8 cm, 8005), zirconia ceramic balls (12.7 mm diameter, 8005A), and a mill (8000D DUAL MIXER/MILL®) obtained from SPEX® SamplePrep, Metuchen, NJ, USA.

Preparation of PNIPAM microgel particles with Ag NP

To make the suspension of PNIPAM microgel particles (3 Wt%) and Ag NP (0.01 Wt%), the ground microgel (0.3 g) was added into water (9 mL) and stirred for 4 hours. The suspension was then pushed through a 25-gauge needle to break up any agglomerates of microgel particles. Afterward, an aqueous suspension of Ag NP (1 mL) was added to the microgel particles suspension, and the final suspension was stirred overnight before the electrospinning process.

Electrospinning of core-shell fibers

The core-shell fibers were fabricated using a coaxial electrospinning instrument designed and constructed in our laboratory. The electrospinning instrument was housed inside an electrically-insulated plastic case that was inside a laboratory safety hood (ambient humidity 10% and room temperature 20°C). The electrospinning arrangement was horizontal and the spinneret to collector distance was 14 cm. A prebuilt blunt coaxial spinneret (100-10-COAXIAL-2016, ramé-hart instrument Co.) with a 16-gauge outer needle and a 20-gauge inner needle was used. The collector was a rotating drum (226 rpm, 5.08 cm diameter) which was covered with a piece of aluminum foil. The spinneret was connected to DC power (17 kV) and the collector was grounded. An optimum fiber structure was achieved in this study using a shell

composition of 14 Wt% PCL, 6.5 Wt% PEG, and 1.6 Wt% of ZnO NP in a mixture of chloroform and DMF (with a ratio of 17:10), and core composition of 3 Wt% PNIPAM microgel particles and 0.01 Wt% of Ag NP in water. The core and shell fluid feeding rates were 0.4 and 1 mL/h, respectively. Fiber meshes were obtained during one hour of electrospinning, then left inside the hood to dry overnight. The electrospun fiber mesh was designated F-AgHG representing the Ag NP and PNIPAM microgel particles inside the fiber core.

Dynamic Light Scattering (DLS)

DLS measurements were performed to evaluate the swelling/shrinking behavior and particle size changes of the PNIPAM microgel particles in water using a Zetasizer Nano ZS (Malvern Instruments Ltd., ZEN3600, UK). The hydrodynamic diameter of microgel particles was measured over the temperature range of 20-50°C with temperature intervals of 1°C (three measurements were performed at each temperature interval). The concentration of the microgel particles in water was adjusted to prevent particle-particle interaction due to the agglomeration, and obtain count rate (photons detected per second) higher than 10 KCPS (kilo-counts per second) (42,43).

Differential Scanning Calorimetry (DSC)

DSC measurements were performed to determine the thermoresponsive phase transition of the PNIPAM microgel using a TA differential scanning calorimeter (Q20 V24.11 build 124, USA). After synthesizing the PNIPAM hydrogel and purifying it by soaking in water, a small piece (6.21 mg) of the PNIPAM hydrogel was cut and put in a Tzero aluminum hermetic pan and scanned over a temperature range of 25-50°C with the heating rate of 3°C/min, under nitrogen atmosphere. Microgel particles obtained by ball-milling were also tested; a 3 Wt% suspension of PNIPAM microgel particles (6.24 mg, preparation explained in part 2.3) was pipetted into a

Tzero aluminum hermetic pan and was scanned under a similar condition. The 3 Wt% concentration was chosen because it is the concentration of the PNIPAM microgel particles in the fiber core.

Release of nanoparticles

Rectangular samples of 15 cm × 3 cm were cut from the center of electrospun fiber meshes. To obtain intact sample pieces, fiber meshes were dipped in water for a few seconds and then quickly detached from the aluminum foil on which they were electrospun. Samples were placed into 50 mL conical centrifuge tubes filled with 20 mL of water. The tubes were placed on shakers (200 rpm, 0.3-cm orbit motion, Thermo Labline 4625 Titer Shaker, USA) on a lab bench (room temperature of 20°C) or inside an incubator (37°C). At predetermined time intervals, samples were gently taken out of the tubes and transferred into new tubes filled with 20 mL fresh water and put back on the shakers. The time intervals of 1 h, 2 h, 4 h, 8 h, 24 h, 3 days, 7 days, and 14 days were selected to determine the short and long-term use of fiber meshes. Water was chosen as the immersion media to consider possible uses of the fibers for various applications ranging from biomedical to filters and sensors (10,11). The average of three samples was used for each data point (error bars represent the standard deviation, SD, for n=3). The amounts of Ag and Zn released in the supernatants were measured using an inductively coupled plasma mass spectrometer (ICP-MS, Agilent 7900, CA, USA). The released percentages of Ag at each time interval (Ag_r) were calculated as follows:

$$\% Ag_r = \frac{Ag_s}{Ag_t \times \frac{A_s}{A_t}} \times 100 \quad (1)$$

Where Ag_s is the measured Ag (g) by ICP-MS in 20 mL supernatant at each time internal; Ag_t is the primary amount of Ag (g) injected into the inner needle during 1 h of

electrospinning; A_s is the cut sample area (15 cm × 3 cm); and A_t is the primary area of the electrospun fiber mesh.

The released percentages of Zn at each time interval (Zn_r) were calculated as follows:

$$\% Zn_r = \frac{Zn_s}{Zn_t} \times 100 \quad (2)$$

$$Zn_t = M_s \times \frac{M_{ZnO}}{M_{ZnO}+M_{PCL}+M_{PEG}+M_{core}} \quad (3)$$

Zn_s is the measured Zn (g) by ICP-MS in 20 mL supernatants at each time interval; Zn_t is the total Zn (g) in the primary electrospun fiber mesh. Zn_t was calculated using formula 3 where, M_s is the mass (g) of the sample before immersion; M_{ZnO}, M_{PCL}, and M_{PEG} are the masses of ZnO, PCL, and PEG used for making the fiber mesh, respectively; and M_{core} is the mass of the core solution injected during 1 h of electrospinning. A more detailed explanation of formulas 1-3 can be found in our previous study (44).

Weight loss of fiber meshes

The F-AgHG samples of the release study were weighed before immersion and after one- and two-week immersion at 20°C and 37°C to calculate their weight loss. The percent of sample weight loss was calculated as follows:

$$\%Weight\ Loss = \frac{M_0 - M_i}{M_0} \times 100 \quad (4)$$

Where M_0 is the sample weight before immersion and M_i is the sample weight after one- and two- week immersion at 20°C or 37°C.

Tensile test

Samples were prepared by cutting the fiber meshes into strips of 1 cm × 7 cm. Then fiber samples were quickly detached from the aluminum foil in water to avoid damage. Samples were then immersed in 15 mL water for one and two weeks on shakers (200 rpm, 0.12-inch orbit motion, Thermo Labline 4625 Titer Shaker) placed at 20°C and 37°C. The no immersion group was air-dried after detachment from the aluminum foil. All samples were kept for four days at 20°C and 10% humidity (laboratory ambient condition) before the tensile test. Tensile tests were performed at strain rate of 10 mm/min and load cell of 10 N using a Discovery HR2 hybrid rheometer (TA Instruments, New Castle, DE, USA). The gauge length was set at 30 mm and the gripping distance was 10 mm. The thickness of fiber meshes was measured with FESEM imaging. Four replicates were performed for each measurement.

PNIPAM microgel particles release

Similar to the release study, fiber meshes cut into rectangular samples of 15 cm × 3 cm were immersed in 20 mL water with shaking at 20°C and 37°C for two weeks. After two weeks of immersion, fiber meshes were removed and water samples were collected. Water samples were centrifuged at 9,000 × g for 3 minutes at 20°C to pellet any fiber mesh pieces that might have degraded during the immersion. We confirmed that using this centrifugation procedure did not pellet any detectable PNIPAM microgel particles. As a control, a suspension of the PNIPAM microgel particles in water with a known concentration was centrifuged and placed at 50°C to visualize the PNIPAM microgel particles (which are opaque above the transition temperature).

To increase the detection limit of the PNIPAM microgel particles in water samples, the concentration was increased 3-fold by centrifugation at 15,000 × g for 10 minutes at 40°C to

pellet PNIPAM microgel particles. Then, 2/3 of the water was pipetted out to increase the concentration. The concentrated water samples were then cooled to 20°C and the PNIPAM microgel particles were resuspended by vortexing. Then, 200 µL of the water samples were pipetted into 96 microwell plates, and measuring the optical density at 450 nm (OD_{450}, SpectraMax M4 multi-mode microplate reader, Molecular Devices, USA) was used to determine the amount of PNIPAM microgel particles released after two-week immersion. The OD_{450} was measured at 50°C because the PNIPAM microgel particles are opaque and absorb light above the transition temperature, thus they can be detected at lower concentrations. The detection limit of the PNIPAM microgel particles in aqueous suspension was determined by making a concentration series of the suspensions and measuring their OD_{450} at 50°C.

Scanning electron microscopy and fluorescent imaging

Scanning electron microscope (SEM, Hitachi S-4700) imaging was used to assess the morphology and the size of ball-milled microgel particles. A small amount of the ground PNIPAM microgel particles was placed on a carbon taped stage and then gold-coated for imaging. Field emission scanning electron microscope (FESEM, Zeiss SUPRA 55VP) imaging was used to determine the morphology of electrospun fiber meshes before and after immersion (one and two weeks). Fiber meshes were gold-coated before imaging. At least 200 points of FESEM images were measured using image analyzer software (ImageJ, National Institutes of Health, USA) to calculate the average fiber diameter and pore size.

Confocal imaging (Confocal Laser Scanning Microscope, CLS, Zeiss LSM 880) was used to assess the core-shell structure of the fibers. Fluorescent dextran (FITC_DEAE-Dextran, 0.01%) was added to the core fluid and protected from light to avoid photobleaching. Electrospinning procedure was performed with similar conditions and fibers were collected on a

microscopy cover glass quickly passed in front of the spinneret close to the collector. Fibers without fluorescent dextran were also collected as a control.

Statistical analyses

Statistical analyses were performed using a one- or two-way ANOVA followed by individual comparison of groups using Holm-Sidak's multiple comparisons test (PRISM v.7.0, GraphPad, San Diego, CA, USA). The Holm-Sidak's multiple comparison results are reported at supplementary data of chapter 3. A statistical significance level of 5% ($p < 0.05$) was defined. The minimum number of replicates was three. Values were reported as M ± SD.

Results and discussion

Characterization of the PNIPAM microgel particles

A novel method of producing microgel particles was developed to avoid the current chemical challenges in synthesizing microgel particles for use in electrospun fibers. PNIPAM microgel particles produced via this method were first characterized to make sure that the drying and ball-milling did not interfere with the function of the hydrogel i.e. thermoresponsive behavior, and also that particles have an appropriate size to be loaded inside the fiber core via coaxial electrospinning.

SEM imaging was performed to characterize the general morphology of microgel particles after ball-milling (in the dry state). Figures 3.1A and 3.1B show the microgel particles at two different magnifications. It can be seen in these micrographs that the microgel particles had irregular shapes, which is a common result of the ball-milling process (45). It can be seen in Figure 3.1B (with higher magnification) that small particles had agglomerated into larger particles.

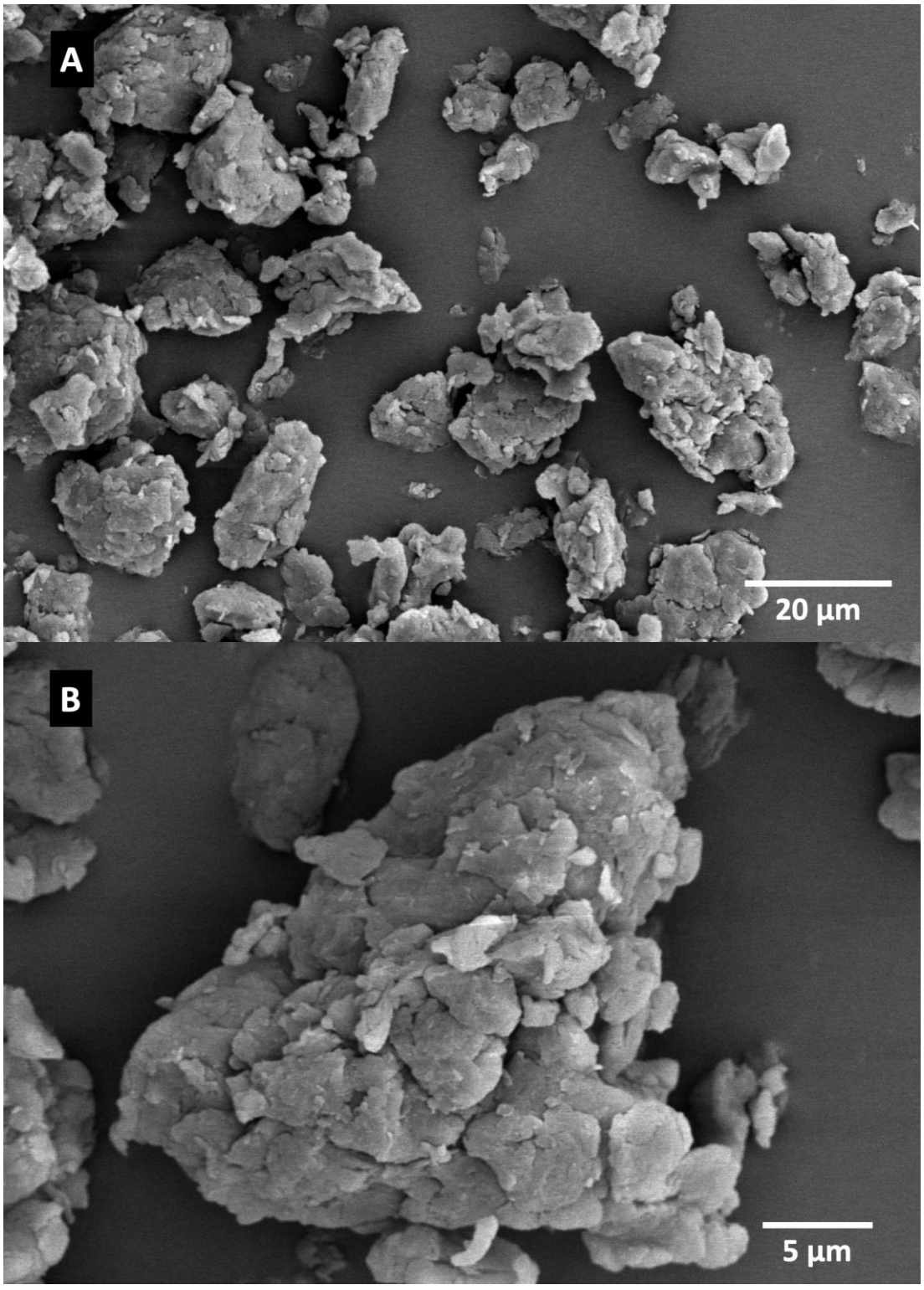

Figure 3.1 SEM micrographs of the ball-milled PNIPAM microgel particles with (A) 996X, 10KV and (B) 3KX, 10KV magnifications.

The hydrodynamic diameter of PNIPAM microgel particles in suspension and changes with temperature were assessed with DLS analysis. The PNIPAM hydrogel produced via the method developed by Haraguchi et al (41) absorbs water (hydrophilic) below the transition temperature (~33°C) and shrinks and expels water (hydrophobic) above the transition temperature (41). Microgels made from PNIPAM hydrogel were evaluated by DLS analysis of the aqueous suspension of PNIPAM microgel particles over the temperature range of 20-50°C with three measurements performed at each temperature interval. Moreover, the validity of hydrodynamic diameter measurements was assessed by assuring that the count rates (photons detected per second) were in the valid range (above 10KCPS, determined by the DLS instrument manufacturers) and had no fluctuations (42,43).

Figure 3.2A shows the measured hydrodynamic diameters (blue line) and the count rates (red line) for the PNIPAM microgel particles at the concentration of 3 Wt%, which is the same concentration used for the core fluid of the electrospinning process. Two regions can be seen in the curves of Figure 3.2A; 20-34°C and 34-50°C. In the region of 20-34°C, the count rates were in the valid range and had no fluctuations, showing a valid hydrodynamic diameter measurement. Hence, the average hydrodynamic diameter of PNIPAM microgel particles was determined to be 511 ± 100 nm in the region of 20-34°C. When the temperature increased above 34°C, the hydrodynamic diameter increased and the measurements at each temperature interval had higher variations. The increase of the hydrodynamic diameter accompanied by the increased fluctuations of the count rate curve in this region (34-50°C) indicated that agglomeration of PNIPAM microgel particles occurred and the measured hydrodynamic diameter was no longer valid due to the particle-particle interactions. The observed behavior is consistent with the lower critical solution temperature behavior of the PNIPAM microgel particles being hydrophilic and

dispersed in between water molecules below the transition temperature, while becoming hydrophobic and agglomerating above the transition temperature. Therefore, to inhibit the effect of the particle-particle interactions in the measurements at 34-50°C, the concentration of PNIPAM microgel particles in water was decreased gradually to find a concentration where the count rate curve was stable and higher than 10KCPS. Figure 3.2B shows the measured hydrodynamic diameters (blue line) and the count rates (red line) for the PNIPAM microgel particles at the concentration of 0.005 Wt%, which was found to be suitable for DLS measurements in the region of 34-50°C. It can be seen in Figure 3.2B that the count rate curve was stable in the region of 34-50°C and the count rates were higher than 10KCPS. Hence, the average hydrodynamic diameter of the PNIPAM microgel particles was determined to be 199 ± 10 nm above the transition temperature. Moreover, it can be seen in Figure 3.2B that the hydrodynamic diameter curve had large fluctuations in the region of 34-50°C, which was due to the low count rate i.e. invalid measurement (42,43).

The detailed DLS analysis of the PNIPAM microgel particle size distribution measured at 25°C and 40°C are shown in Table 3.1. At 25°C, particle size was variable. At 40°C, there was one particle size showing the shrinkage of PNIPAM microgel particles above the transition temperature. These results show that below the transition temperature, the PNIPAM microgel particles take in water and expand to larger diameters and size distribution, while below the transition temperature, the PNIPAM microgel particles expel water and collapse into smaller diameters.

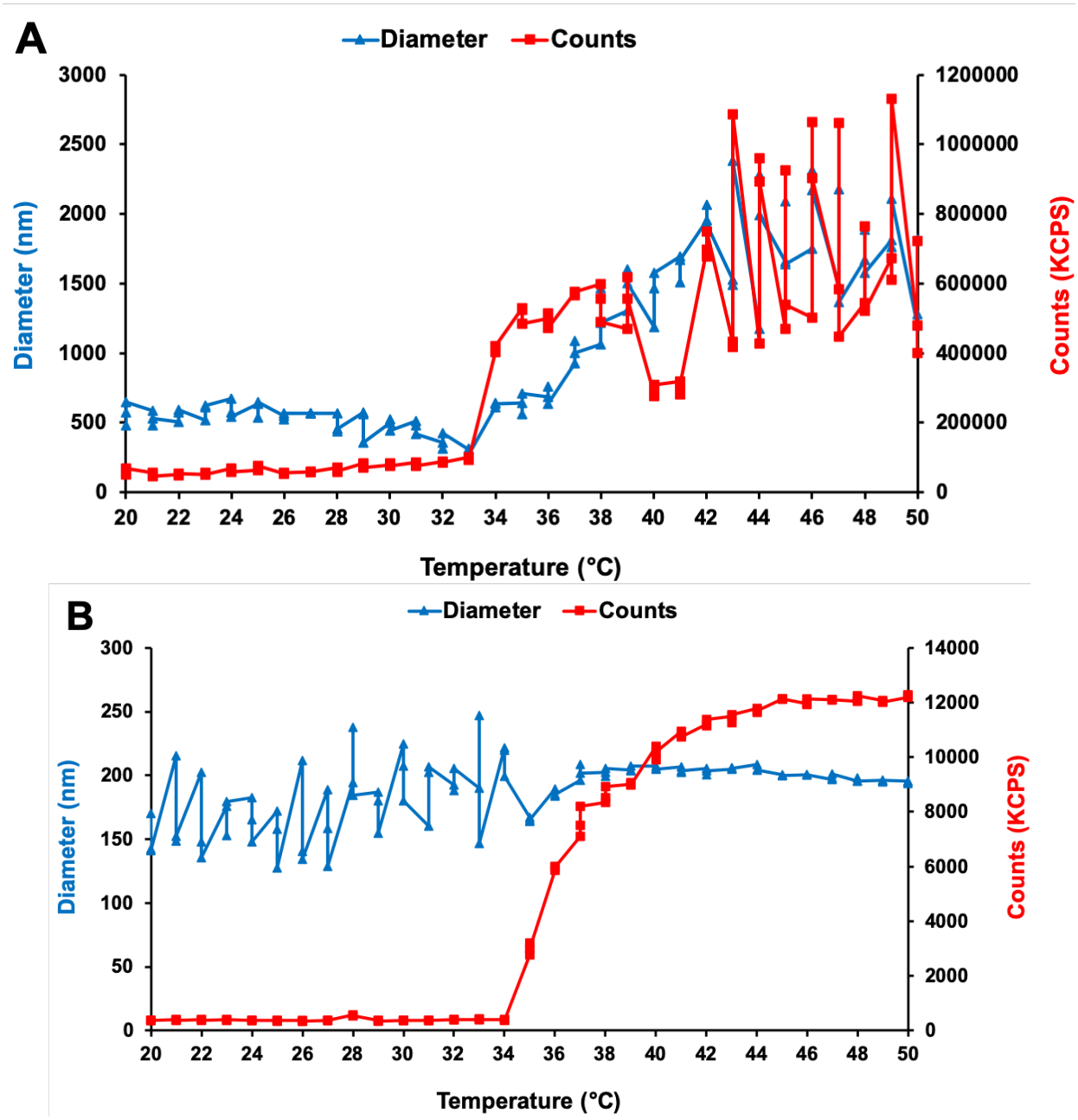

Figure 3.2 The temperature-dependent hydrodynamic diameter (blue line) and the count rate (red line) of PNIPAM microgel particles with the concentration of (A) 3 Wt% and (B) 0.005 Wt%.

Table 3.1 The hydrodynamic diameter distribution of PNIPAM microgel particles measured at 25°C and 40°C.

Temperature: 25 (°C), Count rate: 371 (KCPS), PDI: 0.699			
	Size (nm)	**Intensity (%)**	**SD (nm)**
Peak 1	122	64.1	48.9
Peak 2	1425	21.4	579
Peak 3	4660	8	822
Temperature: 40 (°C), Count rate: 131 (KCPS), PDI: 0.182			
	Size (nm)	**Intensity (%)**	**SD (nm)**
Peak 1	215	100	62.8

The thermoresponsive behavior of PNIPAM hydrogel (before ball-milling) and PNIPAM microgel particles (after drying, ball-milling, and resuspension in water) was characterized using calorimetry. The thermoresponsive transition of PNIPAM hydrogel and the microgel particles are represented by endothermic peaks on DSC thermograms in Figure 3.3. PNIPAM hydrogel had an endothermic peak with onset temperature (T_{onset}) at 33.3°C which indicated the starting point of the transition. The peak temperature (T_{peak}) at 34.4°C can be considered as the transition temperature. In addition, the enthalpy of transition (ΔH) of 0.187 J/g shows the energy required for this transition. Comparison of PNIPAM hydrogel to the suspension of the PNIPAM microgel particles showed a slight increase of the T_{onset} to 33.7°C, T_{peak} to 35°C, and ΔH to 0.203 J/g. The observed slight increases can be explained by an increase of water content in the suspension (46).

These results confirm that the PNIPAM microgel particles maintained thermoresponsive behavior after drying and ball-milling.

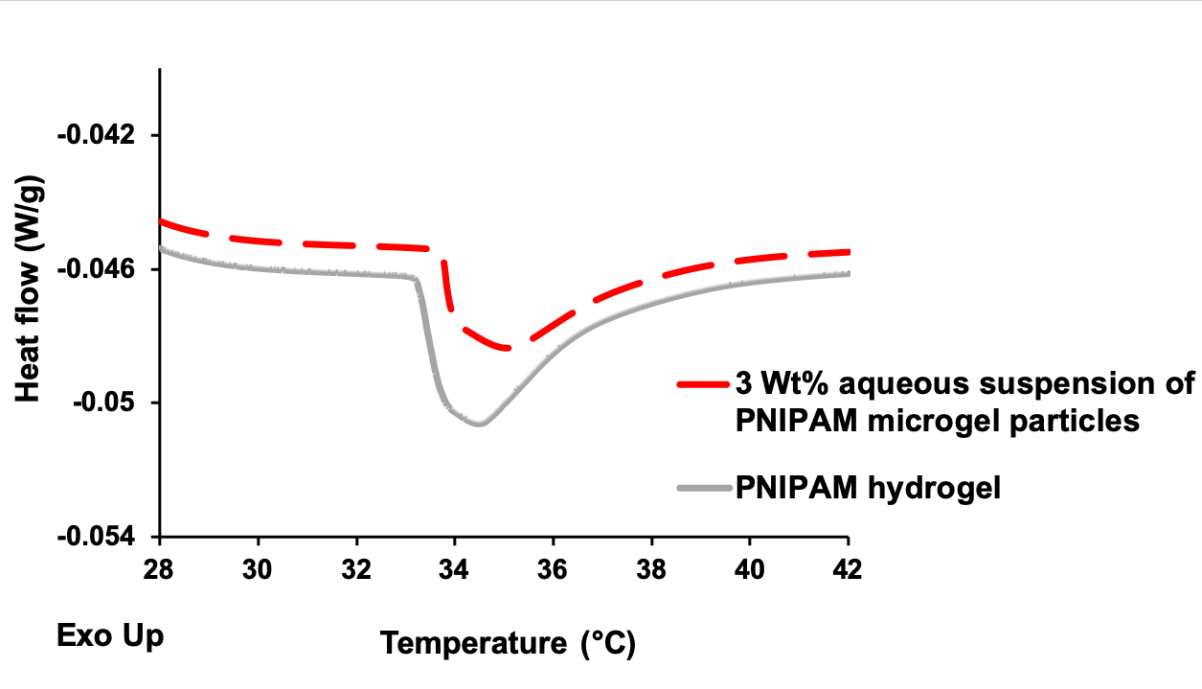

Figure 3.3 DSC thermograms of (——) the PNIPAM hydrogel and (- - -) ball-milled PNIPAM microgel particles in an aqueous suspension of 3 Wt%.

Characterization of the core-shell structured fibers

Morphology of the electrospun fibers was assessed using FESEM imaging of the gold coated fibers. Figure 3.4A and 3.4B show FESEM micrographs of the sample F-AgHG with 10KX and 30KX magnifications, respectively. It can be seen in Figure 3.4A that F-AgHG fibers were continuous and randomly aligned. Moreover, few beads were detected throughout the FESEM assessment of the fiber meshes. Figure 3.4B shows the F-AgHG fibers at higher magnification of 30KX. Some microcracks can be seen on the surface of thinner fibers and some dimples can be seen on the surface of thicker fibers, which have been suggested to be the result of the PCL and PEG phase separation during the electrospinning (47). Fiber diameter distribution

of sample F-AgHG, measured with ImageJ analyzer software, is shown in Figure 3.5. The average fiber diameter was 570 ± 394 nm and the highest frequency of fiber diameter was in the range of 400-600 nm. The fiber structure was of sufficient quality to achieve the nanoparticles delivery goals of the current study. Nevertheless, we propose that it is likely that the fiber structure could be further improved using an electrospinning instrument with more controlled processing conditions.

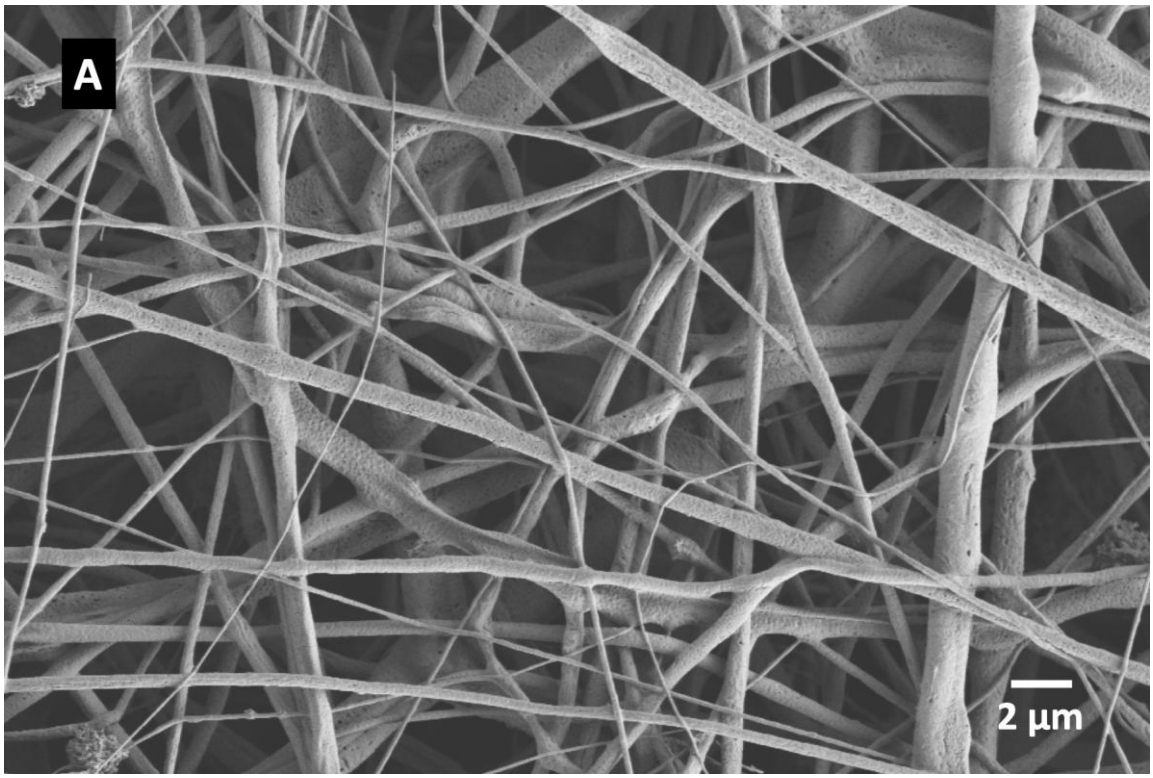

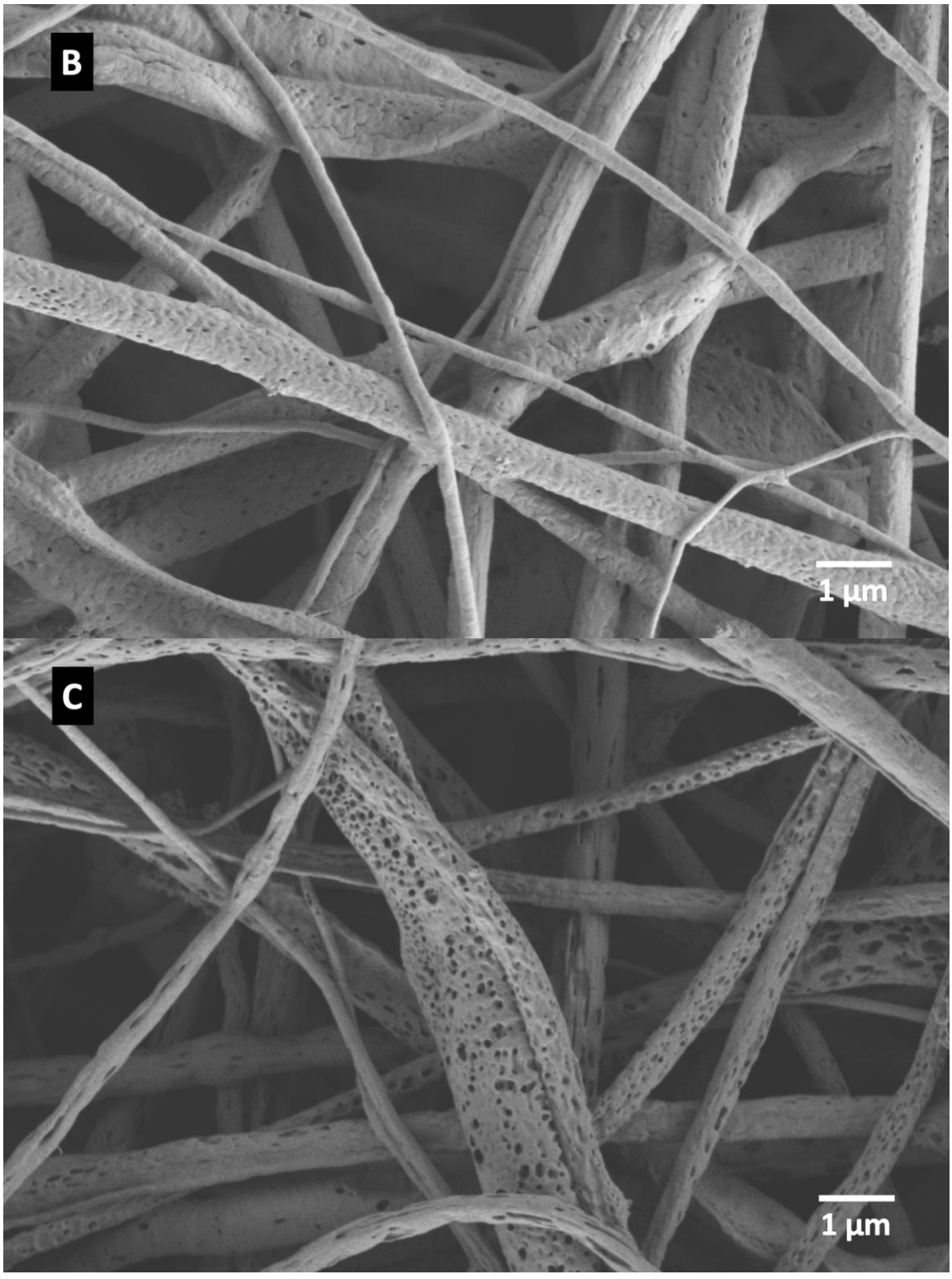
B
1 µm
C
1 µm

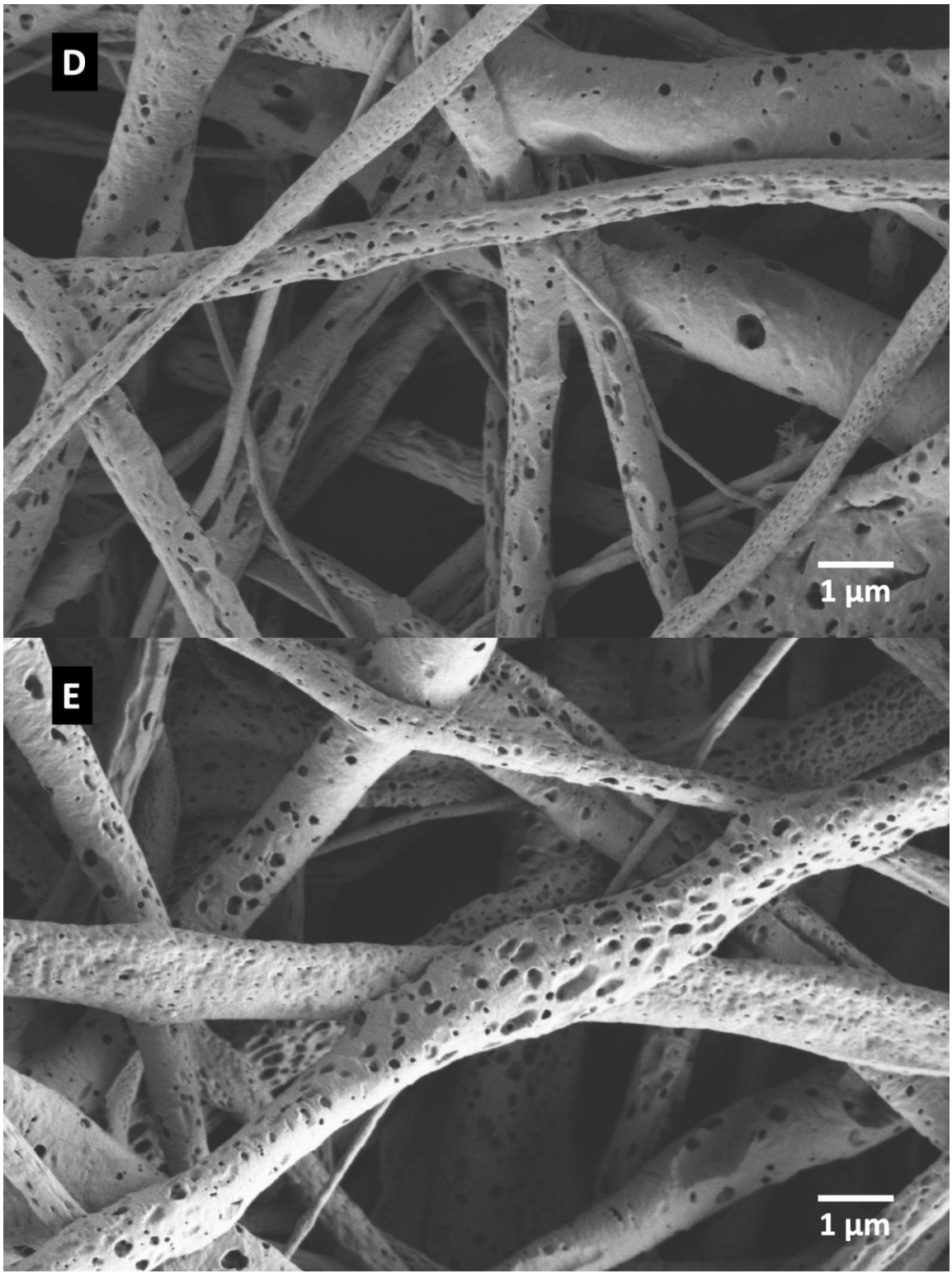
D
1 µm
E
1 µm

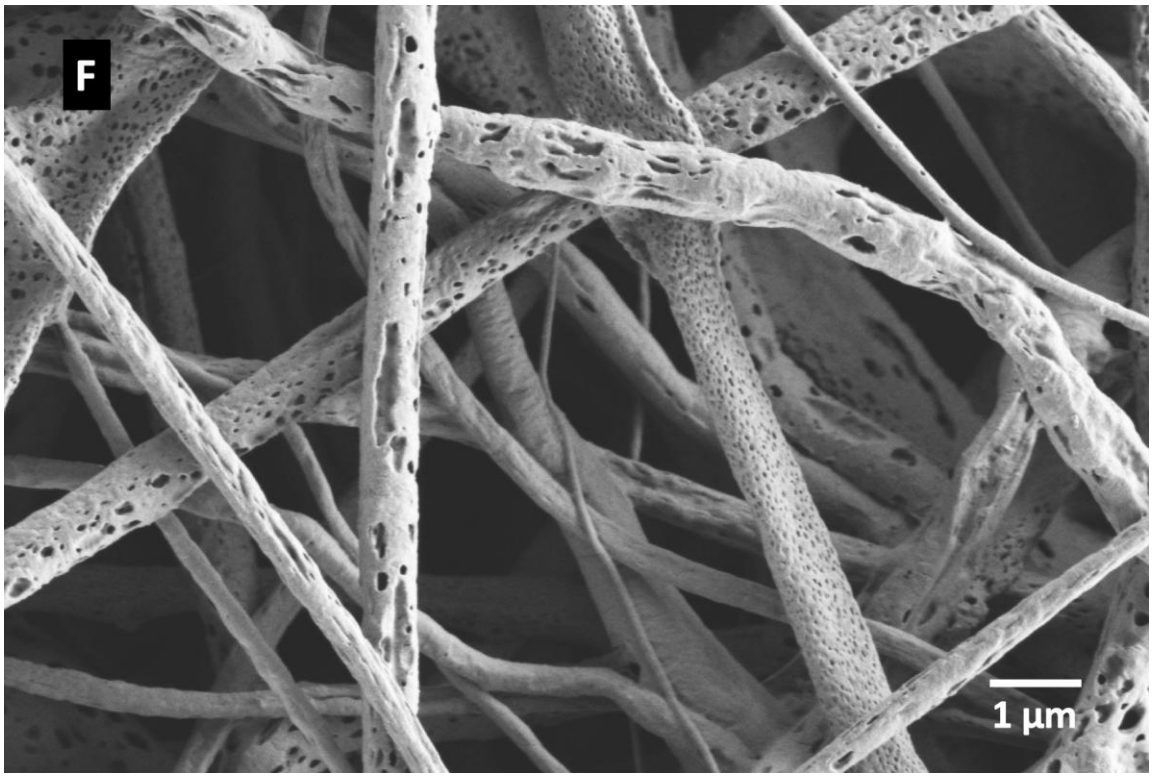

Figure 3.4 FESEM micrographs of electrospun fibers containing PNIPAM microgel particles and Ag NP in the core (sample F-AgHG) (A) before immersion in 10KX magnification, (B) before immersion in 30KX magnification, (C) after one-week immersion at 20°C in 30KX magnification, (D) after one-week immersion at 37°C in 30KX magnification, (E) after two-week immersion at 20°C in 30KX magnification, and (F) after two-week immersion at 37°C in 30KX magnification.

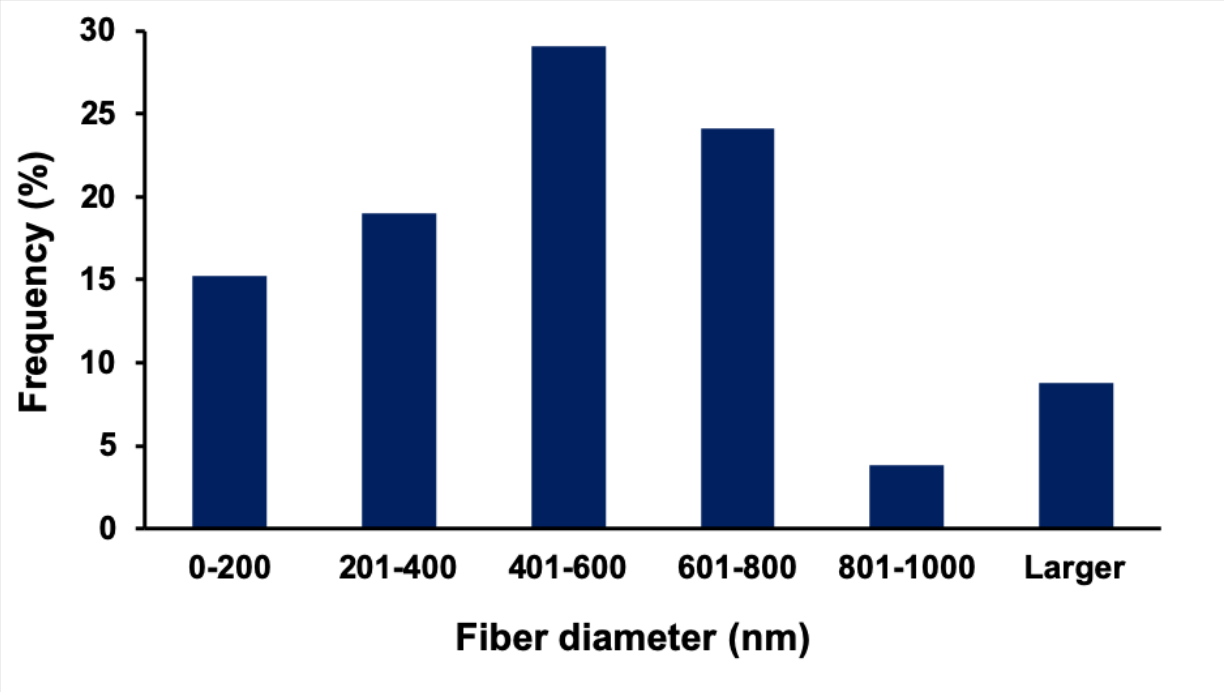

Figure 3.5 Fiber diameter distribution of fiber mesh F-AgHG before pore formation.

Formation of core-shell structured fibers was demonstrated using confocal imaging with fluorescent dextran was added to the core solution to provide a contrast between the fiber core and shell. The fluorescent and transmitted light images are shown in Figure 3.6, indicating the core and the shell. A discrete margin can be seen between the core and the shell in these images showing no mixing of the core and the shell solutions during the electrospinning process. In addition, no leakage of the core was observed during the confocal imaging of the fibers. Imaging of the control fibers (without the addition of fluorescent dextran) was performed to rule out possible background of autofluorescence of fiber components. As expected, confocal images of the control sample had no fluorescent signal confirming that none of the materials used for fabrication of fibers had any background autofluorescence that could have created image artifacts (data not shown).

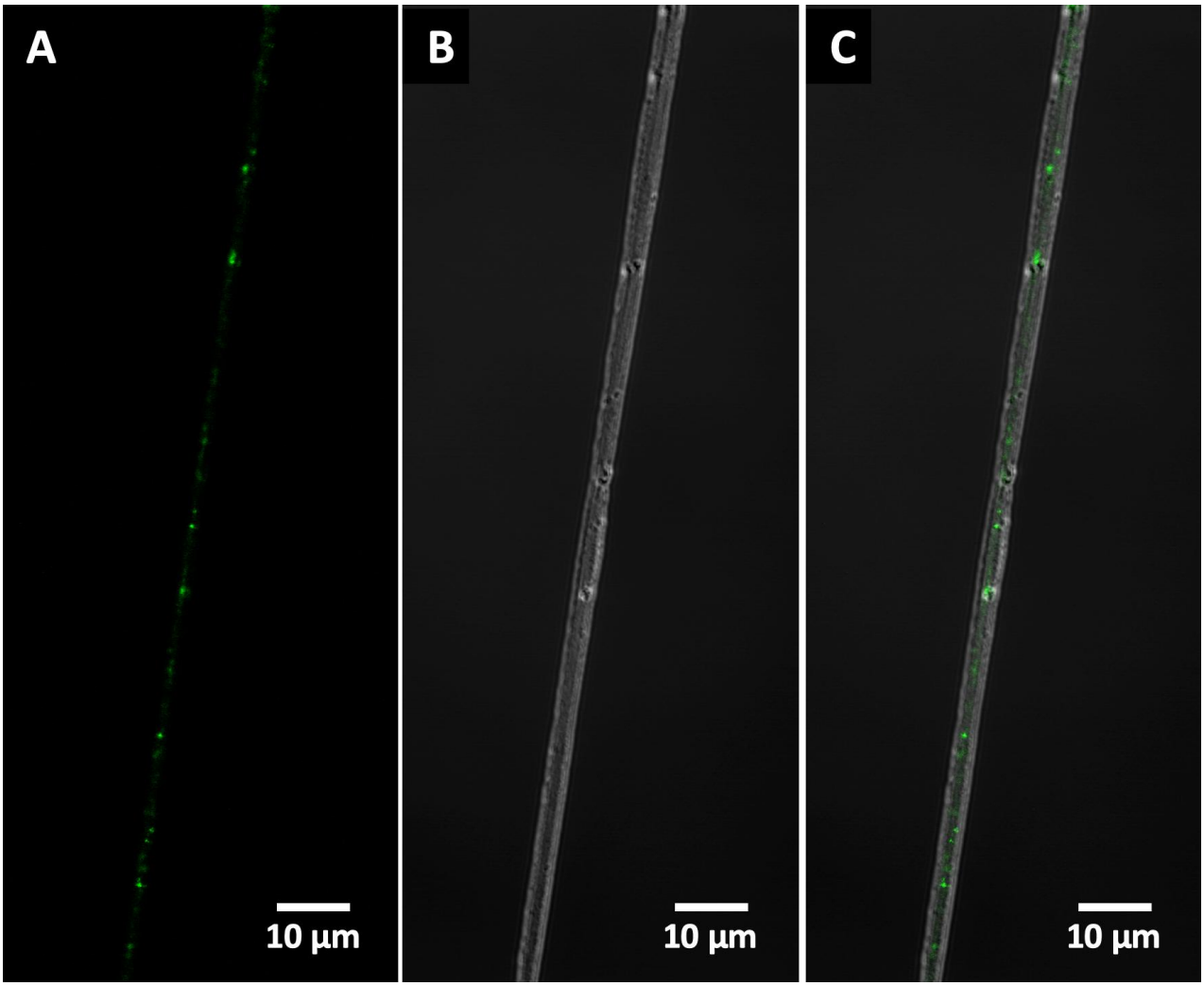

Figure 3.6 Confocal laser scanning micrographs of a fiber of sample F-AgHG: (A) fluorescence channel image, (B) transmitted light channel image, and (C) overlay image.

Characterization of the pore formation in the fiber shell

Pore size and structure, formed via selective dissolution of PEG during immersion in water, was characterized using FESEM imaging. In addition, the effect of immersion temperature on the pore structure was determined. Figure 3.4 shows FESEM micrographs of the F-AgHG fibers after one week (C and D) and two weeks (E and F) of immersion at 20°C or 37°C, respectively. It can be seen in these images that pores were formed, and the fiber structure

was preserved after one or two weeks of immersion at both temperatures. There were no apparent differences between the pore structure at 20°C or 37°C (Figure 3.4C and 3.4E, compared to Figure 3.4D and 3.4F). The similar pore structure at both temperatures can be explained by the high solubility of PEG, which results in its fast dissolution at both temperatures, and thus pore formation within a few minutes of immersion (48). Moreover, there were no changes in the pore structure between one and two weeks of immersion, showing no detectable degradation of fibers.

The degradation of fiber meshes was evaluated by measuring the percent weight loss after immersion. The percent total weight loss of the fiber mesh (F-AgHG) after one and two weeks of immersion at 20°C and 37°C are shown in Table 3.2. The percent total weight loss of one- and two-week immersed fiber meshes were slightly lower at 20°C compared to 37°C and not significantly different. The weight loss (%) observed during the first week was mostly due to the pore formation (dissolution of PEG) and the smaller weight loss observed afterward was most likely due to the minor fiber degradation. Weight loss during the second week of immersion was low at 20°C and 37°C, suggesting minor degradation of fibers at these temperatures. The minor degradation was confirmed with FESEM imaging.

Table 3.2 Percent total weight loss (± SD) after one- and two-week immersion of F-AgHG fiber meshes at 20°C and 37°C.

Weight loss % (± SD)	**Immersed at 20°C**	**Immersed at 37°C**
One-week immersion	26.5 (± 0.54)	27.2 (± 0.8)
Two-week immersion	27.3 (± 0.72)	28.2 (± 0.65)

BET surface area and pore volume analysis was performed on the F-AgHG fiber meshes before and after one-week immersion at 20°C or 37°C to quantify the changes of the fiber surface area and pore volume (Table 3.3). It can be seen in Table 3.3 that both surface area and pore volume increased after one-week immersion at both temperatures. These results confirm pore formation in the fiber shell with immersion at these temperatures. Moreover, the nitrogen adsorption and desorption isotherms had the same profile for all the samples (graphs not shown). These results corroborate similar pore structures as were seen in the FESEM images (Figure 3.4) of samples immersed at 20°C or 37°C and explained by the high solubility of PEG at both temperatures. However, the increases in the surface area and pore volume were about two-fold larger at 37°C compared to 20°C. This could be due to an increased degradation rate of fiber surface at 37°C, which could result in deeper pores or rougher fiber surface (more shallow features on the surface). Therefore, it should be noted that the presence of a higher number of deep pores (connected to the core) can also affect the nanoparticle release rate at 37°C compared to 20°C. Neither of these possibilities (presence of more deep pores or more shallow features) was detected with FESEM imaging described above, thus further analysis with higher resolution, such as atomic force microscopy, could help to further evaluate the surface structure and its effect on nanoparticle release.

Table 3.3 BET surface area and pore volume results for the F-AgHG fiber mesh before immersion and after one-week immersion at 20°C or 37°C.

	Before immersion	**One week immersed at 20°C**	**One week immersed at 37°C**
Surface area (m^2/g)	172	501	956

Pore volume (cm^3/g)	0.35	0.98	1.82

Tensile properties

Mechanical properties of the fiber mesh F-AgHG before immersion, and after one- and two-weeks immersion at 20°C or 37°C were assessed via a tensile test (Figure 3.7). The average ultimate tensile strength, elongation at the break, and Young's modulus measured for three samples at each group are reported in Table 3.4. After one-week immersion, compared to non-immersion, tensile strength and elongation at break had large increases at 20°C or 37°C immersion temperatures, while Young's modulus decreased at both temperatures. Compared to one-week immersion, after two-week immersion, the tensile strength and elongation at break decreased for both temperatures, with larger decreases at 37°C. Young's modulus showed no significant change at either temperature after two weeks.

The improvement of mechanical properties seen in this study can be explained with the annealing of the fiber shell, which provides the mechanical foundation of the core-shell fibers (44). The immersion temperatures of 20°C or 37°C are both in the annealing temperature range of PCL (49), thus the improvement of mechanical properties observed at these temperatures after one-week immersion was due to the annealing mechanism. However, a higher annealing temperature (37°C) also facilitates the degradation mechanism which nullifies the annealing effects (49). The greater degradation at 37°C was confirmed with the higher weight loss observed for fibers immersed at 37°C (compared to 20°C). Consequently, a greater decrease in tensile properties was seen for F-AgHG fiber mesh after the second week of immersion at 37°C. It should be noted that the decline in mechanical properties during the second week of immersion

was small (similar to the weight loss) and the tensile properties were still superior to the non-immersed fiber mesh.

Taken together, these results demonstrate the mechanical stability of the fibers, which was provided by the fiber shell (PCL matrix). However, in previous fiber designs, PNIPAM provided the mechanical foundation of fibers causing poor mechanical properties (15–19). Mechanical stability is crucial for achieving a controlled release of nanoparticles, especially for long-term uses. For example, weak fiber structure causes undefined and unstable pore structure, which results in an uncontrolled release.

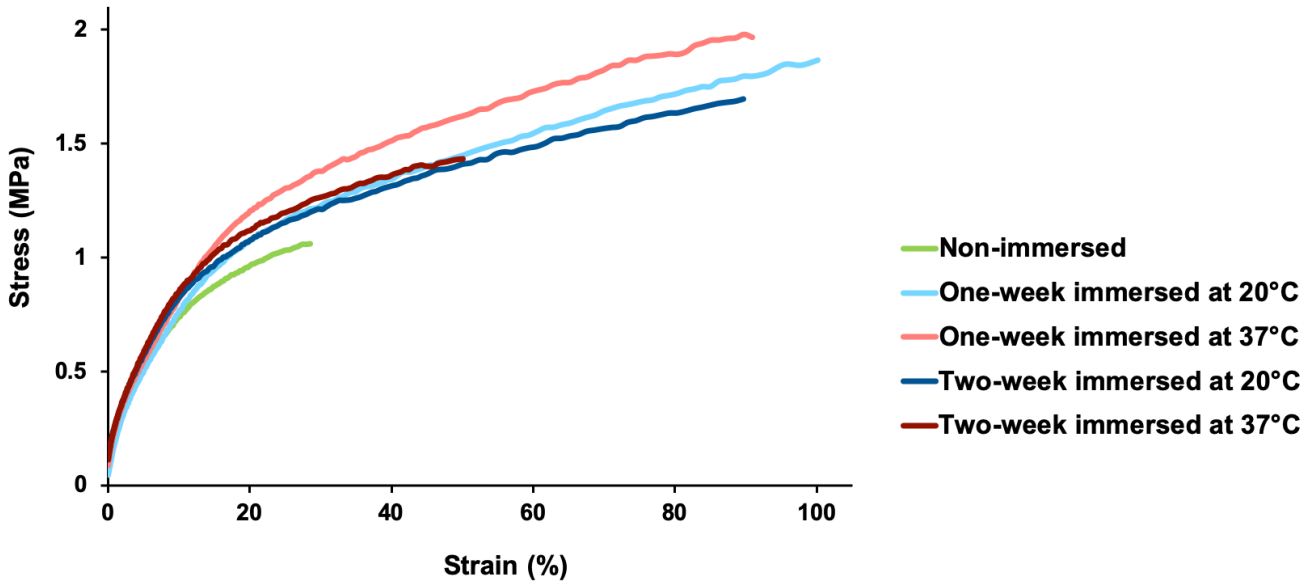

Figure 3.7 Stress-strain curves of sample F-AgHG before immersion and after immersion for one and two weeks at 20°C or 37°C.

Table 3.4 Measured tensile properties (ultimate tensile strength, elongation at break, and Young's modulus) of non-immersed fiber mesh F-AgHG and, one- and two-week immersed at 20°C or 37°C. The SD for n=4 is reported in the parentheses for each measurement.

	Ultimate Tensile Strength (KPa)	**Elongation at Break (%)**	**Young's Modulus (KPa)**
Non-immersed	1059 (± 81.7)	31.1 (± 3.71)	152 (± 8.61)
One-week immersed at 20°C	1793 (± 101)	94.3 (± 6.88)	103 (± 7.13)
One-week immersed at 37°C	1860 (± 168)	86.8 (± 4.12)	122 (± 14.3)
Two-week immersed at 20°C	1596 (± 138)	86.8 (± 4.12)	115 (± 14.3)
Two-week immersed at 37°C	1438 (± 70.1)	46 (± 2.47)	120 (± 4.64)

Release of nanoparticles

The release profile of Ag NP from the fiber mesh containing PNIPAM microgel particles in the core (F-AgHG) was determined at two temperatures, 20°C and 37°C (Figure 3.8). ICP-MS analysis was used to measure the released Ag both in the ionic form and Ag NP. The samples of fiber meshes were immersed in water and at the predetermined time intervals, water samples were collected and analyzed using ICP-MS for the presence of Ag. The nanoparticle release study was performed over the course of two weeks to reflect the long-term use of the electrospun fibers for various applications. Figure 3.8A shows the Ag release profile during the first 8 hours of immersion of F-AgHG fiber meshes at 20°C and 37°C. The amount of released Ag from F-AgHG fiber mesh after one hour of immersion were 5% and 12% at 20°C or 37°C, respectively,

showing no burst release. These results show the advantage of using PNIPAM microgel particles, compared to a non-crosslinked polymer, to avoid the burst release.

Figure 3.8B shows the Ag release profile during the two-week immersion of F-AgHG fiber meshes at 20°C and 37°C. The cumulative Ag release was 34% after two weeks of immersion at 20°C, increasing to 94% after two weeks of immersion at 37°C, or about three (2.8) times faster release rate at 37°C compared to 20°C. This result confirms the thermoresponsive and sustained release of nanoparticles from the fibers, which was achieved via the application of PNIPAM microgel particles in the fiber core and having improved mechanical properties and pore structure in the shell.

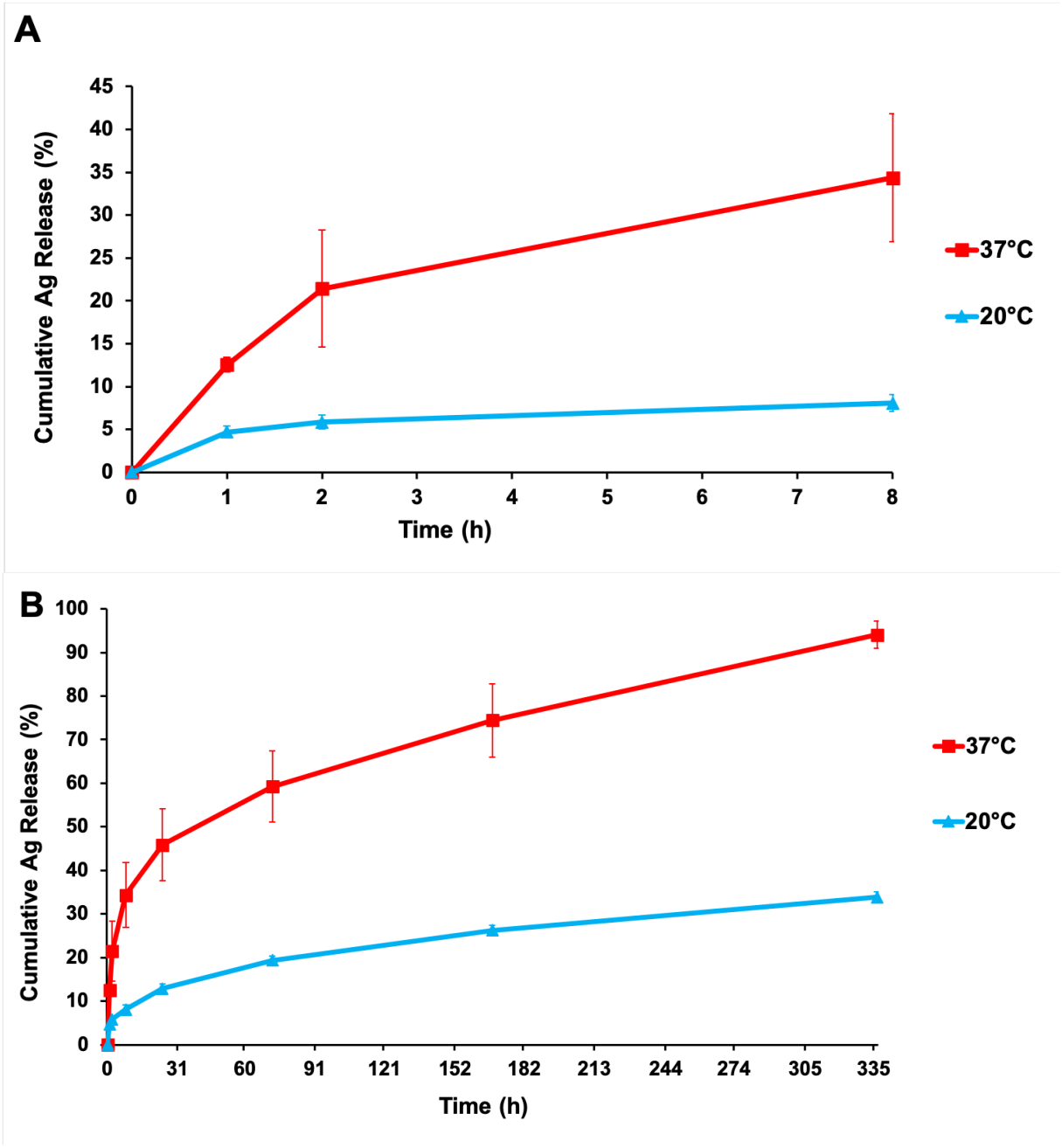

Figure 3.8 Cumulative release of Ag for the fiber mesh F-AgHG at 20°C or 37°C (A) during the first 8 hours of immersion and (B) during the two-week immersion period.

The amount of ZnO NP released from the shell was also measured using ICP-MS. The release profiles of Zn during the two-week immersion of F-AgHG at 20°C or 37°C are shown in Figure 3.9. No burst release was observed in any of the Zn release profiles, suggesting the

association of the ZnO NP mostly with the PCL phase of the fiber shell rather than PEG, which has a fast dissolution rate (44).

Sample F-AgHG immersed at 37°C had a faster sustained Zn release rate compared to the sample F-AgHG immersed at 20°C, showing a temperature-dependent release of Zn. Desorption or leaching of ZnO NP exposed to water on the surface of the fibers was suggested as the release mechanism for Zn (44). Higher molecular interactions at the interphase of the fiber surface and water at higher temperature (37°C) (50) results in the increased rate of Zn release. The increased surface interactions and increased release of ZnO NP were also confirmed with the slightly higher weight loss (Table 3.2) and surface area (Table 3.3) observed for the fiber mesh F-AgHG at 37°C compared to 20°C.

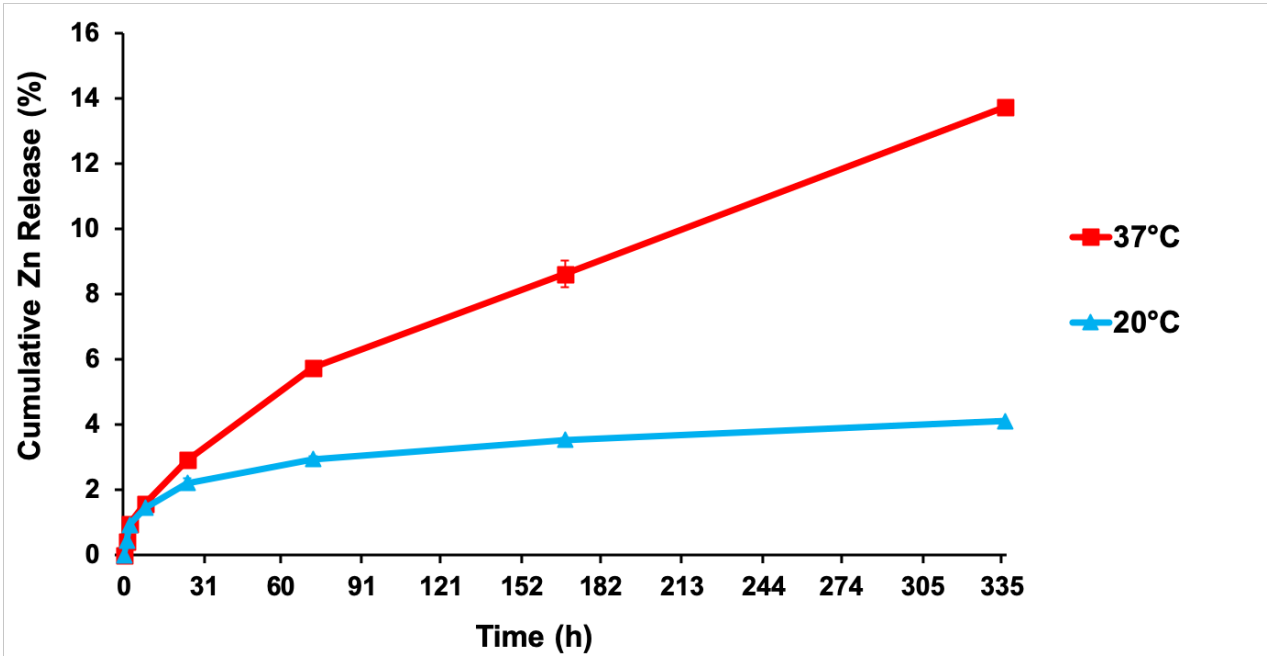

Figure 3.9 Cumulative release of Zn during the two-week immersion period of fiber mesh F-AgHG at 20°C and 37°C.

Release of PNIPAM microgel particles

The possibility of PNIPAM microgel particles being released from fiber meshes was investigated by measuring the OD_{450} of water samples after two-week immersion of fiber meshes at 20°C and 37°C. The OD_{450} measurements did not show any detectable presence of PNIPAM microgel particles (data not shown). The detection limit of the OD_{450} measurement was calculated to be 5.3% of the PNIPAM microgel particles loaded in the fiber core of samples. Therefore, it can be concluded that at least more than 94.7% of the loaded PNIPAM microgel particles remained associated in the fibers, inside the core.

This result is important for future biomedical applications of the designed fibers. This fiber design allows for the application of various microgels regardless of their biocompatibility inside a fiber core because microgel particles remain inside the fiber core and do not release into the tissue through an inconsistent pore structure or mechanical failure of the fibers.

Conclusions

Ball-milling of dried hydrogels was introduced in this study as a simple, versatile, and high-yield method for production of microgel particles. Thermoresponsive PNIPAM hydrogel was synthesized in the bulk form, dried, and ball-milled to produce microgel particles. The PNIPAM microgel particles were then resuspended in water. DLS and DSC analyses showed that the thermoresponsive property of the PNIPAM microgel particles was maintained, i.e. the ball-milling method did not affect the stimuli-responsive properties of the microgel. The main advantage of this method is avoiding the complex chemical processes, which usually requires the use of toxic organic solvents and limits the potential to develop microgel particles with specific properties. For other applications, microgel particles can be filtered to achieve narrow particle size distribution.

A temperature-controlled delivery of nanoparticles was obtained via application of the PNIPAM microgel particles (loaded with Ag NP as a model antibacterial drug) inside the core of electrospun fibers. Loading of the microgel in the core prevents unwanted reactions of the microgel with the electrospinning solvents and possible phase transition during electrospinning. The fiber meshes with PNIPAM microgel particles in the core had superior mechanical stability with increased ductility and strength after immersion in water. At least 94.7% of the PNIPAM microgel particles remained inside the fiber core during the two-week immersion period. Preventing direct contact of the microgel particles and the tissue reduces possible toxicity. Subsequently, biocompatible fiber meshes with various properties can be developed using microgels with specific properties. In future applications, various fragile or bioactive therapeutic agents can be delivered using this design and be protected from the harsh condition of electrospinning or crosslinking.

References

1. Schmaljohann D. Thermo- and pH-responsive polymers in drug delivery. Vol. 58, Advanced Drug Delivery Reviews. Elsevier; 2006. p. 1655–70.

2. Fleige E, Quadir MA, Haag R. Stimuli-responsive polymeric nanocarriers for the controlled transport of active compounds: Concepts and applications. Vol. 64, Advanced Drug Delivery Reviews. Elsevier; 2012. p. 866–84.

3. Ashraf S, Park HK, Park H, Lee SH. Snapshot of phase transition in thermoresponsive hydrogel PNIPAM: Role in drug delivery and tissue engineering. Vol. 24, Macromolecular Research. Polymer Society of Korea; 2016. p. 297–304.

4. Gandhi A, Paul A, Sen SO, Sen KK. Studies on thermoresponsive polymers: Phase behaviour, drug delivery and biomedical applications. Vol. 10, Asian Journal of Pharmaceutical Sciences. Shenyang Pharmaceutical University; 2015. p. 99–107.

5. Kokardekar RR, Shah VK, Mody HR. PNIPAM Poly (N-isopropylacrylamide): A Thermoresponsive "Smart" Polymer in Novel Drug Delivery Systems. Internet J Med Updat. 2012;7(2):60–3.

6. Hu J, Li HY, Williams GR, Yang HH, Tao L, Zhu LM. Electrospun Poly(N-isopropylacrylamide)/Ethyl Cellulose Nanofibers as Thermoresponsive Drug Delivery Systems. J Pharm Sci. 2016 Mar 1;105(3):1104–12.

7. Karimi M, Sahandi Zangabad P, Ghasemi A, Amiri M, Bahrami M, Malekzad H, et al. Temperature-Responsive Smart Nanocarriers for Delivery of Therapeutic Agents: Applications and Recent Advances. Vol. 8, ACS Applied Materials and Interfaces. 2016. p. 21107–33.

8. Zhang CL, Cao FH, Wang JL, Yu ZL, Ge J, Lu Y, et al. Highly Stimuli-Responsive Au Nanorods/Poly(N-isopropylacrylamide) (PNIPAM) Composite Hydrogel for Smart Switch. ACS Appl Mater Interfaces. 2017 Jul 26;9(29):24857–63.

9. Guan Y, Zhang Y. PNIPAM microgels for biomedical applications: From dispersed particles to 3D assemblies. Vol. 7, Soft Matter. The Royal Society of Chemistry; 2011. p. 6375–84.

10. Huang C, Soenen SJ, Rejman J, Lucas B, Braeckmans K, Demeester J, et al. Stimuli-responsive electrospun fibers and their applications. Vol. 40, Chemical Society Reviews. The Royal Society of Chemistry; 2011. p. 2417–34.

11. Gao S, Tang G, Hua D, Xiong R, Han J, Jiang S, et al. Stimuli-responsive bio-based polymeric systems and their applications. Vol. 7, Journal of Materials Chemistry B. Royal Society of Chemistry; 2019. p. 709–29.

12. Song F, Wang XL, Wang YZ. Fabrication of novel thermo-responsive electrospun nanofibrous mats and their application in bioseparation. Eur Polym J. 2011 Oct 1;47(10):1885–92.

13. Rockwood DN, Chase DB, Akins RE, Rabolt JF. Characterization of electrospun poly(N-isopropyl acrylamide) fibers. Polymer (Guildf). 2008 Aug 26;49(18):4025–32.

14. Okuzaki H, Kobayashi K, Yan H. Thermo-responsive nanofiber mats. Macromolecules. 2009;42(16):5916–8.

15. Lin X, Tang D, Lyu H, Zhang Q. Poly(N-isopropylacrylamide)/polyurethane core-sheath nanofibres by coaxial electrospinning for drug controlled release. Micro Nano Lett. 2016 May 1;11(5):260–3.

16. Lin X, Tang D, Cui W, Cheng Y. Controllable drug release of electrospun thermoresponsive poly(N-isopropylacrylamide)/poly(2-acrylamido-2-methylpropanesulfonic acid) nanofibers. J Biomed Mater Res - Part A. 2012 Jul 1;100 A(7):1839–45.

17. Chen M, Dong M, Havelund R, Regina VR, Meyer RL, Besenbacher F, et al. Thermo-responsive core-sheath electrospun nanofibers from poly (N - isopropylacrylamide)/polycaprolactone blends. Chem Mater. 2010;22(14):4214–21.

18. Vihola H, Laukkanen A, Valtola L, Tenhu H, Hirvonen J. Cytotoxicity of thermosensitive polymers poly(N-isopropylacrylamide), poly(N-vinylcaprolactam) and amphiphilically modified poly(N-vinylcaprolactam). Biomaterials. 2005 Jun;26(16):3055–64.

19. Tran T, Hernandez M, Patel D, Burns E, Peterman V, Wu J. Controllable and switchable drug delivery of ibuprofen from temperature responsive composite nanofibers. Nano Converg. 2015;2(1).

20. Jiang S, Liu F, Lerch A, Ionov L, Agarwal S. Unusual and Superfast Temperature-Triggered Actuators. Adv Mater. 2015 Sep;27(33):4865–70.

21. Kim YJ, Ebara M, Aoyagi T. Temperature-responsive electrospun nanofibers for "on-off" switchable release of dextran. Sci Technol Adv Mater. 2012;13(6).

22. Haq MA, Su Y, Wang D. Mechanical properties of PNIPAM based hydrogels: A review. Vol. 70, Materials Science and Engineering C. Elsevier Ltd; 2017. p. 842–55.

23. Zhang H, Niu Q, Wang N, Nie J, Ma G. Thermo-sensitive drug controlled release PLA core/PNIPAM shell fibers fabricated using a combination of electrospinning and UV photo-polymerization. Eur Polym J. 2015 Oct 29;71:440–50.

24. Jiang H, Wang L, Zhu K. Coaxial electrospinning for encapsulation and controlled release of fragile water-soluble bioactive agents. J Control Release. 2014 Nov 10;193:296–303.

25. Hathaway H, Ajuebor J, Stephens L, Coffey A, Potter U, Sutton JM, et al. Thermally triggered release of the bacteriophage endolysin CHAPK and the bacteriocin lysostaphin for the control of methicillin resistant Staphylococcus aureus (MRSA). J Control Release. 2017 Jan 10;245:108–15.

26. Salehi R, Irani M, Rashidi MR, Aroujalian A, Raisi A, Eskandani M, et al. Stimuli-responsive nanofibers prepared from poly(N-isopropylacrylamide- acrylamide-vinylpyrrolidone) by electrospinning as an anticancer drug delivery. Des Monomers Polym. 2013 Nov 27;16(6):515–27.

27. Wellert S, Richter M, Hellweg T, Von Klitzing R, Hertle Y. Responsive Microgels at Surfaces and Interfaces. Z Phys Chem. 2015;229(8):1225–50.

28. Eichenbaum GM, Kiser PF, Simon SA, Needham D. pH and ion-triggered volume response of anionic hydrogel microspheres. Macromolecules. 1998 Jul 28;31(15):5084–93.

29. Noro A, Hayashi M, Matsushita Y. Design and properties of supramolecular polymer gels. Vol. 8, Soft Matter. 2012. p. 6416–29.

30. Ramos J, Imaz A, Callejas-Fernández J, Barbosa-Barros L, Estelrich J, Quesada-Pérez M, et al. Soft nanoparticles (thermo-responsive nanogels and bicelles) with biotechnological applications: From synthesis to simulation through colloidal characterization. Vol. 7, Soft Matter. 2011. p. 5067–82.

31. Ward MA, Georgiou TK. Thermoresponsive polymers for biomedical applications. Polymers (Basel). 2011 Sep;3(3):1215–42.

32. Welsch N, Ballauff M, Lu Y. Microgels as Nanoreactors: Applications in Catalysis. In Springer, Berlin, Heidelberg; 2010. p. 129–63.

33. Pich A, Richtering W. Chemical Design of Responsive Microgels. Springer Berlin; 2013.

34. Dai Z, Ngai T. Microgel particles: The structure-property relationships and their biomedical applications. J Polym Sci Part A Polym Chem. 2013 Jul 15;51(14):2995–3003.

35. Fernandez-Nieves A, Wyss HM, Mattsson J, Weitz DA. Microgel Suspensions: Fundamentals and Applications. John Wiley & Sons. Weinheim, Germany: Wiley-VCH Verlag GmbH {&} Co. KGaA; 2011. I--XXI.

36. Shewan HM, Stokes JR. Review of techniques to manufacture micro-hydrogel particles for the food industry and their applications. Vol. 119, Journal of Food Engineering. Elsevier; 2013. p. 781–92.

37. Stokes JR. Rheology of Industrially Relevant Microgels. In: Microgel Suspensions. Weinheim, Germany: Wiley-VCH Verlag GmbH & Co. KGaA; 2011. p. 327–53.

38. Das M, Zhang H, Kumacheva E. MICROGELS: Old Materials with New Applications. Annu Rev Mater Res. 2006;36:117–59.

39. Xia T, Hamilton RF, Bonner JC, Crandall ED, Elder A, Fazlollahi F, et al. Interlaboratory Evaluation of in Vitro Cytotoxicity and Inflammatory Responses to Engineered Nanomaterials: The NIEHS Nano GO Consortium. Environ Health Perspect. 2013 Jun;121(6):683–90.

40. Hamilton R, Buckingham S, Holian A. The Effect of Size on Ag Nanosphere Toxicity in Macrophage Cell Models and Lung Epithelial Cell Lines Is Dependent on Particle Dissolution. Int J Mol Sci. 2014 Apr 22;15(4):6815–30.

41. Kazutoshi Haraguchi *, Toru Takehisa and, Fan† S. Effects of Clay Content on the Properties of Nanocomposite Hydrogels Composed of Poly(N-isopropylacrylamide) and Clay. 2002;

42. Panchal J, Kotarek J, Marszal E, Topp EM. Analyzing Subvisible Particles in Protein Drug Products: a Comparison of Dynamic Light Scattering (DLS) and Resonant Mass Measurement (RMM). AAPS J. 2014 May 26;16(3):440–51.

43. Goldburg WI. Dynamic light scattering. Am J Phys. 1999 Dec 29;67(12):1152–60.

44. Mahdieh Z, Mitra S, Holian A. Electrospun fibers with an improved pore structure for controlled delivery of nanoparticles. ACS Appl Mater Interfaces. 2020;(am-2020-04409t).

45. Little L, Mainza AN, Becker M, Wiese J. Fine grinding: How mill type affects particle shape characteristics and mineral liberation. Miner Eng. 2017 Sep 1;111:148–57.

46. Song L, Lin J, Liu P, Li J, Jiang S, Huang D. Quantitative determination of the spring entropy effect and its indication of the conformational change of polymer coils with varying concentration in aqueous poly(N-isopropylamide) solutions. RSC Adv. 2019;9(10):5540–9.

47. Zhang YZ, Feng Y, Huang ZM, Ramakrishna S, Lim CT. Fabrication of porous electrospun nanofibres. Nanotechnology. 2006;17(3):901–8.

48. Corrigan OI, Murphy CA, Timoney RP. Dissolution properties of polyethylene glycols and polyethylene glycol-drug systems. Int J Pharm. 1979 Nov;4(1):67–74.

49. Abhari RE, Mouthuy PA, Zargar N, Brown C, Carr A. Effect of annealing on the mechanical properties and the degradation of electrospun polydioxanone filaments. J Mech Behav Biomed Mater. 2017 Mar 1;67:127–34.

50. Cussler EL. Mass Transfer in Fluid Systems. Cambridge University Press; 2009.

Supplementary data of chapter 3

Table 1. The Holm-Sidak's multiple comparisons test results for the total weight loss of fiber meshes with immersion at 20°C and 37°C reported in Table 3.2. Asterisks indicate significant difference ****$p < 0.0001$, ***$p < 0.0002$, **$p < 0.0021$, *$p < 0.0332$, $^{ns}P > 0.1234$.

	Immersed at 20°C vs. Immersed at 37°C
One-week immersion	ns
Two-week immersion	ns

Table 2. The Holm-Sidak's multiple comparisons test results for measured tensile properties of non-, one-, and two-week immersed fiber mesh F-AgHG at 20°C and 37°C reported in Table 3.4. Asterisks indicate significant difference ****p < 0.0001, ***p < 0.0002, **p < 0.0021, *p < 0.0332, ^{ns}P > 0.1234.

	Ultimate Tensile Strength	Elongation at break	Young's Modulus
Non-immersed vs. One-week immersed at 20°C	****	****	***
Non-immersed vs. One-week immersed at 37°C	****	****	**
Non-immersed vs. Two-week immersed at 20°C	****	****	**
Non-immersed vs. Two-week immersed at 37°C	**	**	**
One-week immersed at 20°C vs. One-week immersed at 37°C	ns	ns	ns
One-week immersed at 20°C vs. Two-week immersed at 20°C	ns	ns	ns
One-week immersed at 20°C vs. Two-week immersed at 37°C	**	****	ns
One-week immersed at 37°C vs. Two-week immersed at 20°C	*	ns	ns
One-week immersed at 37°C vs. Two-week immersed at 37°C	***	****	ns
Two-week immersed at 20°C vs. Two-week immersed at 37°C	ns	****	ns

Table 3. The Holm-Sidak's multiple comparisons test results for the percent cumulative release of Ag from fiber meshes reported in Figure 3.8B. Asterisks indicate significant difference ****p < 0.0001, ***p < 0.0002, **p < 0.0021, *p < 0.0332, ^{ns}P > 0.1234.

	F-AgHG at 37°C vs. F-AgHG at 20°C	F-Ag20 at 37°C vs. F-AgHG at 37°C	F-Ag20 at 37°C vs. F-AgHG at 20°C
1h	ns	***	****
2h	***	*	****
8h	****	ns	****
24h	****	ns	****
72h	****	ns	****
168h	****	*	****
336h	****	***	****

Table 4. The Holm-Sidak's multiple comparisons test results for the percent cumulative release of Zn from fiber meshes reported in Figure 3.9. Asterisks indicate significant difference ****p < 0.0001, ***p < 0.0002, **p < 0.0021, *p < 0.0332, ^{ns}P > 0.1234.

	F-AgHG at 37°C vs. F-AgHG at 20°C	F-Ag20 at 37°C vs. F-AgHG at 37°C	F-Ag20 at 37°C vs. F-AgHG at 20°C
1h	ns	ns	ns
2h	ns	ns	ns
8h	ns	ns	ns
24h	ns	*	**
72h	****	***	****
168h	****	****	****
336h	****	****	****

Chapter 4: *In vitro* and *in vivo* evaluations of electrospun fiber meshes

Contributions

Zahra Mahdieh, University of Montana: Primary author responsible for development of project and design of experiments. Responsible for animal use protocol. Performed electrospinning processes and sample preparations, antibacterial assays, *in vitro* cytotoxicity assays, animal studies, tissue collection, histological staining, hyperspectral microscopy, bright field microscopy, statistical analyses.

Andrij Holian, University of Montana: Supervised project development and experimental design. Reviewed final paper submission.

Gretchen McCaffrey, University of Montana: Provided editorial guidance for preparation of paper.

Britten Postma, University of Montana: Primary author of animal use protocol. Performed and provided training for animal studies.

Lou Harriette, University of Montana: Provided training for tissue collection and bright field microscopy. Performed histological staining.

Ray Hamilton, University of Montana: Provided training for hyperspectral imaging, *in vitro* cytotoxicity assay, and statistical analyses.

Jim Driver, University of Montana: Provided training and resource support for antibacterial studies.

Joseph (Fred) Rhoderick, University of Montana: Provided training for antibacterial studies.

Kevin Trout, University of Montana: Constructed electrospinning hardware and provided training for electrospinning.

Chris Palmer, University of Montana: Provided resource support for syntheses of hydrogels.

Abstract

In vitro studies are of the primary steps in development of new biomaterials. *In vitro* studies provide rapid information on efficacy of potential biomaterials. *In vitro* studies are fast, cost efficient, and have fewer ethical restrictions, however, they cannot accurately mimic a live biological system. *In vivo* studies are of the next steps to be performed for extrapolating information on the expected performance and safety of biomaterials when in use. *In vivo* studies are especially important in development of drug delivery systems because body biokinetics can alter the drug release mechanisms in unpredicted ways. In this study, drug delivery performance of developed fiber meshes was thoroughly evaluated *in vitro* and *in vivo.* Fiber meshes were loaded with silver nanoparticles (Ag NP) and the delivery rate was controlled via application of different sizes of NP and via application of thermoresponsive poly(n-isopropylacrylamide) (PNIPAM) hydrogel particles. Fiber meshes also contained ZnO NP which have antibacterial and wound healing properties. *In vitro* studies showed antibacterial efficacy of the fiber meshes. *In vivo* studies showed continuous release of Ag NP during 27 days of subcutaneous implantation. ZnO NP induced cytotoxicity *in vitro* while improved the wound healing and hair regrowth *in vivo*.

Introduction

Development of alternative drug delivery systems has gained attention in pharmaceutical research to improve effectiveness of treatments, prevent or reduce side effects of drugs, decrease costs and patient discomfort (1–4). With new delivery systems, unpredicted changes in the performance of such systems can result in toxicity and/or reduce the efficacy of the intended drug delivery. Therefore, it is vital to perform a thorough validation of such systems to ensure that quality performance of any new system is maintained without introducing unusual effects. There are a number of steps involved in the process. Dissolution/immersion testing also known as "*in vitro* release testing" is an important initial quality control test for predicting the *in vivo* performance of drug delivery systems after it was officially approved in 1970 (5,6). However, considering the complexity of the dynamics and structure of human body, the *in vitro* release testing method falls short of safely predicting *in vivo* performance.

The situation is more complicated when working with nanoparticles or smart drug delivery systems since they are novel, more difficult to characterize, and often have unique properties (7). Since no standard *in vitro* testing has been developed for quality and performance testing of nanoparticles and smart drug delivery systems, *in vivo* animal study is still the most reliable testing method (8,9). Therefore, *in vitro* antibacterial and cytotoxicity assays in addition to animal studies need to be performed to ensure the quality performance of the fiber meshes especially those using novel materials such as nanoparticles.

In prior work, fiber meshes were designed to achieve controlled and smart delivery of nanoparticles (10,11). The fibers have a core-shell structure containing silver nanoparticles (Ag NP, as a model drug) loaded inside fiber core and include pores formed in the fiber shell to provide a release pathway. The pore structure and mechanical stability of the fibers were

improved via novel use of zinc oxide nanoparticles (ZnO NP). Three different release rates were achieved via application of 20 nm Ag NP, 110 nm Ag NP, and a mixture of both nanoparticles in the core. Drug delivery with controlled rate was further upgraded to a smart delivery by applying thermoresponsive Poly(n-isopropylacrylamide) (PNIPAM) microgel particles inside the fiber core. *In vitro* release testing confirmed the temperature-controlled release of Ag NP.

In the current study, *in vitro* antibacterial efficacy of the fiber meshes was determined. An MTS assay was used to evaluate the *in vitro* cytotoxicity of A549 epithelial cells by the fiber meshes. Subcutaneous implantation of the fiber meshes in a mouse model was performed to confirm the *in vivo* release of Ag NP form the fiber meshes. The subcutaneous implantation of fiber meshes, which can represent *in vivo* drug delivery performance for cancer treatment (3,12), tissue engineering (13–15), and wound healing (16,17) applications, was performed on a mouse model. Biocompatibility, wound healing, anti-infection, and biodegradation properties of the fiber meshes were assessed during the 27 days of implantation.

Materials and methods

Fiber meshes loaded with 20 nm Ag NP (F-Ag20 and F-AgHG) were chosen for the *in vitro* and *in vivo* studies since they had the fastest release rate of Ag NP (10,11). Fiber meshes F-PPZn and F-PP were used as negative control for Ag NP and ZnO NP, respectively. The data in Table 4.1 represent the designation and composition of the fiber meshes used in this study.

Table 4.1 The core and shell compositions of fabricated fiber meshes and their corresponding sample name.

Sample	Core composition	Shell composition		
		PCL (Wt%)	PEG (Wt%)	ZnO NP (Wt%)
F-Ag20	0.02 Wt% Ag NP	14	7	1.6
F-AgHG	0.01 Wt% Ag NP + 3 Wt% PNIPAM Microgel particles	14	7	1.6
F-PPZn	Water	14	7	1.6
F-PP	Water	14	7	-

Antibacterial assay

E. coli (Migula Castellani and Chalmers, ATCC® 29842, USA) bacteria were cultured in standard Luria-Bertani (LB, Invitrogen™ , Gibco®, USA) medium on a shaker (150 rpm, 0.3 cm orbit motion, Thermo Labline 4625 Titer Shaker, USA) in an incubator (37°C). Initial incubation of bacterial suspension was continued until an OD_{600} of 0.1 was obtained, then it was used as the bacterial stock. Measurements at OD_{600} were used as a monitor of bacterial growth in a similar manner as previously described (18). The OD_{600} was measured by transferring 100 µL of bacterial aliquots into 96 microwell plates and reading the optical density at 600 nm (OD_{600}, SpectraMax M4 multi-mode microplate reader, Molecular devices, USA) to determine bacterial activity.

In order to determine the antibacterial potential of each of the fiber mesh, four equal pieces were cut out of each fiber meshes (F-AgHG, F-Ag20, F-PP and F-Zn) using a punch (12.7 mm diameter, Jenley hollow leather punch) then quickly detached from the aluminum foil in

water and placed in each well of 24-well plates. To investigate a possible effect of the PNIPAM microgel particles on the antibacterial activity, a 200 µL suspension of 3 Wt% PNIPAM microgel particles was added into separate wells. It was calculated that a total of 85 µL PNIPAM microgel particles suspension was inside the fiber mesh samples used for the assay. Therefore, to evaluate a possible antibacterial activity caused by PNIPAM microgel particles, 200 µL (which is more than 85 µL for safe measurements) was used. Three replicate wells were used for each measurement (error bars represent standard deviation (SD) for n=3).

Experiments were started (at 0 h) by addition of 2 mL of bacterial suspension from the stock (with OD_{600} of 0.1) into each well. The control was 2 mL of bacterial suspension from the stock added into empty wells. Cultures were continued for 24 hours and the OD_{600} measurements were performed hourly for 10 h and then at 24 h to obtain the bacterial growth curves. PNIPAM microgel particles become opaque at 37°C and could skew the OD_{600} measurements results. Therefore, aliquots for OD_{600} measurements were gently collected by careful insertion of the pipet tip into the bacterial suspensions to avoid collecting the PNIPAM microgel particles.

Cytotoxicity assay

The MTS assay was performed using A549 human lung epithelial cells obtained from ATCC. Cells were suspended in Ham's F-12K (Kaighn's) Medium (Gibco™ by Life Technologies™, USA) supplemented with 10% fetal bovine serum, 250 ng/mL amphotericin B, and 100 U/mL penicillin and Streptomycin in 75 cm^2 flasks at 37 °C (all supplements provided from Media Tech, Manassas, VA, USA). Since A549 cells are adherent, trypsin was used to dislodge the cells for MTS assay. The cells were centrifuged at 950 x g for 4 minutes and the cells were resuspended in 5 mL of media. A 40 µL volume was counted with a Z2 Coulter Counter (Beckman Coulter, FL, USA).

Equal circles were cut from fiber meshes using a 5.5 mm diameter punch (Jenley hollow leather punch, Yiwu Jiede Electronic Commerce Co.). Fiber meshes were immersed in water for one hour to form pores required for Ag NP release. Fiber meshes were sterilized by soaking in (100%) ethanol for 10 seconds then placed in 96-well plates to dry. Afterwards, 100 µL of the A549 cell suspension was added into the wells at 15,000 cells/well and cultured for 24 hours. Cell viability was determined using CellTiter assay (Promega, WI, USA) according to the manufacturer's protocol (19). Cell viability was calculated as the percent viable cells relative to the control cultures (which had no fiber meshes). Blanks were also defined as media, without cells, added to the fiber meshes. Data are the presented as mean ± standard error (SE) calculated from three experiments with three replicates in each.

In vivo experimental design and surgical implantation

All animal procedures were approved by the Institutional Animal Care and Use Committee of the University of Montana. Male and female C57BL/6 mice (7-8 weeks, 15-25 g body weight) were used. Animals were grouped as skin control (no surgery), sham surgery (surgery was performed without implanting a fiber mesh), and groups implanted with F-Ag, F-AgHG, F-PPZn, F-PP fiber meshes. 24 h, 7 days, and 27 days were selected to observe the outcomes from fiber mesh implants. Two male and two female mice were implanted for each group and each time point. Fiber meshes were cut in squares (~ 6 mm × 6 mm) and soaked in water then ethanol each for 10 seconds prior to surgery. For surgery, animals were anaesthetized by intraperitoneally injecting 100 mg/kg body weight of a ketamine (80 mg/kg)/xylazine (12 mg/kg) cocktail with 9/1 volume ratio. The dorsal hair was shaved and skin was prepared with ethanol (70%), povidone-iodine, and lidocaine (4%), alternatively. A 1.5 cm longitudinal cut was created on the right dorsal flank and a pouch was created using forceps. Fiber meshes were

implanted into the left side of the dorsal pouch and the incision was closed using surgical glue. Animals were placed on heating pads to recover from anesthesia. Mice were housed individually after the surgery and fed ad libitum.

Tissue collection and histological staining

After 24 h, 7 days, and 27 days, animals were euthanized by barbiturate overdose injection. A square area of skin around the fiber mesh was cut with surgical scissors. Skin and fiber mesh were dissected free of adherent tissue, placed in OCT compound (Sakura Finetek USA Inc., CA, USA), and snap frozen using liquid nitrogen. To obtain cross-sections of tissue samples, the frozen OCT blocks were cut at the center, placed vertically in OCT, and snap frozen using liquid nitrogen. Tissue samples were cryo-sectioned into 10 μm sections. Sections were stained with hematoxylin and eosin (H&E).

Hyperspectral microscopy

CytoViva hyperspectral microscopy (CytoViva Inc, Auburn, Al, USA) was used to determine the release of Ag NP from fiber meshes into the mouse skin tissue. Hyperspectral images were captured with CytoViva Micro-Manger 1.4 and processed with CytoViva ENVI 4.8 image analysis software. A spectral library was created from a hyperspectral image captured from a dried droplet of Ag NP suspension on a slide. The created spectral library was filtered against skin control and F-PP to exclude any non-specific match with tissue or the fiber mesh without Ag NP. Subsequently, spectral Angle Mapper Classification was used to map the matching pixels of Ag NP on the tissue samples.

Statistical analyses

Statistical analyses were performed using a one- or two-way ANOVA followed by individual comparison of groups using Holm-Sidak's multiple comparisons test (PRISM v.7.0, GraphPad, San Diego, CA, USA). The Holm-Sidak's multiple comparison results are reported at supplementary data of chapter 4. A statistical significance level of 5% ($p < 0.05$) was defined. The minimum number of replicates was three. Values were reported as Mean ± SD.

Results and discussion

Antibacterial efficacy

Antibacterial efficacy of fiber meshes was evaluated from their ability to inhibit bacterial growth, as shown in bacterial growth curves Figure 4.1. It can be seen in Figure 4.1 that the starting OD_{600} was 0.1 for all samples, showing similar starting conditions. As expected, the bacterial growth curve of the control increased continuously until the end of the experiment (24 h) excluding possible factors to limit bacterial growth, such as lack of nutrients. The bacterial growth curves of sample HG-200µL had no significant difference from control, showing that the PNIPAM microgel particles had no antibacterial activity. Similarly, the bacterial growth curve of F-PP was not significantly different from the control. This result eliminates any possible masking or interfering factors such as attachment of bacteria to the fibers or growth inhibitory effects of PCL and PEG.

In contrast, significant (Supplementary Data Table 1) inhibition was seen from the bacterial growth curves of fiber meshes F-Ag20, F-AgHG, and F-PPZn compared to the growth curve of control, demonstrating highly effective antibacterial activity of the fiber meshes (18). In

fact, after 24-hour incubation with the fiber meshes, bacterial growth curves decreased to an OD_{600} of 0.46 which is the OD_{600} of broth without bacteria. The observed antibacterial activity can be attributed to the release of Ag NP and ZnO NP (20). However, comparing the samples F-Ag20 and F-PPZn reveals that the antibacterial activity was dominated by ZnO NP. This result could be due to the higher amount of ZnO NP in the shell (1.6 Wt%), compared to Ag NP in the core (0.02 Wt%), and/or higher antibacterial activity of ZnO NP compared to Ag NP. It should be noted that the primary purpose for including ZnO NP in this research was to achieve open pores, but it was also an effective antibacterial (11).

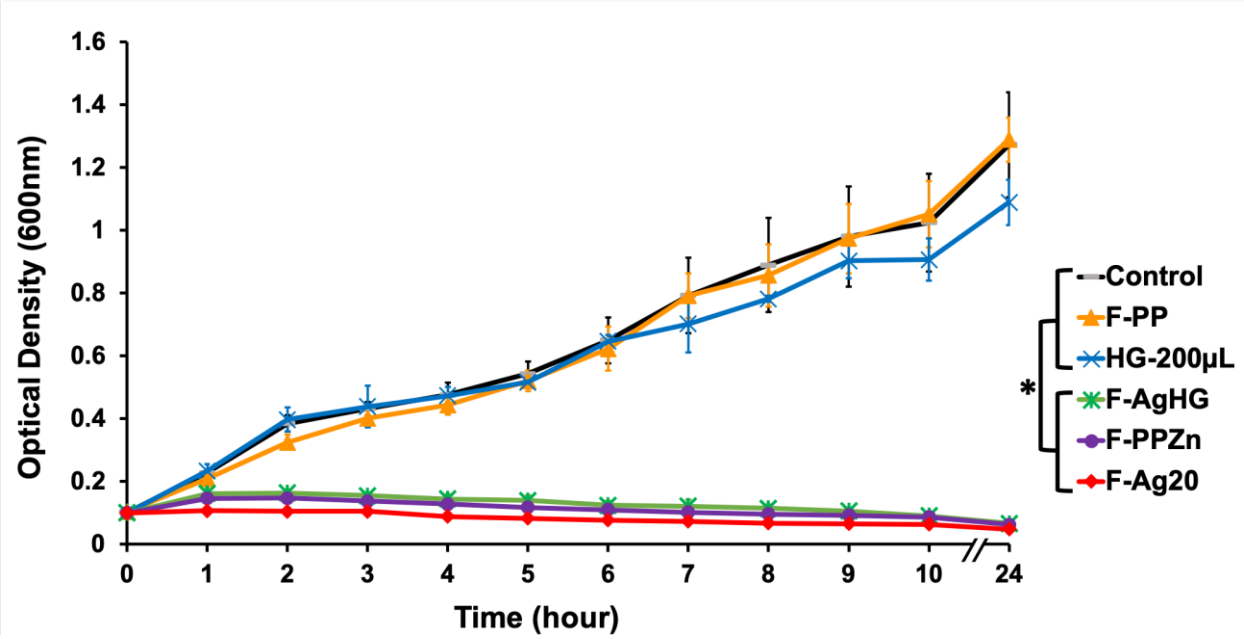

Figure 4.1 Growth curves of E. coli during 24 h of incubation at 37°C with fiber meshes F-AgHG (✱), F-PPZn (●), and F-Ag20 (◆) compared to the control (-), F-PP (▲), and HG-200 µL (X). Asterisk indicates a significant difference of (*$p < 0.0001$, Supplementary Data Table 1). Data are expressed as mean ± SD of n = 4.

Cytotoxicity

In vitro MTS assays were performed to determine potential cytotoxicity of the fiber meshes with cells in culture. The percent cell viability data relative to the control are presented in Figure 4.2. The fiber mesh F-PP had the least effect on viability most likely due to absence of ZnO NP and Ag NP. The reason for decrease in viability of F-PP compared to control was not clear. Addition of ZnO NP into the fiber mesh F-PPZn reduced the cell viability to 28% consistent with known ZnO NP cytotoxicity (21,22). The cell viability was slightly improved (but not significant, Supplementary Data Table 2) when Ag NP were in the fiber meshes (F-Ag20 and F-AgHG). Similar results were reported with loading ZnO NP and Ag NP in electrospun fiber meshes, concluding that application of both nanoparticles can reduce cytotoxicity without affecting the antibacterial efficacy of fiber meshes (23). It should be noted that the A549 cells are considered sensitive (24–26). Therefore, while the high sensitivity of these cells helped to determine the source of the cytotoxicity (ZnO NP), it might not be the actual representative of *in vivo* outcomes.

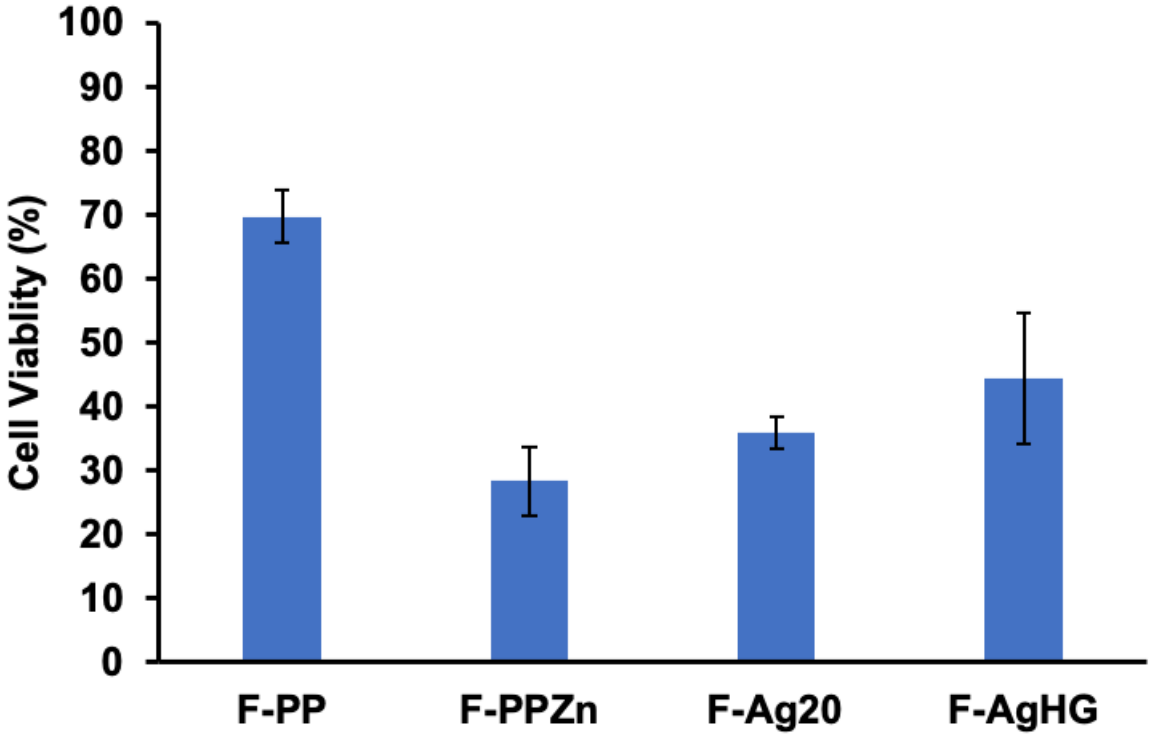

Figure 4.2 A549 lung epithelial cell viability in an *in vitro* 24 hours culture measured by MTS assay. Data are expressed as mean ± SE of n = 4.

Surgical implantation of fiber meshes

General appearance of the skin with surgical implants

The fiber meshes were appeared to have been well-tolerated by all animals. No sign of irritation or infection was observed at any of the time intervals. Fiber meshes had good adherence and did not move from the implantation site i.e. the left dorsal flank. However, fiber meshes were folded in some animals. When collecting tissue samples, fiber meshes were easily released from the adjacent tissues (skin or muscle) at 24-hour and 7-day time intervals. After 27 days of implantation, fiber meshes of all groups (excluding the F-PP group) were attached to the underlying muscle. Moreover, some capillary formation could be seen on the fiber meshes after 27 days of implantation. Images of the animals at 27 days after surgery are presented in Figure

4.3. Hair regrowth was faster for females compared to males in all groups. For all groups, hair regrowth initiated from the site of surgical incision i.e. the right dorsal flank. Fiber mesh F-PP, which had no ZnO NP or Ag NP, slightly decreased the hair regrowth in both male and female mice. Fiber mesh F-PPZn, which had ZnO NP, improved the hair regrowth in both males and females. However, addition of Ag NP into the composition of fiber mesh F-Ag20 decreased hair regrowth. These results are in contrast to a previous study (27), in which, addition of Ag NP into the electrospun fibers stimulated the hair regrowth of a rabbit model. Fiber meshes with PNIPAM microgel particles, F-AgHG, had a slightly better hair regrowth than F-Ag fiber meshes. This result is most likely be due to the less total percent of Ag NP in fiber meshes F-AgHG (0.01%) compared to F-Ag (0.02%).

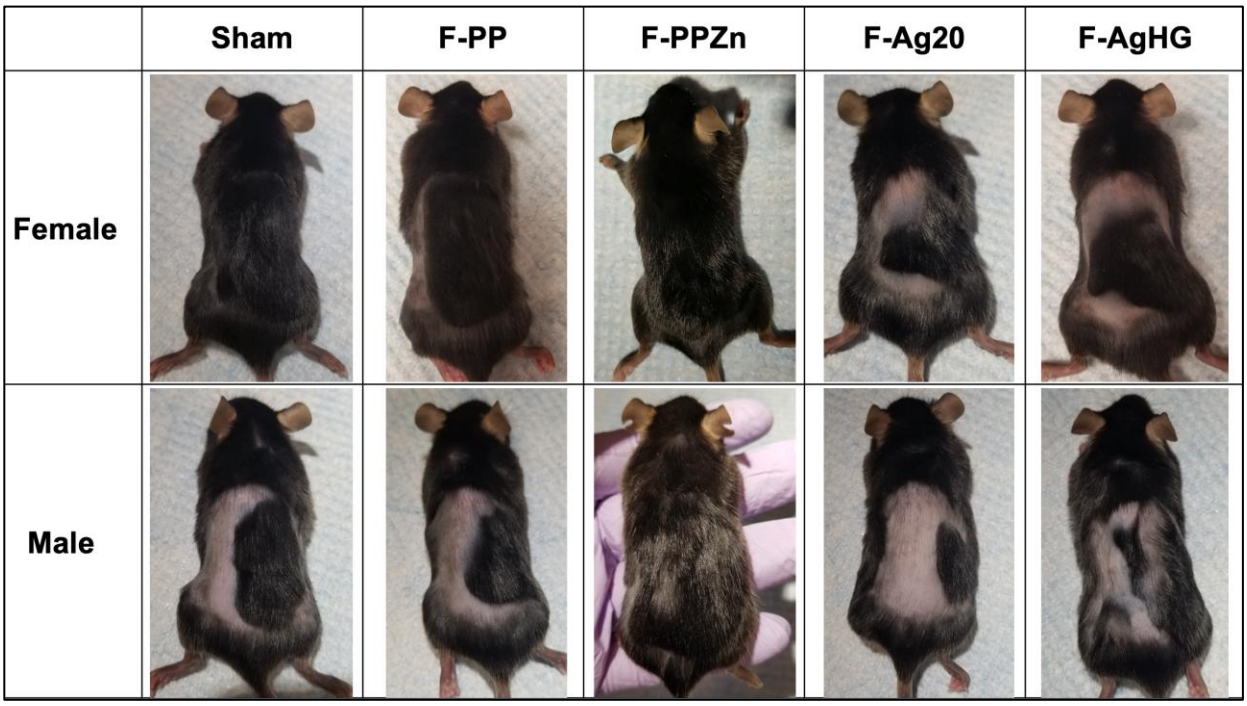

Figure 4.3 Skin appearance of the mouse groups on 27 days post-surgery.

Response of skin tissue to fiber implants

Skin samples collected after 24 hours, 7 days, and 27 days of implantation were stained and examined for responses to the different fiber implants. Representative examples are presented in Figure 4.4 for female mice and in Figure 4.5 for male mice. The normal skin (no surgery) examples show the different structure of female and male mice. Female skin has more adipose cells and more hair follicles (28,29). After 24 hours of implantation, edema was seen in all groups with an increasing order of F-PPZn, sham, F-PP, F-AgHG, and F-Ag20. These results show that addition of Ag NP induced edema while ZnO NP reduced the edema. Similar results were observed in female and male groups, but with greater intensity in female mice. After 24 hours of implantation, some accumulation of neutrophils on the fiber mesh F-PP was seen in male and female mice suggesting the presence of an infection or acute inflammation (30). After 7 days of implantation, neutrophil accumulation diminished. No edema was seen after 7 days in the male and female sham surgery groups and the skin structure was similar to normal skin. However, more hair follicles in female mice and less hair follicles in male mice were observed compared to normal skin. After 7 days of implantation, edema was reduced, but not completely eliminated, in all fiber mesh groups. After 7 days of implantation, some cell infiltration to the fiber meshes was detected starting from the edges of fiber mesh. The lowest cell infiltration was observed with F-PP. After 27 days of implantation, cell infiltration was greatest for F-Ag20 and F-AgHG and less F-PPZn. Cell infiltration did not increase for F-PP after 27 days of implantation. This result shows that Ag NP was responsible for inducing cell infiltration into the fiber meshes. Slight degree of fibrosis formed around the fiber meshes after 27 days which showed biocompatibility of the fiber meshes (31).

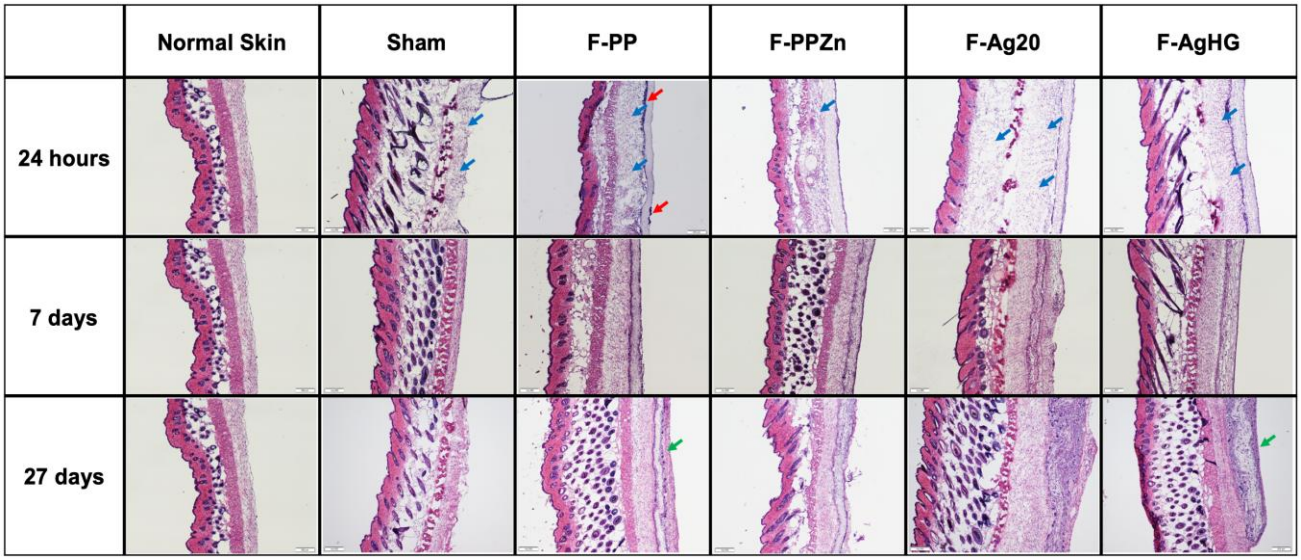

Figure 4.4 Bright field micrographs of H&E stained skin samples of female mice collected at 24-hour, 7-day, 27-days intervals compared to the normal skin. Blue, red, and green arrows denote edema, neutrophils, and fibrotic tissue, respectively. All images are at 40X and scale bars are 200 µm.

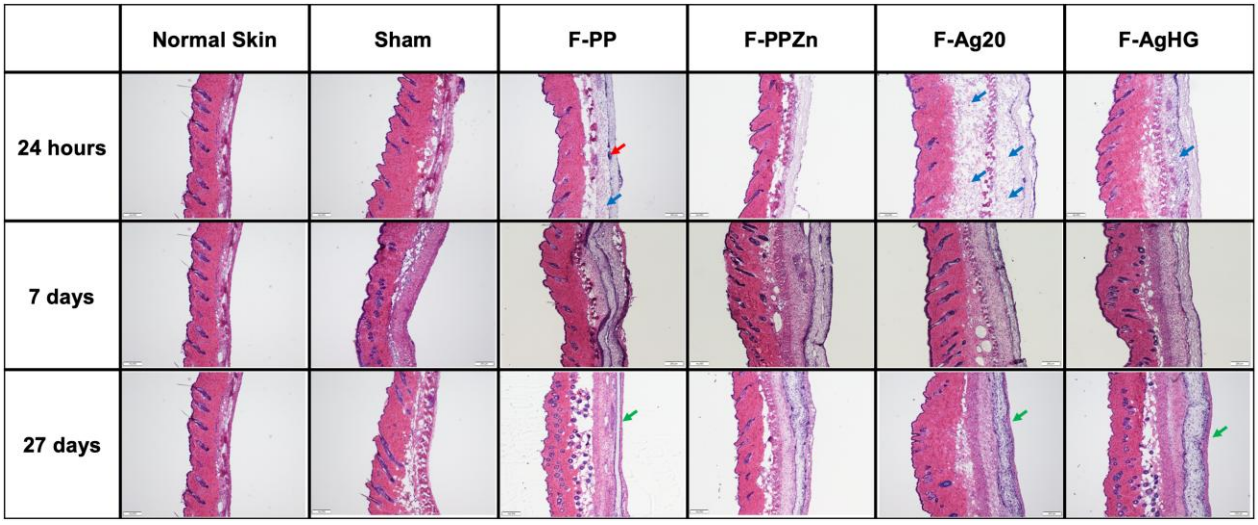

Figure 4.5 Bright field micrographs of H&E stained tissue samples of male mice collected at 24-hour, 7-day, 27-days intervals compared to the normal skin. Blue, red, and green arrows denote

edema, neutrophils, and fibrotic tissue, respectively. All images are at 40X and scale bars are 200 μm.

Hyperspectral mapping of Ag NP

Our earlier studies with the fiber meshes demonstrated that Ag NP were released from the fiber meshes into water (10,11). The antibacterial and cytotoxicity studies suggested that Ag NP were released into biologically relevant media and had toxicity toward bacteria and cells. The histology results suggested that Ag NP were released from the fiber meshes *in vivo*. CytoViva hyperspectral imaging of the tissue samples was performed to demonstrate that Ag NP were released from the fiber meshes. Figures 4.6, 4.7, and 4.8 present CytoViva hyperspectral imaging of the female mouse skin collected after 24 hours, 7 days, and 27 days of implantation, respectively. It can be seen in Figure 4.6 that after 24 hours of implantation, Ag NP were released from the mesh, traveled through the dermis, and accumulated at hair follicles. This result confirms release of Ag NP soon after implantation and ability of Ag NP to traverse from the meshes through several cell layers to the hair follicles. Figure 4.7 shows that the accumulation of Ag NP in hair follicles continued after 7 days of implantation. Figure 4.8 shows a high accumulation of Ag NP along the hair shafts after 27 days of implantation. This result confirms that Ag NP had a continuous release from fiber meshes over the period of 27 days which resulted in a uniform accumulation inside the hair shafts as hair grew.

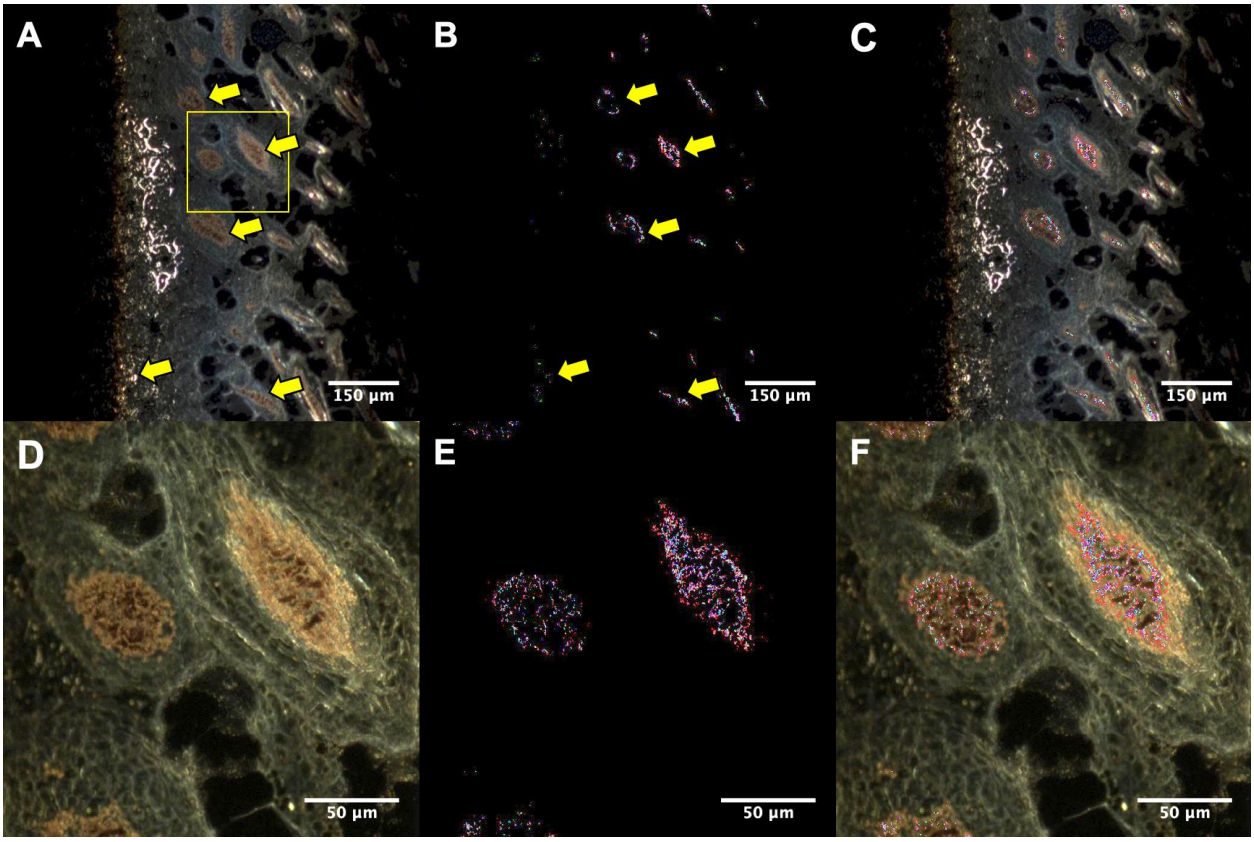

Figure 4.6 CytoViva hyperspectral imaging of the female mouse skin collected after 24 hours implantation of fiber mesh F-Ag20. Dark field images (A and D), spectral mapping of Ag NP (B and E), and the overlaid images (C and F). Images taken at 50X magnification (A, B, and C) and 400X magnification (D, E, and F). Yellow arrows denote accumulated Ag NP in hair follicles.

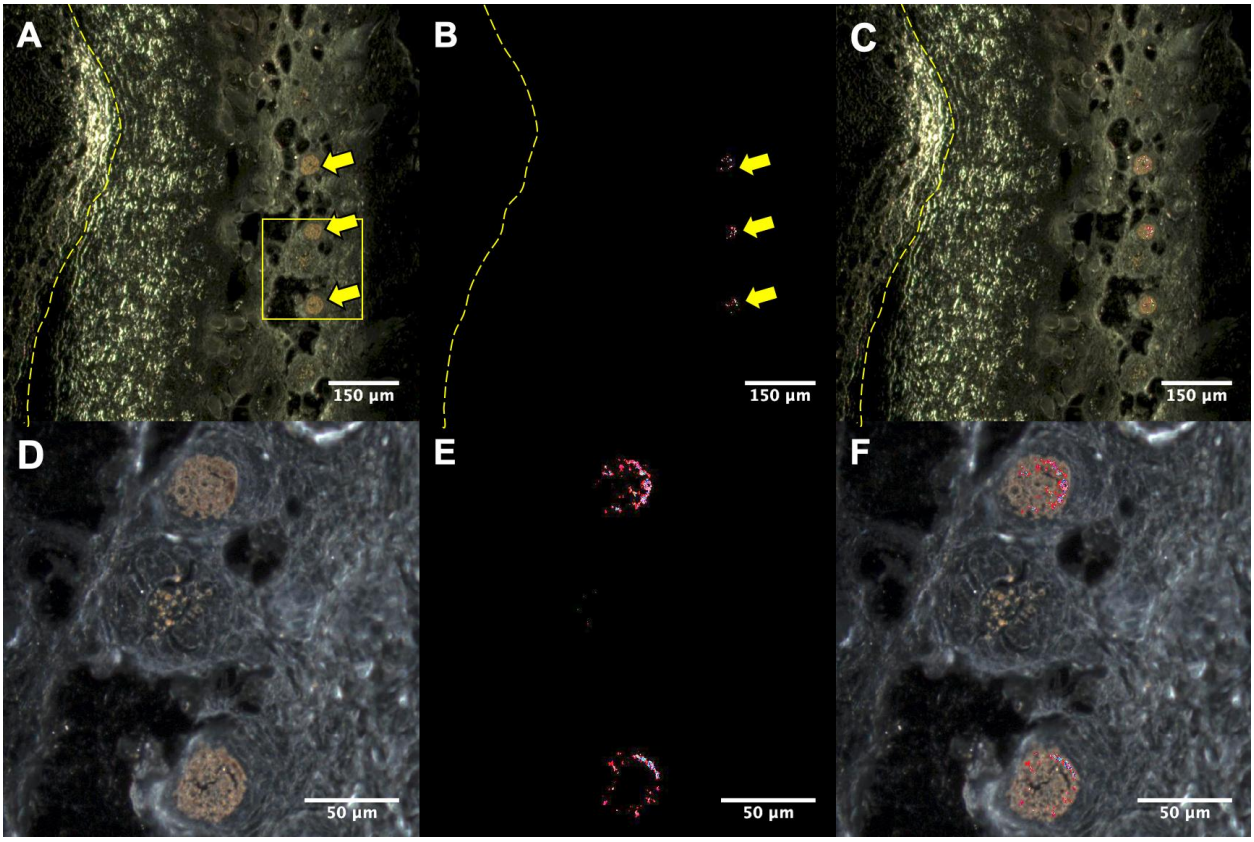

Figure 4.7 CytoViva hyperspectral imaging of female mouse skin collected after 7 days implantation of fiber mesh F-Ag20. Dark field images (A and D), spectral mapping of Ag NP (B and E), and overlaid images (C and F). Images taken at 100X magnification (A, B, and C) and 400X magnification (D, E, and F). The dashed lines show the tissue and fiber mesh margin. The rectangular shows the region of the image taken at 400X magnification. Yellow arrows denote accumulated Ag NP in hair follicles.

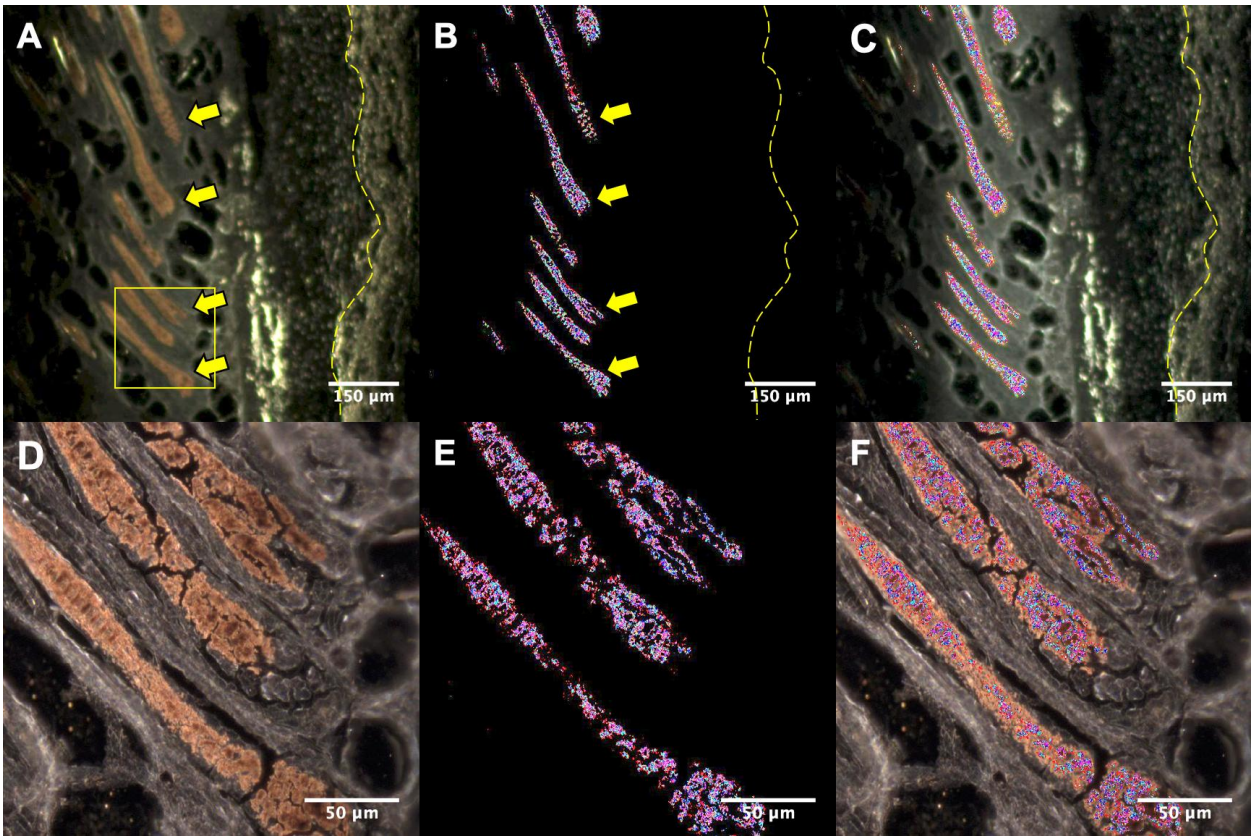

Figure 4.8 CytoViva hyperspectral imaging of female mouse skin collected after 27 days implantation of fiber mesh F-Ag20. Dark field images (A and D), spectral mapping of Ag NP (B and E), and overlaid micrographs (C and F). Images taken at 100X magnification (A, B, and C) and 400X magnification (D, E, and F). The dashed lines show the tissue and fiber mesh margin. Yellow arrows denote accumulated Ag NP in hair shafts.

Figures 4.9, 4.10, and 4.11 present CytoViva hyperspectral images of male mouse skin collected after 24 hours, 7 days, and 27 days of implantation, respectively. Figure 4.9 shows accumulation of Ag NP in a hair follicle after 24 hours of implantation, which confirmed the early release of Ag NP from the fiber mesh. However, skin samples of male mice had less hair follicles compared to female mice and thus it was difficult to detect many hair follicles with Ag NP accumulation. Figures 4.10 and 4.11 show that male skin samples had no hair follicles after 7

and 27 days of implantation, and Ag NP were dispersed within the dermis. This result confirms that Ag NP had a continuous release from the fiber mesh during the 27 days of implantation in male mice, however, the released Ag NP had different distribution/accumulation behavior compared to female mice. Similar results were observed for *in vivo* release of Ag NP from the fiber meshes containing PNIPAM microgel particles (Figures 4.12, 4.13, 4.14, 4.15, 4.16, and 4.17).

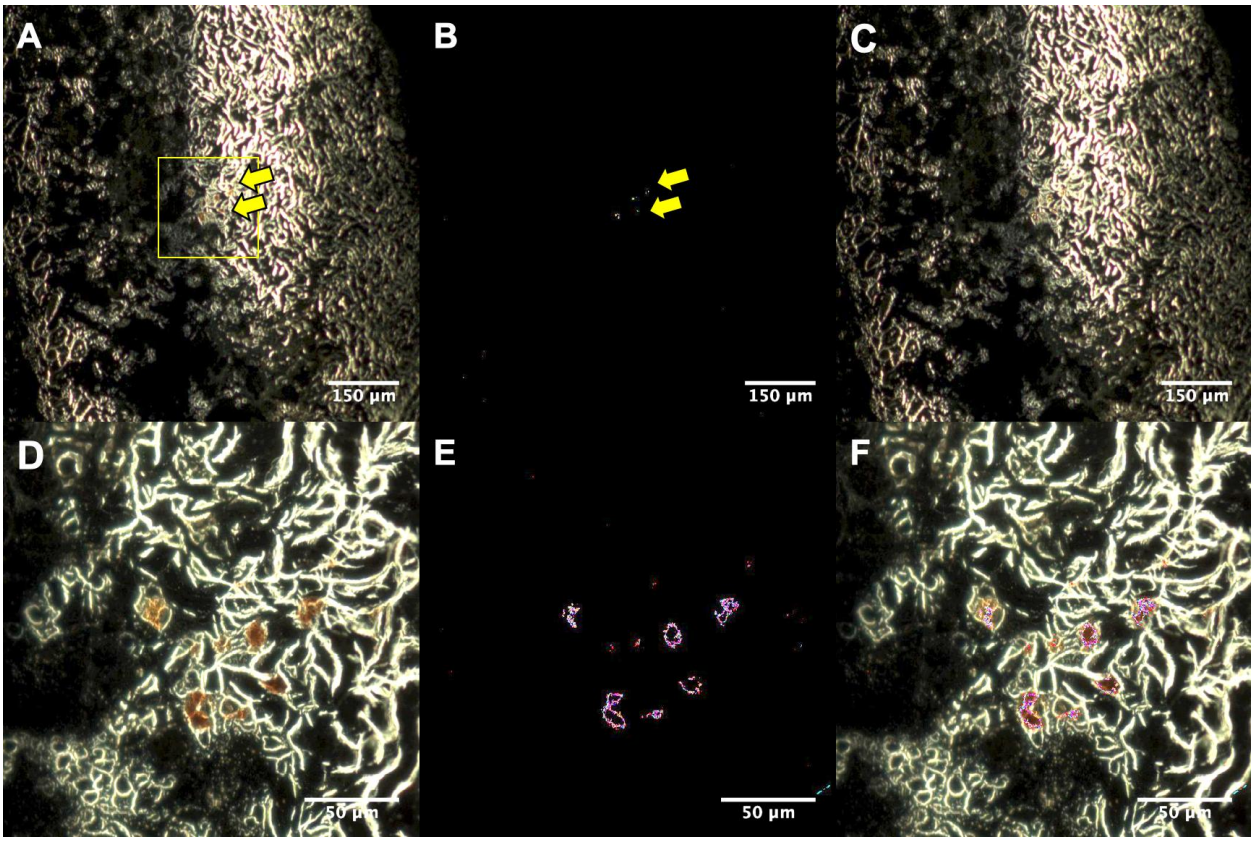

Figure 4.9 CytoViva hyperspectral imaging of male mouse skin collected after 24 hours implantation of fiber mesh F-Ag20. Dark field images (A and D), spectral mapping of Ag NP (B and E), and overlaid images (C and F). Images taken at 100X magnification (A, B, and C) and

400X magnification (D, E, and F). The rectangle shows the region of the image taken at 400X magnification. Yellow arrows denote accumulated Ag NP in the dermis.

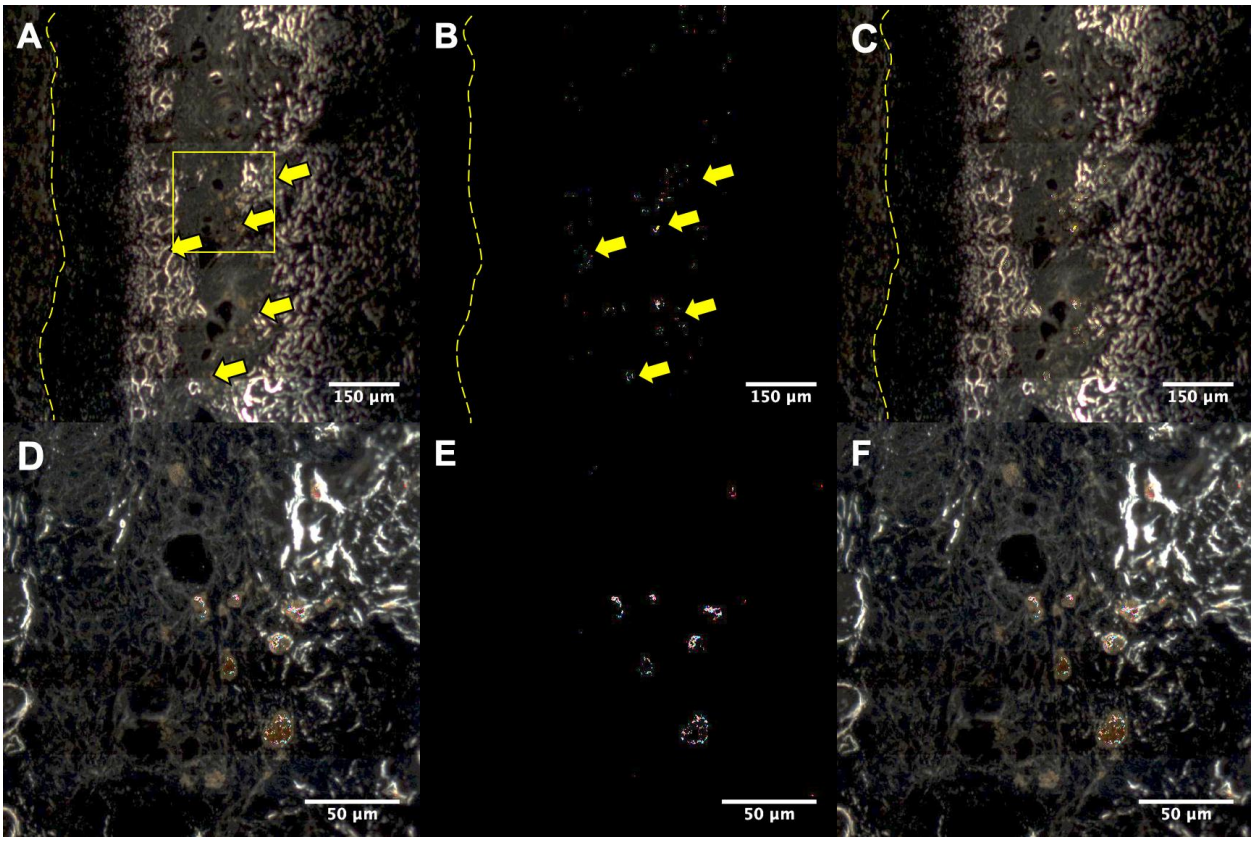

Figure 4.10 CytoViva hyperspectral imaging of male mouse skin collected after 7 days implantation of fiber mesh F-Ag20. Dark field images (A and D), spectral mapping of Ag NP (B and E), and overlaid images (C and F). Images taken at 100X magnification (A, B, and C) and 400X magnification (D, E, and F). The dashed lines show the tissue and fiber mesh margin. The rectangle shows the region of the image taken at 400X magnification. Yellow arrows denote dispersed Ag NP in the dermis.

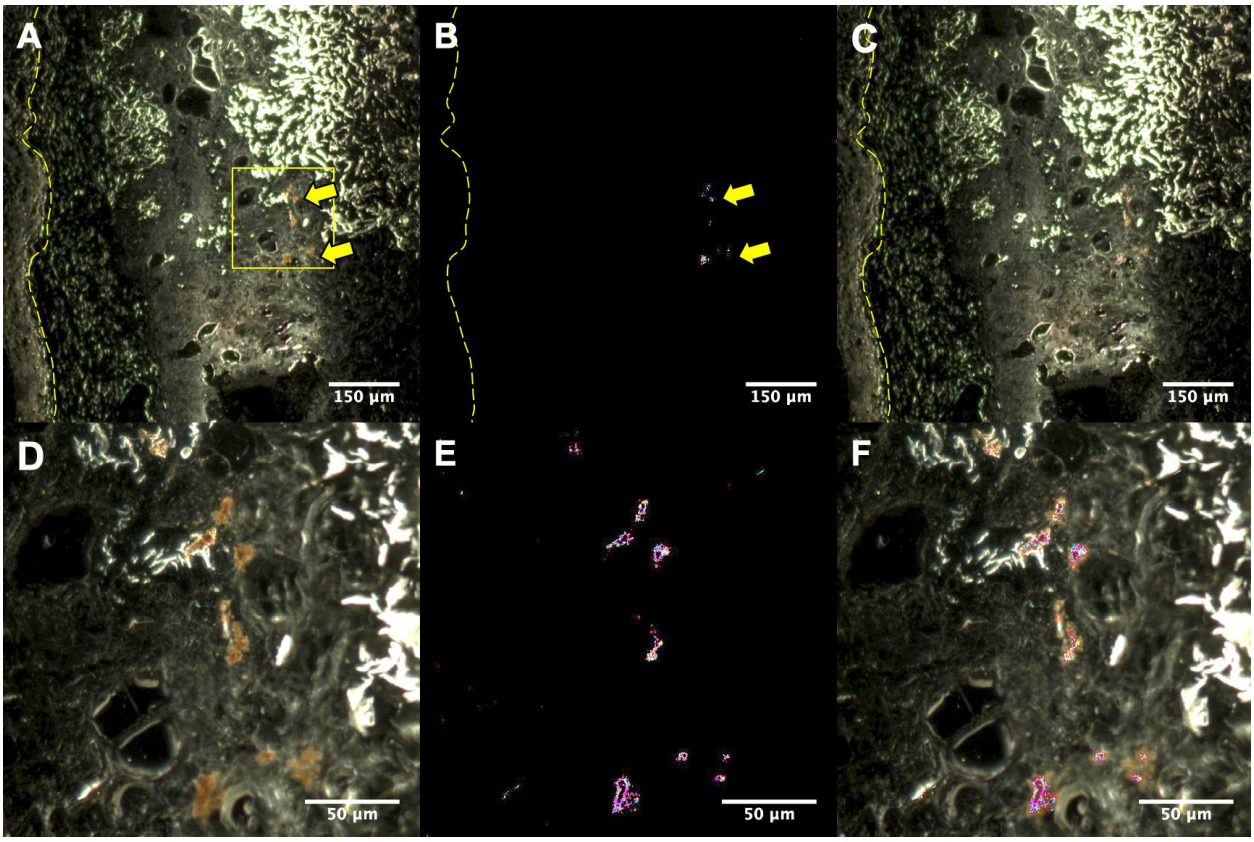

Figure 4.11 CytoViva hyperspectral imaging of male mouse skin collected after 27 days implantation of fiber mesh F-Ag20. Dark field images (A and D), spectral mapping of Ag NP (B and E), and overlaid images (C and F). Images taken at 100X magnification (A, B, and C) and 400X magnification (D, E, and F). The dashed lines show the tissue and fiber mesh margin. The rectangle shows the region of the image taken at 400X magnification. Yellow arrows denote dispersed Ag NP in the dermis.

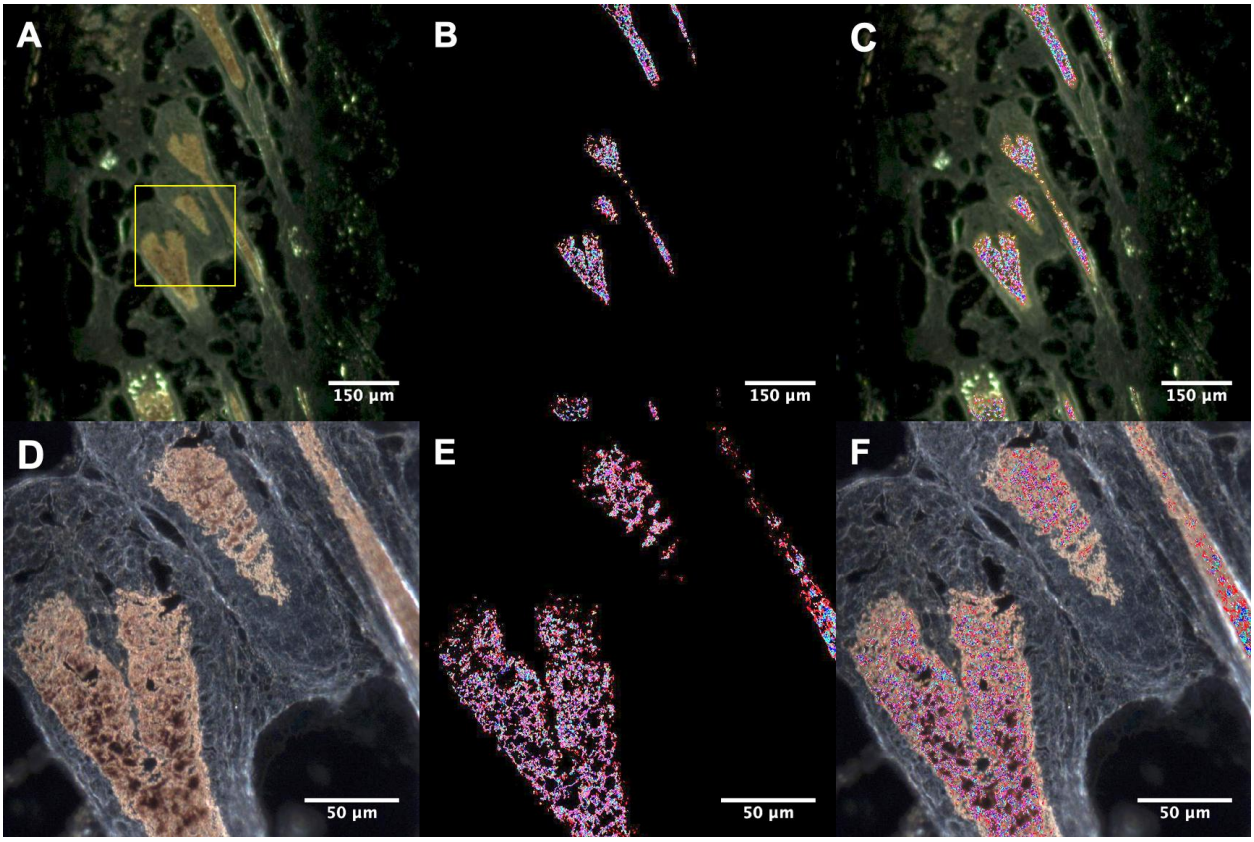

Figure 4.12 CytoViva hyperspectral imaging of the female mouse skin collected after 24 hours implantation of fiber mesh F-AgHG. Dark field images (A and D), spectral mapping of Ag NP (B and E), and the overlaid images (C and F). Images taken at 50X magnification (A, B, and C) and 400X magnification (D, E, and F). Yellow arrows denote accumulated Ag NP in hair follicles.

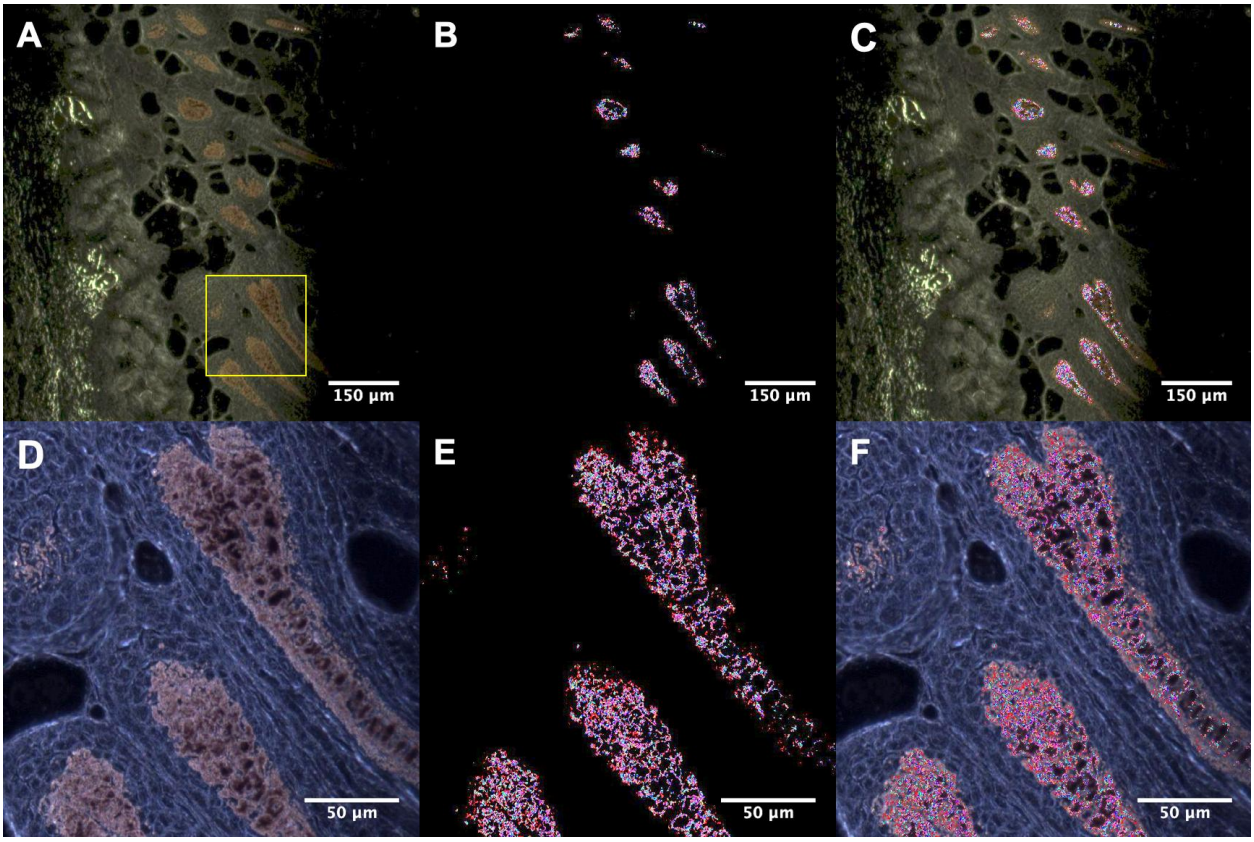

Figure 4.13 CytoViva hyperspectral imaging of the female mouse skin collected after 7 days implantation of fiber mesh F-AgHG. Dark field images (A and D), spectral mapping of Ag NP (B and E), and the overlaid images (C and F). Images taken at 50X magnification (A, B, and C) and 400X magnification (D, E, and F). Yellow arrows denote accumulated Ag NP in hair follicles.

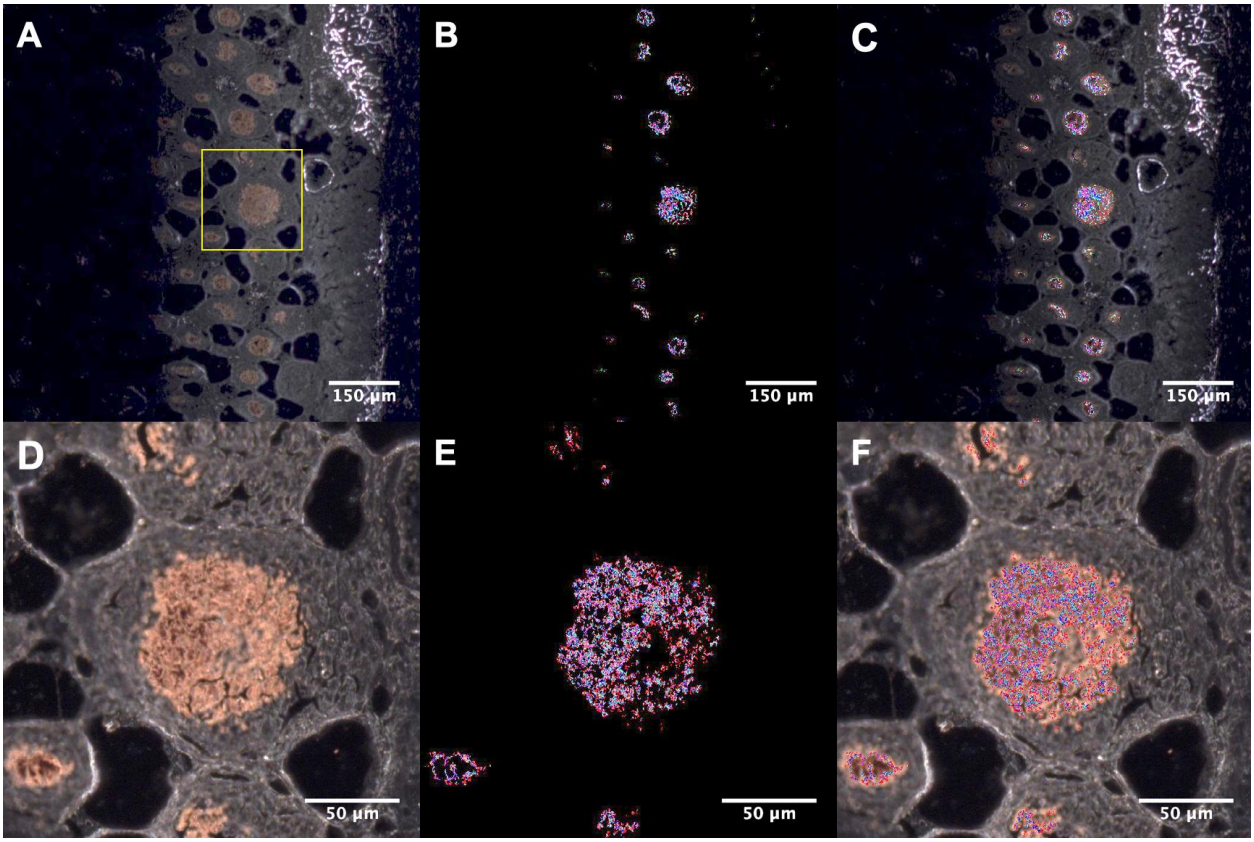

Figure 4.14 CytoViva hyperspectral imaging of the female mouse skin collected after 27 days implantation of fiber mesh F-AgHG. Dark field images (A and D), spectral mapping of Ag NP (B and E), and the overlaid images (C and F). Images taken at 50X magnification (A, B, and C) and 400X magnification (D, E, and F). Yellow arrows denote accumulated Ag NP in hair follicles.

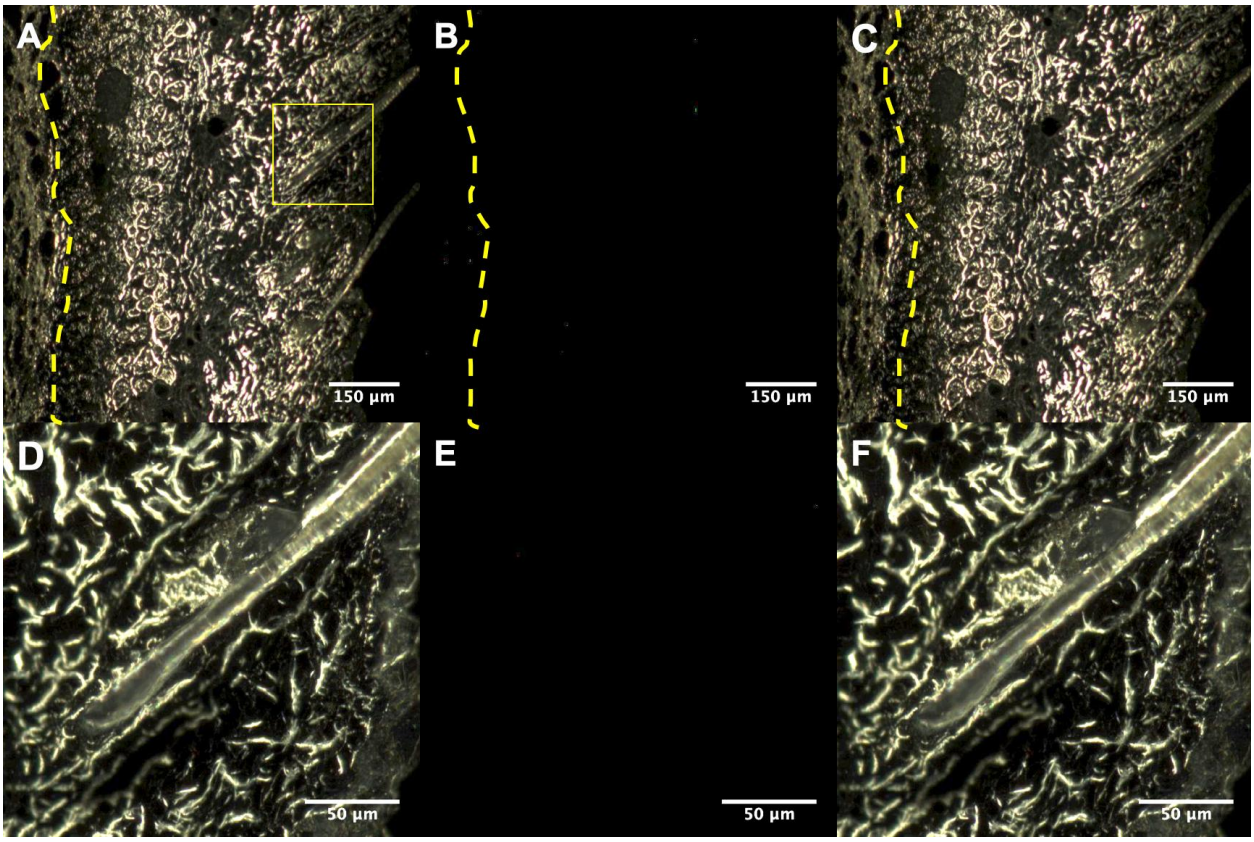

Figure 4.15 CytoViva hyperspectral imaging of male mouse skin collected after 24 hours implantation of fiber mesh F-AgHG. Dark field images (A and D), spectral mapping of Ag NP (B and E), and overlaid images (C and F). Images taken at 100X magnification (A, B, and C) and 400X magnification (D, E, and F). The dashed lines show the tissue and fiber mesh margin. The rectangle shows the region of the image taken at 400X magnification. Yellow arrows denote dispersed Ag NP in the dermis.

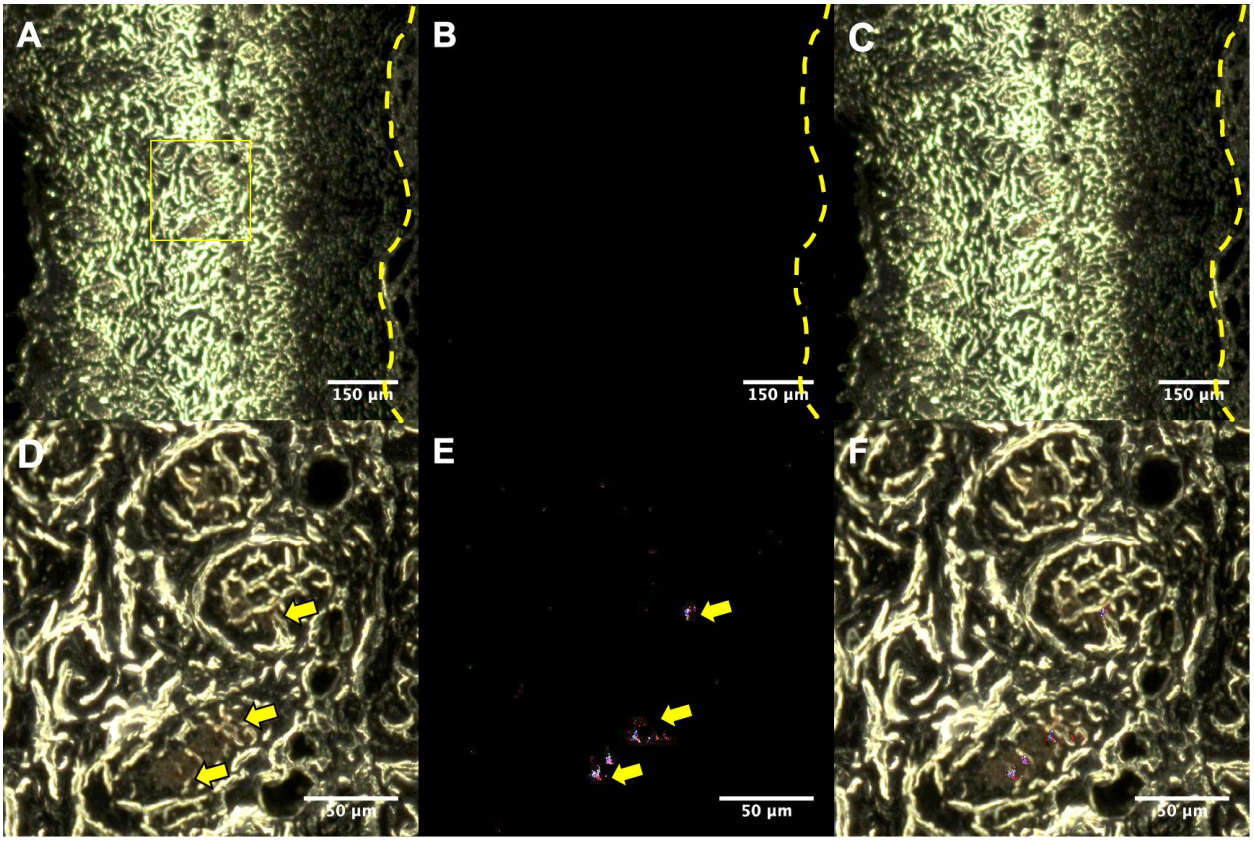

Figure 4.16 CytoViva hyperspectral imaging of male mouse skin collected after 7 days implantation of fiber mesh F-AgHG. Dark field images (A and D), spectral mapping of Ag NP (B and E), and overlaid images (C and F). Images taken at 100X magnification (A, B, and C) and 400X magnification (D, E, and F). The dashed lines show the tissue and fiber mesh margin. The rectangle shows the region of the image taken at 400X magnification. Yellow arrows denote dispersed Ag NP in the dermis.

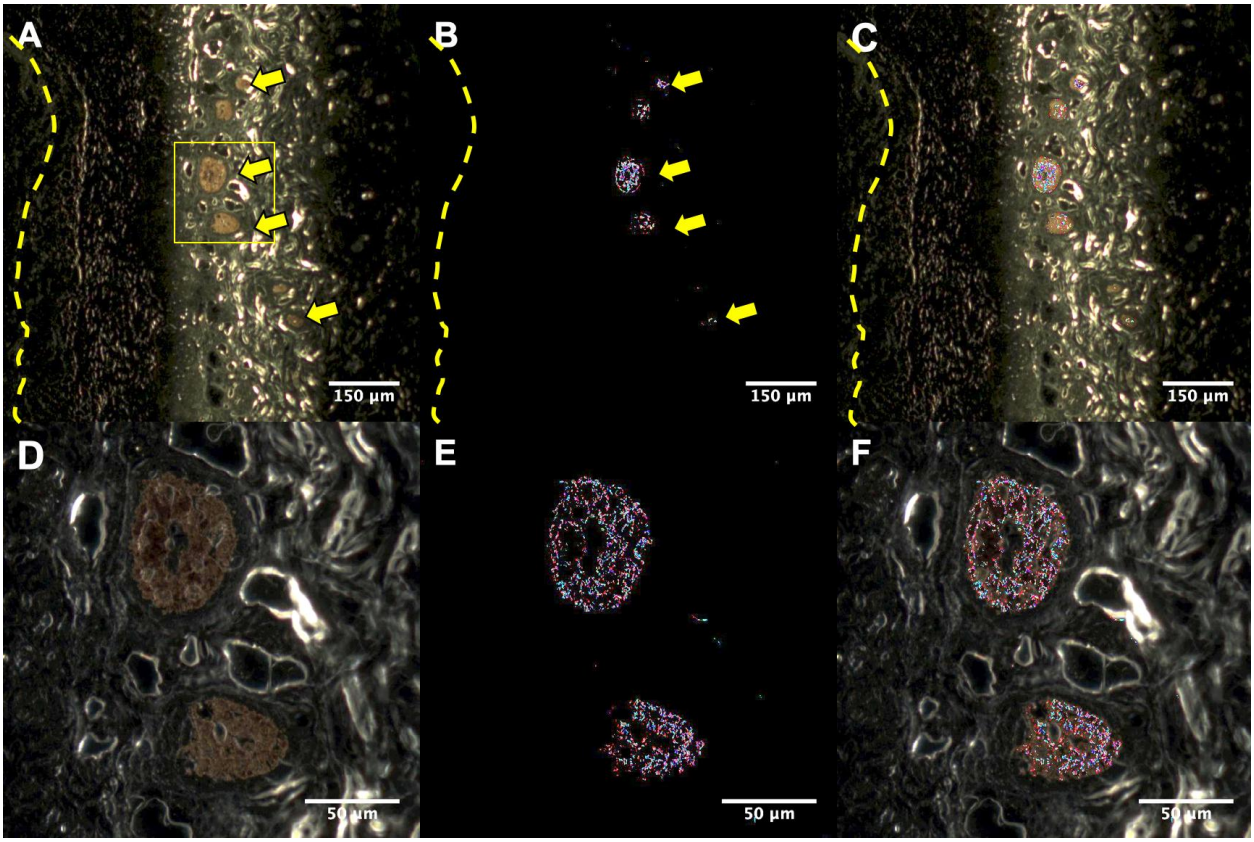

Figure 4.17 CytoViva hyperspectral imaging of male mouse skin collected after 27 days implantation of fiber mesh F-AgHG. Dark field images (A and D), spectral mapping of Ag NP (B and E), and overlaid images (C and F). Images taken at 100X magnification (A, B, and C) and 400X magnification (D, E, and F). The dashed lines show the tissue and fiber mesh margin. The rectangle shows the region of the image taken at 400X magnification. Yellow arrows denote dispersed Ag NP in the dermis.

Conclusions

In vitro and *in vivo* evaluations of the fiber meshes were performed in this study. *In vitro* antibacterial activity of fiber meshes was shown and thus confirmed the potential for antibacterial applications such as wound dressings. MTS assay results showed cytotoxicity of the ZnO NP suggesting that the fiber meshes might not be appropriate for *in vitro* tissue scaffolding

uses. In future studies, other nanoparticles can be explored for replacing ZnO NP to reduce cytotoxicity.

Subcutaneous implantation of fiber meshes allowed monitoring of drug delivery into skin tissue. The Ag NP started to release soon after implantation and continued to release over the course of 27 days. In male mice, Ag NP were dispersed in the dermis layer while in female mice, Ag NP accumulated in hair follicles. Different accumulation patterns of Ag NP in male and female mice suggest the need to consider gender-specific drug delivery systems. Quantitative measurements of drug release rates are needed to further understand the gender difference of drug release. Ag NP reduced hair regrowth which was in contrast to previous reports (27,32,33). More studies are needed to understand the mechanism(s) of Ag NP effects on hair growth. ZnO NP enhanced wound healing and stimulated hair regrowth. These results suggested the use of the fiber meshes for cosmetic applications. *In vivo* studies confirmed drug release, biocompatibility, and mechanical stability of the fiber meshes and effective performance for prolonged drug delivery applications.

References

1. Torres-Martinez EJ, Cornejo Bravo JM, Serrano Medina A, Pérez González GL, Villarreal Gómez LJ. A Summary of Electrospun Nanofibers as Drug Delivery System: Drugs Loaded and Biopolymers Used as Matrices. Curr Drug Deliv. 2018 Jul 23;15(10):1360–74.

2. Yu D-G, Zhu L-M, White K, Branford-White C. Electrospun nanofiber-based drug delivery systems. 2009;1(2):67–75.

3. Poláková L, Širc J, Hobzová R, Cocârță AI, Heřmánková E. Electrospun nanofibers for

local anticancer therapy: Review of in vivo activity. Vol. 558, International Journal of Pharmaceutics. Elsevier B.V.; 2019. p. 268–83.

4. Karimi M, Sahandi Zangabad P, Ghasemi A, Amiri M, Bahrami M, Malekzad H, et al. Temperature-Responsive Smart Nanocarriers for Delivery of Therapeutic Agents: Applications and Recent Advances. Vol. 8, ACS Applied Materials and Interfaces. 2016. p. 21107–33.

5. Dokoumetzidis A1 MP. A century of dissolution research From Noyes and Whitney to the.pdf. Int J Pharm. 2006;321:16920290.

6. Dissolution. United State Pharmacopeia (USP). USP 34-NF 29 ed2011. P. 5091-7.

7. Shen J, Burgess DJ. In vitro dissolution testing strategies for nanoparticulate drug delivery systems: Recent developments and challenges. Vol. 3, Drug Delivery and Translational Research. 2013. p. 409–15.

8. Solomon D, Gupta N, Mulla NS, Shukla S, Guerrero YA, Gupta V. Role of In Vitro Release Methods in Liposomal Formulation Development: Challenges and Regulatory Perspective. Vol. 19, AAPS Journal. Springer New York LLC; 2017. p. 1669–81.

9. Godin B, Touitou E. Transdermal skin delivery: Predictions for humans from in vivo, ex vivo and animal models. Vol. 59, Advanced Drug Delivery Reviews. Elsevier; 2007. p. 1152–61.

10. Mahdieh Z, Holian A. No Title. Electrospun fibers loaded with ball-milled hydrogel Part smart Deliv Appl.

11. Mahdieh Z, Mitra S, Holian A. Electrospun fibers with an improved pore structure for controlled delivery of nanoparticles. ACS Appl Mater Interfaces. 2020;(am-2020-04409t).

12. Falde EJ, Freedman JD, Herrera VLM, Yohe ST, Colson YL, Grinstaff MW. Layered superhydrophobic meshes for controlled drug release. J Control Release. 2015 Jul 25;214:23–9.

13. Kurpinski KT, Stephenson JT, Janairo RRR, Lee H, Li S. The effect of fiber alignment and heparin coating on cell infiltration into nanofibrous PLLA scaffolds. Biomaterials. 2010 May 1;31(13):3536–42.

14. Rujitanaroj PO, Aid-Launais R, Chew SY, Le Visage C. Polysaccharide electrospun fibers with sulfated poly(fucose) promote endothelial cell migration and VEGF-mediated angiogenesis. Biomater Sci. 2014 May 7;2(6):843–52.

15. Srouji S, Kizhner T, Suss-Tobi E, Livne E, Zussman E. 3-D Nanofibrous electrospun multilayered construct is an alternative ECM mimicking scaffold. J Mater Sci Mater Med. 2008 Mar 15;19(3):1249–55.

16. Guo H-F, Li Z-S, Dong S-W, Chen W-J, Deng L, Wang Y-F, et al. Piezoelectric PU/PVDF electrospun scaffolds for wound healing applications. Colloids Surfaces B Biointerfaces. 2012;96:29–36.

17. Augustine R, Dominic EA, Reju I, Kaimal B, Kalarikkal N, Thomas S. Electrospun polycaprolactone membranes incorporated with ZnO nanoparticles as skin substitutes with enhanced fibroblast proliferation and wound healing. RSC Adv. 2014 Jun 9;4(47):24777–85.

18. Balouiri M, Sadiki M, Ibnsouda SK. Methods for in vitro evaluating antimicrobial activity: A review. Vol. 6, Journal of Pharmaceutical Analysis. Xi'an Jiaotong University; 2016. p. 71–9.

19. Hamilton RF, Wu Z, Mitra S, Holian A. The effects of varying degree of MWCNT carboxylation on bioactivity in various in vivo and in vitro exposure models. Int J Mol Sci. 2018 Feb 1;19(2).

20. Gao Y, Bach Truong Y, Zhu Y, Louis Kyratzis I. Electrospun antibacterial nanofibers: Production, activity, and in vivo applications. J Appl Polym Sci. 2014 Sep 15;131(18):n/a-n/a.

21. Yang ST, Liu JH, Wang J, Yuan Y, Cao A, Wang H, et al. Cytotoxicity of zinc oxide nanoparticles: Importance of microenvironment. In: Journal of Nanoscience and Nanotechnology. 2010. p. 8638–45.

22. Ng CT, Yong LQ, Hande MP, Ong CN, Yu LE, Bay BH, et al. Zinc oxide nanoparticles exhibit cytotoxicity and genotoxicity through oxidative stress responses in human lung fibroblasts and Drosophila melanogaster. Int J Nanomedicine. 2017 Feb 28;12:1621–37.

23. Hu M, Li C, Li X, Zhou M, Sun J, Sheng F, et al. Zinc oxide/silver bimetallic nanoencapsulated in PVP/PCL nanofibres for improved antibacterial activity. Artif Cells, Nanomedicine Biotechnol. 2018 Aug 18;46(6):1248–57.

24. Alhadlaq HA, Akhtar MJ, Ahamed M. Zinc ferrite nanoparticle-induced cytotoxicity and oxidative stress in different human cells. Cell Biosci. 2015 Sep 17;5(1):55.

25. Hsiao IL, Huang YJ. Effects of various physicochemical characteristics on the toxicities of ZnO and TiO2 nanoparticles toward human lung epithelial cells. Sci Total Environ. 2011 Mar 1;409(7):1219–28.

26. Lankoff A, Sandberg WJ, Wegierek-Ciuk A, Lisowska H, Refsnes M, Sartowska B, et al. The effect of agglomeration state of silver and titanium dioxide nanoparticles on cellular

response of HepG2, A549 and THP-1 cells. Toxicol Lett. 2012 Feb 5;208(3):197–213.

27. Tura V, Hagiu BA, Mangalagiu II. Hair follicles stimulation effects of gelatin nanofibers containing silver nanoparticles. J Biomed Nanotechnol. 2010 Apr;6(2):192–7.

28. Azzi L, El-Alfy M, Martel C, Labrie F. Gender differences in mouse skin morphology and specific effects of sex steroids and dehydroepiandrosterone. J Invest Dermatol. 2005 Jan 1;124(1):22–7.

29. Rønø B, Engelholm LH, Lund LR, Hald A. Gender Affects Skin Wound Healing in Plasminogen Deficient Mice. PLoS One. 2013 Mar 20;8(3).

30. Zhou J, Tsai YT, Weng H, Tang EN, Nair A, Davé DP, et al. Real-time detection of implant-associated neutrophil responses using a formyl peptide receptor-targeting NIR nanoprobe. Int J Nanomedicine. 2012;7:2057–68.

31. Xue J, He M, Liang Y, Crawford A, Coates P, Chen D, et al. Fabrication and evaluation of electrospun PCL-gelatin micro-/nanofiber membranes for anti-infective GTR implants. J Mater Chem B. 2014 Oct 21;2(39):6867–77.

32. Kirkpatrick CM. Hair growth promoter and method of using same. 1998 Apr.

33. Keeney JA. Compositions for stimulating hair growth, preventing hair loss, or minimizing hair loss, and methods for preparing and using same. 1999 Jul.

Supplementary data of chapter 4

Table 1. The Holm-Sidak's multiple comparisons test results for the OD_{600} measurements of the antibacterial assay reported in Figure 4.1. Asterisks indicate significant difference ****p < 0.0001, ***p < 0.0002, **p < 0.0021, *p < 0.0332, ^{ns}P > 0.1234.

	Control vs. F-PP, F-AgHG vs. F-PPZn, F-AgHG vs. F-Ag20, F-PPZn vs. F-Ag20	Control vs. HG-200µL	Control vs. F-AgHG, F-PP vs. F-Ag20	Control vs. F-PPZn, Control vs. F-Ag20, HG-200µL vs. F-AgHG, HG-200µL vs. F-PPZn, HG-200µL vs. F-Ag20	F-PP vs. F-AgHG, F-PP vs. F-PPZn	HG-200µL vs. F-PP
1h	ns	ns	ns	ns	ns	ns
2h	ns	ns	***	****	**	ns
3h	ns	ns	****	****	****	ns
4h	ns	ns	****	****	****	ns
5h	ns	ns	****	****	****	ns
6h	ns	ns	****	****	****	ns
7h	ns	ns	****	****	****	ns
8h	ns	ns	****	****	****	ns
9h	ns	ns	****	****	****	ns
10h	ns	ns	****	****	****	*
24h	ns	**	****	****	****	***

Table 2. The Holm-Sidak's multiple comparisons test results for A549 lung epithelial cell viability results reported in Figure 4.2. Asterisks indicate significant difference ****$p < 0.0001$, ***$p < 0.0002$, **$p < 0.0021$, *$p < 0.0332$, $^{ns}P > 0.1234$.

F-PP vs. F-PPZn	**
F-PP vs. F-Ag20	*
F-PP vs. F-AgHG	ns
F-PPZn vs. F-Ag20	ns
F-PPZn vs. F-AgHG	ns
F-Ag20 vs. F-AgHG	ns

Chapter 5: Conclusions and Future Directions

Contributions

Zahra Mahdieh, University of Montana: Primary author.

Andrij Holian, University of Montana: Supervisor. Reviewed the final submission.

Summary

The goal of this study was to develop electrospun fibers with 1) prolonged and controlled drug release, 2) suitable mechanical properties, 3) minimal toxicity, 4) and capable of loading fragile drugs or bioactive agents. The primary aim while developing the fiber design was to establish versatility that could be used in various applications. Figure 5.1 shows the designing steps of the developed fibers.

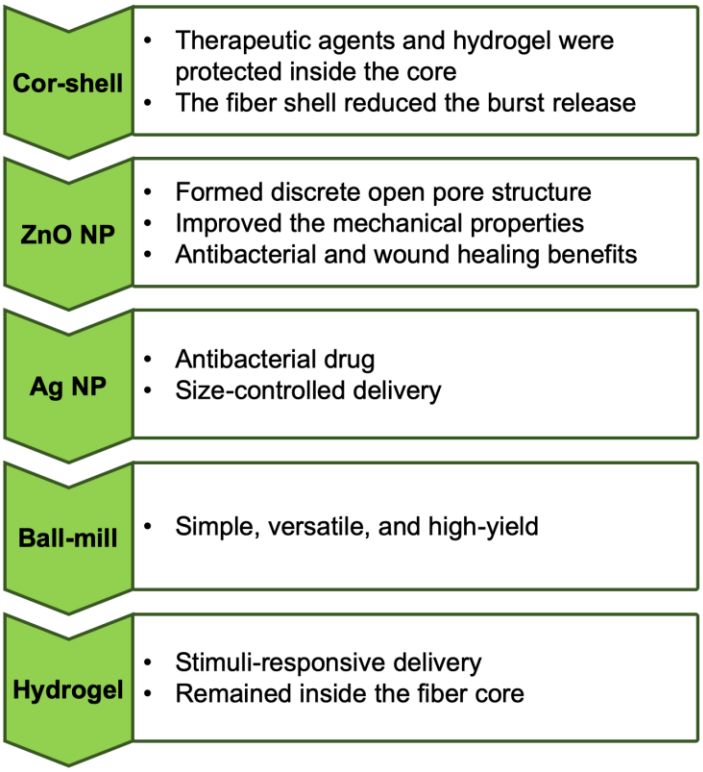

Figure 5.1 Development steps of the core-shell structured fibers.

Core-shell structure fibers were developed with silver nanoparticles (Ag NP, as a model drug) loaded inside the core. Formation of the core-shell structure was confirmed using transmission electron microscopy and confocal laser microscopy (fluorescent imaging). Fiber

diameter had a distribution with the highest frequency (mode) at 600-800 nm. The release pathway for Ag NP was defined through the pores formed in the shell via selective dissolution of the polyethylene glycol (PEG) as porogen. PEG has been used as a porogen for making pores in previous studies (1–4). However, in those studies, high percentages of PEG in the shell composition were needed to form open pores and thus the dissolution of PEG resulted in fiber rupture/swelling and failure of the shell structure. The sudden collapse of fibers in turn resulted in an uncontrolled and sudden release of the drug within one to a few hours (5,6). Therefore, open discrete pore structure and mechanical stability were recognized as the two essential factors to eliminate burst release and provide a prolonged release rate. Therefore, in my studies, I obtained a modified pore structure using a a small percentage of ZnO NP (1.6%) added to the shell simultaneously with the use of PEG (7%) as the porogen. Scanning electron microscopy (SEM) showed that addition of ZnO NP increased the depth and size of pores while tensile testing showed that mechanical properties improved. SEM imaging showed the formation of mostly oblong pores in the surface of the fibers. The average pore width (perpendicular to the fiber length) and length (parallel to the fiber length) were 70 ± 57 nm and 127 ± 64 nm, respectively.

Subsequently, fine-tuned delivery rates were achieved via loading 20 nm Ag NP, 110 nm Ag NP, or a mixture of the two sizes inside the fiber core. *In vitro* drug release studies showed fast (79%), slow (36%), and intermediate (62%) delivery rates of these Ag NP during two-weeks of immersion. Faster diffusion of smaller nanoparticles through the pores resulted in a faster release/delivery rate along with slower diffusion of larger nanoparticles resulting in a slower release/delivery rate.

The function of fibers was further enhanced to smart delivery of therapeutic agents by loading poly(n-isopropylacrylamide) (PNIPAM) microgel particles (in addition to Ag NP) inside the fiber core. Formation of the core-shell structure was confirmed using fluorescent imaging. SEM imaging showed that the highest fiber diameter frequency (mode) was at 400-600 nm. *In vitro* drug release studies showed a temperature-responsive drug delivery of fiber meshes. During two-weeks of immersion, Ag NP released 2.8-fold faster above the transition temperature of PNIPAM microgel (94%) compared to below the transition temperature (34%).

Ball-milling was developed as a simple, non-toxic, and high-yield method to produce PNIPAM microgel particles. Differential scanning calorimetry (DSC) analyses confirmed that the PNIPAM microgel particles maintained thermoresponsive behavior after the drying and ball milling processes. Dynamic light scattering (DLS) measurements showed that the average hydrodynamic diameter of PNIPAM microgel particles was 511 ± 100 nm below the transition temperature and 199 ± 10 nm above the transition temperature. Spectrophotometric analyses of the *in vitro* drug release water samples confirmed that more than 94.7% of the loaded PNIPAM microgel particles remained associated inside the fiber core.

In vitro and *in vivo* performances of the fiber meshes were evaluated in the final steps of this study. *In vitro* tests showed the antibacterial efficacy of the fiber meshes. Fiber meshes had a prompt growth inhibition effect when exposed to bacteria and effectively eliminated bacterial after 24 hours of incubation. *In vitro* MTS assays using human epithelial cells showed that cytotoxicity of the fiber meshes occurred and was caused by ZnO NP. The application of Ag NP reduced cytotoxicity, but not significantly.

Subcutaneous implantation of the fiber meshes in a mouse model was performed to investigate the *in vivo* drug delivery performance of the fiber meshes for applications such as

tissue engineering, wound dressings, and cancer treatment. Ag NP were released soon after implantation and continued to release over the course of 27 days. However, evaluation of skin showed different accumulation patterns of the released Ag NP in female and male mice. In female mice, the Ag NP accumulated in the hair follicles and were expelled into the hair shaft as it grew. However, Ag NP dispersed within the dermis in male mice. Ag NP induced edema during 24 hours of implantation and reduced hair regrowth during 27 days of implantation. ZnO NP induced less edema during 24 hours of implantation and enhanced the hair regrowth and wound healing during 27 days of implantation. Fiber meshes had appropriate biocompatibility and no infection was detected. The mechanical stability of fiber meshes was maintained after 27 days of implantation. *In vivo* drug release studies confirmed the potential of the fiber meshes for prolonged drug delivery applications.

Conclusions and future directions

The main advantage of the fiber meshes was versatility for applying different kinds of drugs or nanoparticles to be used for various applications. Bioactive or fragile therapeutic agents can be loaded inside the fiber core while being protected from organic solvents and harsh conditions of electrospinning. Drugs can be produced in the form of nanoparticles or can be loaded on nanoparticles. Simultaneous delivery of several drugs with individually controlled delivery rates can be achieved by loading different sizes of drug nanoparticles.

Future work needs to be performed for to explain the mechanism(s) to account for how ZnO NP improved the pore structure and mechanical properties, and the fluid dynamic inside the fiber core.

PNIPAM microgel can be replaced by other stimuli-responsive microgels to achieve different smart delivery systems. The advantage of using the stimuli-responsive polymers in the

form of microgel (i.e. cross-linked) is avoiding the sudden release into the tissue site and thus preventing/reducing possible toxicity. Loading microgel particles inside the core prevents undesired phase transition of stimuli-responsive microgels caused by electrospinning conditions and solvents.

The ball-milling method that was developed in this research allows for producing various microgel particles with specific properties while avoiding the chemical complexities of synthesizing microgels. Microgel particles can be filtered to achieve a narrow particle size distribution. Future work needs to be performed to determine a possible connection between the hydrogel synthesis method and the final shape and size distribution of the microgel particles.

The fiber meshes can be used for prolonged anti-infection applications such as wound dressings and tissue replacements. However, they are not suitable for *in vitro* tissue engineering applications due to the cytotoxicity of ZnO NP. In future work, other nanoparticles should be explored to replace the ZnO NP for reducing the cytotoxicity. Unlike the *in vitro* results, the *in vivo* implantation showed the benefits of ZnO NP to enhance wound healing and hair regrowth. Therefore, the application of ZnO NP had various advantages including forming open pores, improving mechanical properties, antibacterial properties, and wound healing enhancement. Moreover, the enhanced hair regrowth suggests potential cosmetic applications of ZnO NP. The different accumulation patterns of Ag NP in male and female mice suggests the need for gender-specific drug delivery designs. In future work, quantitative measurements of *in vivo* release rates and examination of other organs that Ag NP might traverse to (such as lymph nodes), in male and female mice, should be performed to improve the design and performance of the drug delivery systems.

References

1. Jiang H, Hu Y, Zhao P, Li Y, Zhu K. Modulation of protein release from biodegradable core-shell structured fibers prepared by coaxial electrospinning. J Biomed Mater Res - Part B Appl Biomater. 2006 Oct;79(1):50–7.

2. Zhang YZ, Wang X, Feng Y, Li J, Lim CT, Ramakrishna S. Coaxial electrospinning of (fluorescein isothiocyanate-conjugated bovine serum albumin)-encapsulated poly(ε-caprolactone) nanofibers for sustained release. Biomacromolecules. 2006;7(4):1049–57.

3. Liao IC, Chew SY, Leong KW. Aligned core-shell nanofibers delivering bioactive proteins. Nanomedicine. 2006;1(4):465–71.

4. Huang ZM, He CL, Yang A, Zhang Y, Han XJ, Yin J, et al. Encapsulating drugs in biodegradable ultrafine fibers through co-axial electrospinning. J Biomed Mater Res - Part A. 2006 Apr 1;77(1):169–79.

5. Andriolo JM, Sutton NJ, Murphy JP, Huston LG, Kooistra-Manning EA, West RF, et al. Electrospun Fibers for Controlled Release of Nanoparticle-Assisted Phage Therapy Treatment of Topical Wounds. In: MRS Advances. Materials Research Society; 2018. p. 3011–7.

6. Klein S, Kuhn J, Avrahami R, Tarre S, Beliavski M, Green M, et al. Encapsulation of bacterial cells in electrospun microtubes. Biomacromolecules. 2009 Jul 13;10(7):1751–6.